UNIVERSITA' DEGLI STUDI "G. d'Annunzio"

Chieti-Pescara

SCUOLA SUPERIORE "G. d'Annunzio"

DOTTORATO DI RICERCA IN

NEUROSCIENZE E IMAGING

CICLO

XXXVIII

An MRI investigation of grey matter microstructure with multi-compartment diffusion-modelling and its relation to T1 and BOLD contrast in the healthy brain

Dipartimento di Neuroscienze, Imaging e Scienze Cliniche

Settore Scientifico Disciplinare PHYS-06/A

Dottorando

Ekaterina Bliakharskaia

Coordinatore

Prof. Carlo Sestieri

Tutor

Prof. Richard Wise

Co-Tutor

Prof. Cosimo Del Gratta

Anni Accademici 2022/2023-2024/2025



An MRI investigation of grey matter microstructure with multi-compartment diffusion-modelling and its relation to T1 and BOLD contrast in the healthy brain

Ekaterina Bliakharskaia

Department of Neuroscience and Imaging G. d'Annunzio University of Chieti–Pescara

A thesis submitted for the degree of Doctor of Philosophy

Gennaio 2026

An MRI investigation of grey matter microstructure with multi-compartment diffusion-modelling and its relation to T1 and BOLD contrast in the healthy brain

Author: Ekaterina Bliakharskaia

Department of Neurosciences, Imaging and Clinical Sciences, G. d'Annunzio University of Chieti-Pescara, Italy.

Tutor: Prof. Richard Wise

Department of Neurosciences, Imaging and Clinical Sciences, G. d'Annunzio University of Chieti-Pescara, Italy.

Co-Tutor: Prof. Cosimo Del Gratta

Department of Neurosciences, Imaging and Clinical Sciences, G. d'Annunzio University of Chieti-Pescara, Italy.

Gennaio 2026

Acknowledgments

This thesis was carried out at the Department of Neurosciences, Imaging and Clinical Sciences, Gabriele d'Annunzio University of Chieti-Pescara. I present here the research I carried out during the PhD Programme in Neuroscience and Imaging (XXXVIII cycle), entitled "An MRI investigation of grey matter microstructure with multi-compartment diffusion modelling and its relation to T1 and BOLD contrast in the healthy brain", under the supervision of Professor Richard Wise and Professor Cosimo Del Gratta.

I would like to express my deepest gratitude to my tutors, Prof. Richard Wise and Prof. Cosimo Del Gratta. It has been an incredible opportunity and a true pleasure to work under their guidance throughout these years. Their unwavering support, invaluable insights, and patience have been instrumental in shaping my journey. I am especially thankful for their thoughtful feedback and encouragement, which have greatly contributed to both my professional and personal growth. I will forever remain grateful for their mentorship and the knowledge they have imparted to me during my PhD program.

I am also grateful to Eleonora Patitucci for making available the neuroimaging dataset from the School of Psychology, CUBRIC, Cardiff University (United Kingdom), on which the first two studies of this thesis are based. Working with this data provided invaluable initial experience in the handling, processing, and interpretation of diffusion MRI and quantitative MRI measures.

My warmest gratitude goes to Alessandra Caporale, who was in many ways my de facto mentor throughout this PhD. I am deeply thankful for her trust, guidance, and unwavering support- despite having a young child and many other projects, she always found time to help me, and I learned immensely from her, especially in programming and day-to-day research practice.

I am deeply thankful to my colleagues and all members of our MRI lab for their kindness, support, and friendship. They created a welcoming environment and positive atmosphere that helped me adapt quickly to living and working in a new place. I feel fortunate to have been part of such a supportive team.

Finally, I would like to thank my family for being my foundation throughout this journey. To my husband, Andrea de Nicola, thank you for your constant encouragement, patience, and steady belief in me, especially during the most demanding periods of this PhD. To my daughter, Amina Bliakharskaia, thank you for your quiet faith in me, your understanding, and the warmth you brought to our home-your help and support made more difference than you may ever know.

Thesis Summary

This PhD thesis focuses on the non-invasive investigation of grey matter (GM) microstructure using magnetic resonance imaging (MRI) and examines how microstructural parameters derived from multi-compartment diffusion modelling relate to the longitudinal relaxation rate R1 (1/T1), a quantitative marker sensitive to myelin-related cortical tissue properties, although not uniquely specific to myelin, as well as to functional brain activity measured with Blood Oxygen Level Dependent functional magnetic resonance imaging (BOLD-fMRI) in healthy volunteers. The central motivation is that conventional MRI measures, including T1-weighted imaging, remain largely qualitative and non-specific, whereas modern quantitative MRI and biophysically motivated diffusion models enable a closer interpretation of MRI signal changes in terms of the underlying cellular architecture of the cortex.

Building on this motivation, the thesis brings together three complementary lines of investigation, with each chapter using the diffusion model most appropriate to the specific biological question addressed. First, it assesses the contribution of GM microstructure to the formation of R1 contrast using the Soma And Neurite Density Imaging (SANDI) model (Chapter 2), whose explicit separation of soma- and neurite-related signal compartments is particularly suited to probing cortical grey-matter cytoarchitecture, and tests whether these microstructural components are systematically associated with R1, a quantitative marker sensitive to myelin-related cortical tissue properties. Second, it evaluates the functional relevance of a GM microstructural marker of restricted diffusion derived from the Composite Hindered And Restricted Model of Diffusion (CHARMED) by examining its relationship with task-evoked BOLD responses during visuomotor learning (Chapter 3), thereby linking individual differences in restricted diffusion to functional recruitment. Third, it extends these structure-contrast analyses beyond cortex-averaged measures by performing depth-resolved profiling across the cortical ribbon (Chapter 4), again using SANDI to quantify depth-dependent relationships between R1 and soma- and neurite-related microstructural metrics, and revealing systematic patterns that are obscured when parameters are averaged across cortical thickness.

Overall, this thesis shows that combining quantitative R1 mapping with multi-compartment diffusion modelling enables a richer, compartment-informed interpretation of cortical MRI contrast. It further shows that moving from voxel- or region-averaged measures to depth-resolved analyses uncovers systematic, compartment-specific relationships between microstructure and R1 that are obscured when parameters are averaged across cortical thickness. Collectively, these findings support the feasibility of clinically accessible multi-parametric MRI for the in vivo characterization of GM microstructure and motivate its use in future studies of cortical organization and of microstructural alterations in health and disease.

List of Publications

Bliakharskaia E., Chiarelli A.M., Patitucci E., Carriero M., Di Censo D., Biondetti E., Del Gratta C., Capuani S., Palombo M., Tomassini V., Wise R.G., Caporale A. (2025) Exploring the contribution of gray matter microstructure to R1 contrast via multi-compartment diffusion modelling in the healthy brain, NeuroImage (2025), doi: https://doi.org/10.1016/j.neuroimage.2025.121466.

ABSTRACTS

Caporale A., **Bliakharskaia E**., Carriero M., Patitucci E., Di Censo D., Chiarelli A., Palombo M., Biondetti E., Wise R.G. (2025) Investigating gray matter microstructure via multi-compartment diffusion model and cortical myelination in healthy brains. Oral Presentation In *2025 ISMRM & ISMRT Annual Meeting & Exhibition.*

Bliakharskaia E., Patitucci E., Carriero M., Di Censo D., Chiarelli A.M., Biondetti E., Del Gratta C., Capuani S., Palombo M., Tomassini V., Wise R.G., Caporale A. (2025). Linking gray matter microstructure via multi-compartment diffusion modeling to cortical myelination in healthy brain. Poster Presentation In *XVI National Congress AIRMM.*

Bliakharskaia E., Caporale A., Patitucci E., Chiarelli A.M., Biondetti E., Germuska M., Tomassini V., Wise R.G., (2024). Investigating the relationship between restricted diffusion, cortical myelination and functional brain activity. Poster Presentation In *XV National Congress AIRMM.*

Contents

Acknowledgments I

Thesis Summary III

List of Publications V

List of Figures IX

List of Tables XII

1. General Introduction 1

1.1. The Brain and its Microstructure 1

1.1.1. Brain Anatomy 1

1.1.2. Brain Tissue 3

1.2. Imaging Brain Microstructure and Function 7

1.2.1. Basics of Magnetic Resonance Imaging 7

1.2.2. Main MRI Modalities 16

1.3. Introduction to Diffusion Weighted Imaging 20

1.3.1. Basics of Diffusion MRI 20

1.3.2. Diffusion Contrast 22

1.3.3. Free vs Restricted Diffusion in Neural Tissue 23

1.3.4. Diffusion Tensor Imaging 25

1.3.5. The Composite Hindered And Restricted Model of Diffusion (CHARMED) 27

1.3.6. The Soma And Neurite Density Imaging Model (SANDI) 29

1.4. Introduction to fMRI 31

1.4.1. Physiological And Physical Basis of fMRI Signal 31

1.4.2. The BOLD Mechanism 32

1.4.3. Functional Mapping with fMRI 35

1.4.4. The fMRI Experiment 37

2. Exploring the Contribution of Grey Matter Microstructure to R1 Contrast via Multi-Compartment Diffusion Modelling in the Healthy Brain 38

Abstract 38

2.1. Introduction 39

2.2. Methods 42

2.2.1. Data acquisition 42

2.2.2. Data processing 44

2.2.3. Statistical Analysis 46

2.3. Results 47

2.4. Discussion 55

2.5. Conclusions 62

3. Functional Brain Activation During Visuomotor Learning and the Role of Restricted Diffusion in Grey Matter 63

Abstract 63

3.1. Introduction 64

3.2. Methods 66

3.2.1. Data acquisition 66

3.2.2. Data processing 68

3.3. Results 73

3.4. Discussion 81

3.5. Conclusions 85

4. Depth-Dependent Associations Between Grey Matter Microstructure and R1 Revealed by R1 Mapping and SANDI Modelling 86

Abstract 86

4.1. Introduction 87

4.2. Methods 89

4.2.1. Data acquisition 89

4.2.2. Data processing 91

4.3. Results 93

4.3.1. Depth-dependent profiles of R1 and SANDI metrics 93

4.3.2. Inter-subject variability of depth profiles 98

4.3.3. Depth-dependent correlations between R1 and SANDI metrics 101

4.4. Discussion 108

4.5. Conclusions 111

5. General conclusions 113

References 118

Appendix A – Supplementary Materials 126

List of Figures

Figure 1.1. Sagittal view of the human brain 1
Figure 1.2. Lateral view of the cerebral cortex 2
Figure 1.3. Coronal view of brain anatomy 4
Figure 1.4. Schematic representation of a neuron 5
Figure 1.5. Hydrogen protons 8
Figure 1.6. Excitation 10
Figure 1.7. T1 Relaxation 11
Figure 1.8. T1 Relaxation Curves 12
Figure 1.9. T2 Relaxation 13
Figure 1.10. T2 Relaxation Curves 14
Figure 1.11. Diagram of the MP2RAGE sequence 18
Figure 1.12. Schematic representation of the Stejskal-Tanner sequence. 23
Figure 1.13. Schematic representation of water molecule trajectories under restricted and hindered diffusion in biological tissues 24
Figure 1.14. Schematic representation of water molecule trajectories within white-matter fibres represented by cylindrical geometry 25
Figure 1.15. Schematic illustration of the BOLD effect. 34
Figure 1.16. The BOLD effect. 34
Figure 1.17. BOLD signal time course. Typical temporal evolution of the BOLD signal in an fMRI experiment, with the stimulus indicated by the red bar. 35
Figure 1.18. Optimal echo time (TE) for the BOLD effect 37
Figure 2.1. Signal-to-noise ratio (SNR) of diffusion-weighted images 50
Figure 2.2. Group average parametric maps. 51
Figure 2.3. Scatter plots of SANDI metrics vs R1 in Grey and White Matter regions (GM and WM, respectively) 52
Figure 2.4. Subject-wise correlation coefficient between SANDI metrics and R1 53
Figure 2.5. Scatter plots of SANDI metrics vs R1 in Grey Matter across subjects 54
Figure 2.6. Distribution of correlation coefficients between SANDI metrics and R1 across subjects for various Grey Matter regions (ROIs).. 555
Figure 3.1. Visuomotor learning task paradigm 68
Figure 3.2. Grey matter (GM) partial volume estimate (PVE) masks derived from FAST segmentation 722
Figure 3.3. Harvard - Oxford atlas 722
Figure 3.4. Subject-specific ROIs. 733
Figure 3.5. Representative restricted fraction (FR) maps. 74
Figure 3.6. BOLD activation during the visuomotor task 75
Figure 3.7. BOLD activation map overlaid on selected ROIs. 75
Figure 3.8. FR vs BOLD in the supplementary motor cortex 788
Figure 3.9. FR vs R1 in the two hemispheres. 80
Figure 4.1. Depth - dependent profiles of intra - neurite signal fraction (fneurite, blue, left axis) and R1 (red, right axis) across cortical layers in the precentral gyrus defined by the Desikan - Killiany atlas. 955

Figure 4.2. Depth - dependent profiles of intra - soma signal fraction (fsoma, blue, left axis) and R1 (red, right axis) across cortical layers in the precentral gyrus defined by the Desikan - Killiany atlas 96
Figure 4.3. Depth - dependent profiles of estimated soma radius (Rsoma, blue, left axis) and R1 (red, right axis) across cortical layers in the precentral gyrus defined by the Desikan - Killiany atlas 97
Figure 4.4. Inter - subject variability of depth - dependent profiles of intra - neurite signal fraction (fneurite). Individual depth profiles are shown for all subjects in the precentral gyrus defined by the Desikan - Killiany atlas 99
Figure 4.5. Inter - subject variability of depth - dependent profiles of intra - soma signal fraction (fsoma) 1000
Figure 4.6. Inter - subject variability of depth - dependent profiles of estimated soma radius (Rsoma) 1011
Figure 4.7. Depth-dependent correlations between R1 and intra - neurite signal fraction (fneurite) in the precentral gyrus defined by the Desikan - Killiany atlas (left hemisphere) 1033
Figure 4.8. Depth-dependent correlations between R1 and intra - neurite signal fraction (fneurite) in the precentral gyrus defined by the Desikan - Killiany atlas (right hemisphere) 1044
Figure 4.9. Depth-dependent correlations between R1 and intra - soma signal fraction (fsoma) in the precentral gyrus defined by the Desikan - Killiany atlas (left hemisphere). 1055
Figure 4.10. Depth-dependent correlations between R1 and intra - soma signal fraction (fsoma) in the precentral gyrus defined by the Desikan - Killiany atlas (right hemisphere) 10606
Figure 4.11. Depth-dependent correlations between R1 and estimated soma radius (Rsoma) in the precentral gyrus defined by the Desikan - Killiany atlas (left hemisphere). 10707
Figure 4.12. Depth-dependent correlations between R1 and estimated soma radius (Rsoma) in the precentral gyrus defined by the Desikan - Killiany atlas (right hemisphere). 10808

Appendix A

Figure S1. Scatter plots of SANDI metrics vs R1 in cortical and subcortical Gray Matter regions (GM ROIs) 1278
Figure S2. Scatter plots of SANDI metrics vs R1 in cortical and subcortical Gray Matter regions (GM ROIs) using GM and WM partial volume estimate masking 12829
Figure S3. Scatter plots of SANDI metrics vs R1 in Grey Matter (including cortical and subcortical structures) across subjects 12930
Figure S4. Scatter plot of Gray Matter (GM) region volume, cortical thickness and curvature against R1 1301
Figure S5. Depth - dependent profiles of intra - neurite signal fraction (fneurite, blue, left axis) and R1 (red, right axis) across cortical layers in all ROIs defined by the Desikan - Killiany atlas (left hemisphere) 1312
Figure S6. Depth - dependent profiles of intra - neurite signal fraction (fneurite, blue, left axis) and R1 (red, right axis) across cortical layers in all ROIs defined by the Desikan - Killiany atlas (right hemisphere) 1323
Figure S7. Depth - dependent profiles of intra - soma signal fraction (fsoma, blue, left axis) and R1 (red, right axis) across cortical layers in all ROIs defined by the Desikan - Killiany atlas (left hemisphere) 1334

Figure S8. Depth - dependent profiles of intra - soma signal fraction (fsoma, blue, left axis) and R1 (red, right axis) across cortical layers in all ROIs defined by the Desikan - Killiany atlas (right hemisphere).. 1345
Figure S9. Depth - dependent profiles of estimated soma radius (Rsoma, blue, left axis) and R1 (red, right axis) across cortical layers in all ROIs defined by the Desikan - Killiany atlas (left hemisphere). 13536
Figure S10. Depth - dependent profiles of estimated soma radius (Rsoma, blue, left axis) and R1 (red, right axis) across cortical layers in all ROIs defined by the Desikan - Killiany atlas (right hemisphere).. 13637

List of Tables

Table 2.1. Sequence details. Overview of parameters for Diffusion - Weighted Imaging (DWI) and R1 protocols. 43
Table 2.2. Beta coefficients of the regression analysis performed in GM considering the model in eq.7 and in WM considering the model in eq.8 53
Table 3.1. Results. Correlation between microstructure (FR) and task response (BOLD) across GM ROIs. 77
Table 3.2. Results. Correlation between microstructure (FR) and R1 across GM ROIs. 79
Table 4.1. Sequence details. Overview of parameters for Diffusion - Weighted Imaging (DWI) and R1 protocols. 91

1. General Introduction

This chapter provides an overview of the anatomical organization of the brain and introduces the main magnetic resonance imaging techniques employed in the studies presented in this thesis.

1.1. The Brain and its Microstructure

1.1.1. Brain Anatomy

The human brain is a highly organized structure composed of interconnected regions that together support sensory processing, voluntary and involuntary movement, cognition, memory, and emotion. The brain comprises six principal structures: the cerebrum, diencephalon, cerebellum and the medulla oblongata, pons and midbrain, which together form the brain stem [1] (Figure 1.1). Each structure supports distinct but interconnected functional domains.

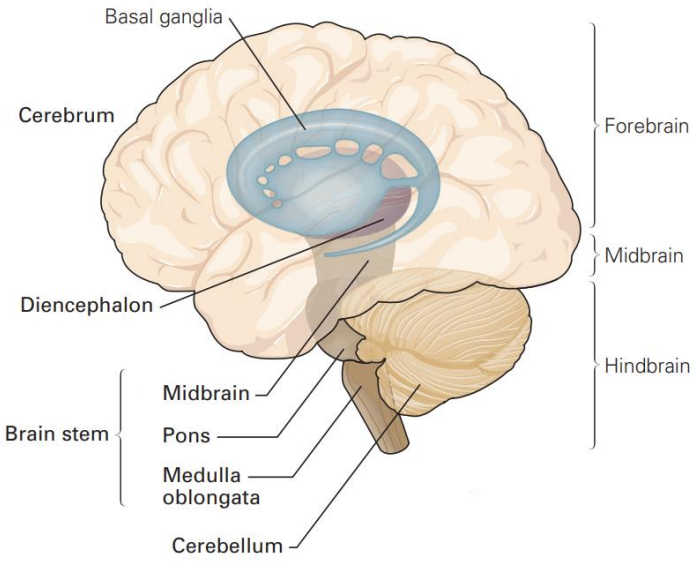


Figure 1.1. Sagittal view of the human brain. *The illustration highlights the major anatomical divisions, including the cerebrum, diencephalon, cerebellum, and brainstem (midbrain, pons, and medulla oblongata).*

The cerebrum comprises two cerebral hemispheres, right and left, each consisting of a heavily folded outer layer (the cerebral cortex) and three deep-lying structures (the basal ganglia, the hippocampus, and the amygdaloid nuclei). The hemispheres are separated by the longitudinal fissure. Although the hemispheres are generally symmetrical in shape, each contributes differently to higher-order functions. Anatomically, both hemispheres are subdivided into four major lobes - frontal, parietal, temporal, and occipital - each associated with specialized roles in perception, action, and cognition (Figure 1.2). The frontal and parietal lobes are separated by the central sulcus, whereas the temporal lobe is delineated superiorly by the lateral fissure. Posteriorly, the occipital lobe encompasses the primary visual areas. The two hemispheres communicate mainly via the corpus callosum, a large fibre bundle that coordinates interhemispheric information transfer. The basal ganglia participate in regulating motor performance; the hippocampus is involved with aspects of memory storage; and the amygdaloid nuclei coordinate the autonomic and endocrine responses of emotional states [2].

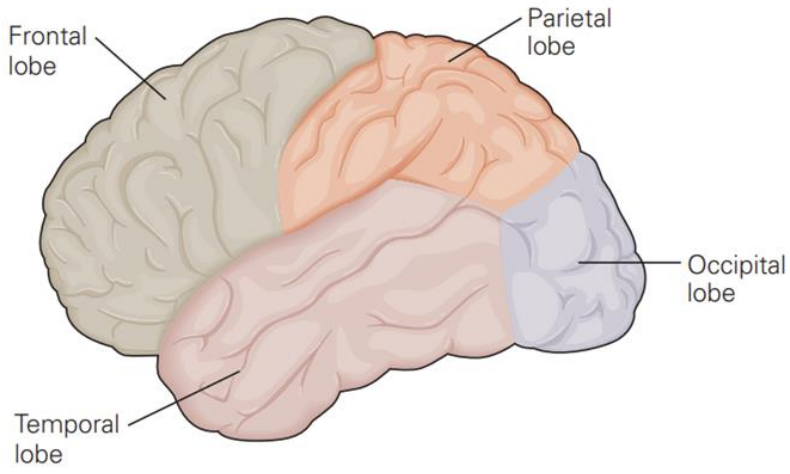


Figure 1.2. Lateral view of the cerebral cortex. *Shows the four lobes: frontal, parietal, temporal, and occipital.*

The **diencephalon** is positioned anterior to the midbrain and comprises two principal structures: the thalamus and the hypothalamus. The thalamus serves as the major relay hub, filtering and transmitting most sensory and motor signals destined for the cerebral cortex. In

contrast, the hypothalamus coordinates a wide range of autonomic, endocrine, and visceral processes, maintaining homeostasis and mediating the body's adaptive responses.

The **cerebellum** is located posterior to the pons and is linked to the brainstem through three large fibre bundles known as the cerebellar peduncles. Functionally, it fine-tunes the amplitude and timing of movements and plays a crucial role in motor learning by adjusting motor commands based on sensory feedback and experience.

The **medulla oblongata** is situated immediately above the spinal cord and includes several centers responsible for vital autonomic functions, such as digestion, breathing, and the control of heart rate.

The **pons**, located anterior to the medulla, conveys information about movement from the cerebral hemispheres to the cerebellum.

The **midbrain**, positioned above the pons, controls many sensory and motor functions, including eye movement and the coordination of visual and auditory reflexes.

The brain is also commonly divided into three broader regions: the hindbrain (medulla oblongata, pons, and cerebellum), midbrain, and forebrain (diencephalon and cerebrum) [1]. The hindbrain (excluding the cerebellum) and midbrain together include the same structures as the brain stem (Figure 1.1).

1.1.2. Brain Tissue

Cells in the brain can be classified according to their structure and function in two major types: neurons and glial cells. Neurons are the main functional units of the brain responsible for the transmission and processing of information, while glial cells provide the necessary support to ensure the stability and efficiency of neural communication [3]. Between the brain and the skull there are three layers of membranes, called meninges, which have the role of protecting the brain from external damage and are filled with cerebrospinal fluid (CSF). Investigating brain slices shows that neural tissue is not uniform but has some darker areas (grey matter) and some lighter areas (white matter) [3].

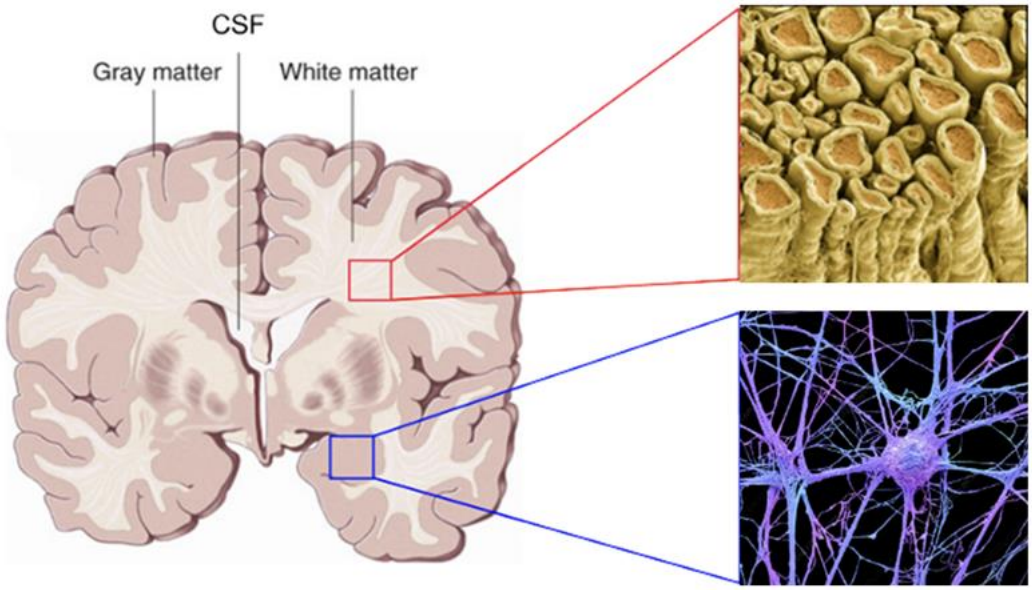


Figure 1.3. Coronal view of brain anatomy. *It illustrates the distribution of white matter, grey matter, and cerebrospinal fluid (CSF). The microstructural organization of both white and grey matter is depicted using scanning electron microscopy images (Science photo library. http://www.sciencephoto.com, [Accessed on 10.09.2025]).*

Grey matter is mainly formed by neuron cell bodies which are the information processing centers of the brain and are grouped according to structure and function in larger areas called nuclei. White matter mostly consists of axons, an extension of neurons that facilitate communication between different regions of the brain. Axons that connect the same regions tend to bundle together and form tracts. Figure 1.3 illustrates the main features of brain anatomy, while Figure 1.4 schematically illustrates the main anatomical features of a neuron [4].

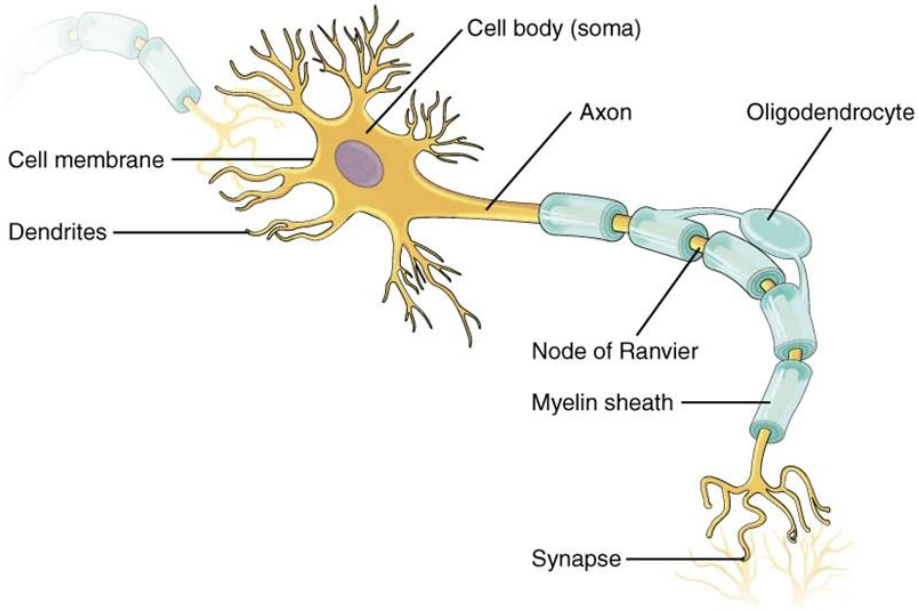


Figure 1.4. Schematic representation of a neuron. *The cell body features short, branched extensions (dendrites) which allow communication with nearby neurons and a long projection (axon) which facilitates communication over longer distances. Axons are usually covered in myelin sheaths which improve the conduction speed of electric impulses.*

Grey matter

Grey matter contains mostly neuronal cell bodies, unmyelinated axons, glial cells and blood capillaries and serves to process information in the brain. As illustrated in Figure 1.3, the majority of grey matter is located at the surface of the brain where it forms the cerebral cortex, a sheet-like structure with thickness varying between 2 and 5 mm [5]. Islands of grey matter can also be found inside the brain in regions such as the thalamus or basal ganglia. The cerebral cortex consists of many different types of neurons, which from the standpoint of cytology can be grouped in two main classes: pyramidal cells (neurons with long axons) and stellate cells (neurons with short axons). Staining cross-sections of tissue allows a direct visualization of cell bodies which were thoroughly studied in the early 20th century and revealed the laminar structure of the cortex. The different layers are interconnected and form vertical columns that extend from the surface of the brain (pial surface) to white matter [5]. Vertical columns with similar cytoarchitecture are grouped together, making cortical parcellation possible. One of the most famous parcellations consists of the Brodmann areas, defined and numbered by the anatomist Korbinian Brodmann in the early 20th century [6]. The Broadman areas represent regions of the cerebral cortex which have a similar histological structure and organization of cells. Later studies have shown an overlap between functional proper ties of different areas and

their cytoarchitecture [5]. The neuronal cell bodies vary in shape and size between different layers and cortical areas. For example, pyramidal cells can be classified according to their diameter as small (1-12 m), medium (20-25 m), large (45-50 m) and giant (70-100 m, characteristic for the motor cortex). The structure and thickness of the cortex are of interest for studying normal brain development as well as a wide range of neurodegenerative diseases and psychiatric disorders, such as Alzheimer's and other dementias, schizophrenia, etc. [7].

White matter

White matter is primarily composed of axons and supporting glial cells. As illustrated in Figures 1.3 and 1.4, axons are long and thin projections of neuron cell bodies that facilitate information transfer between cortical and subcortical regions. The tip of the axons consists of growth cones which sense chemical signals and determine the development in the desired direction [8]. They are organized in bundles which are commonly referred to as tracts. Glial cells are adjacent to axons and have an important role in determining the structure and function of white matter. For example, astrocytes maintain a balanced chemical environment of neurotransmitters and regulate the uptake of nutrients from the blood, while oligodendrocytes produce the myelin sheath surrounding the axons which acts as electric insulation and increases the speed of signal conduction [9]. The key role of axons is to transfer chemical and electrical impulses between neurons, allowing long-distance communication. The length of axons in the body varies between millimeters to meters and their inner diameters are orders of magnitude smaller, ranging between 0.1 to 20 microns [10]. Light microscopy measurements of axon inner diameter in the human corpus callosum show size distributions with a mode between 0.5 to 1 m and a range of values up to 9 m [35]. Nevertheless, there is significant shrinkage during the fixation process (65%) [11] which needs to be accounted for when comparing histological images with in-vivo measurements. The conduction speed of electrical impulses increases with axon diameter, however, due to the complexity of neural network and limited volume, the axons in the brain cannot have a large diameter. This problem was solved by the myelin sheaths, a lipid-rich substance that is wrapped around the axons and insulates them. Myelination allows a dramatic increase in conduction velocity compared to unmyelinated axons, which has facilitated the evolution of human cerebral function [9]. The thickness of the myelin sheath increases with axon diameter, yielding a g-ratio (ratio between inner and outer axon diameters) between 0.6 and 0.8 [12], [13]. The myelin sheath is interrupted every 1-2 millimeters by unmyelinated segments called nodes of Ranvier. When axons have this structure, the signal

propagates from node to node, which results in a higher conduction velocity. The white matter structure is closely related to its function, with the thickest axons originating in primary motor and somatosensory areas and the thinnest ones in prefrontal and temporal areas [14]. This suggests that fast conduction is required for movement and sensory processing which are important for survival, while higher cognitive tasks do not require the same conduction speed [14]. The structure and function of white matter can be affected by different pathologies that affect the myelin sheaths, axons or glial cells. For example, demyelination is characterised by a defective chemical structure of the myelin and is a characteristic of leukodystrophies, a group of diseases that affect children and young adults. On the other hand, demyelination describes the loss of previously healthy myelin and can happen though different mechanisms in diseases such as multiple sclerosis or schizophrenia [15]. Axon and neural degeneration can also occur because of traumatic injuries. All these conditions result in an impaired function of white matter; however, they all have different cellular mechanisms. To differentiate and track the progression of different lesions, first we need to localize and characterize them.

1.2. Imaging Brain Microstructure and Function

1.2.1. Basics of Magnetic Resonance Imaging

1.2.1.1. Magnetisation

Magnetic Resonance Imaging (MRI) originated from a groundbreaking discovery by Felix Bloch over 50 years ago. Bloch, in his Nobel Prize-winning research, identified unique properties of atomic nuclei, suggesting that they act like magnets. He found that a spinning charged particle, such as a proton, generates a magnetic field, referred to as magnetic momentum. Consequently, the nucleus behaves like a miniature bar magnet, capable of interacting with external magnetic fields. This interaction allows for the measurement and manipulation of their magnetic states, which is fundamental to MRI technology. In MRI, the primary focus is on hydrogen nuclei found in the water and fat molecules of the body.

The hydrogen atom, the first element in the periodic table, consists of a nucleus known as a proton and a single electron. This proton is charged and spins around its axis. When looking at multiple hydrogen protons within a molecule, they resemble numerous tiny bar magnets rotating on their own axes. In the human body, these small bar magnets, or protons, align in a

way that their magnetic forces neutralize each other, keeping the body in a state of magnetic equilibrium, as shown schematically in Figure 1.5 A.

When a patient is placed inside the MRI scanner, the hydrogen protons in their body align with the strong external magnetic field (B_0). These protons can align in two ways: parallel (low energy state) or anti-parallel (high energy state) to the magnetic field. The distribution of protons in these states is unequal, with a preference for the low energy state. Consequently, more protons align parallel to the magnetic field than anti-parallel (as shown schematically in Figure 1.5 B). This predominant parallel alignment generates a net magnetisation vector aligned with B_0, and it is this that we measure during MRI.

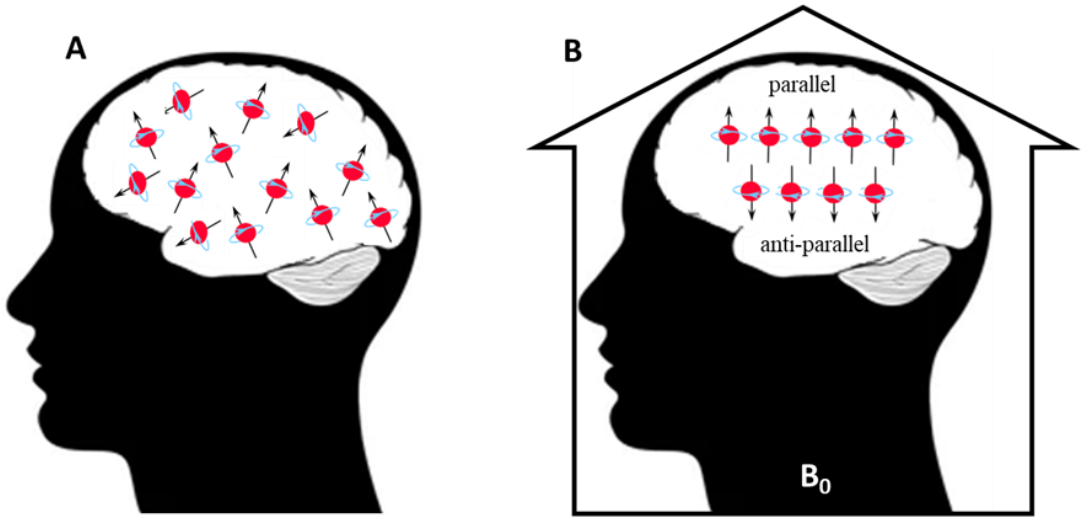


Figure 1.5. Hydrogen protons. *(A) Without the influence of a strong magnetic field, the protons in hydrogen atoms are ordered in random directions, in such a way that the magnetic forces equalize. (B) When the protons experience a strong magnetic field from the scanner, they align parallel with the field. B0 is the indication for the magnetic field of the MRI scanner, reported in units of tesla - T.*

These aligned protons do not remain static but instead precess around the direction of the static magnetic field at a specific frequency called the Larmor frequency. This frequency is determined by the strength of the magnetic field and the gyromagnetic ratio of the proton, described by the following equation (Equation 1.1):

$$\omega_0 = \gamma B_0 \tag{1.1}$$

where ω_0 is the Larmor frequency (MHz), γ is the gyromagnetic ratio (MHz/T) and B_0 is the static magnetic field strength (T). The gyromagnetic ratio for hydrogen nuclei is γ = 42.57 MHz/T.

The establishment of a net longitudinal magnetisation and its precessional motion in the static magnetic field constitute the initial physical conditions required for magnetic resonance. However, this equilibrium state alone does not produce a detectable MR signal. To generate measurable signals and encode spatial and tissue-specific information, the nuclear magnetisation must be deliberately perturbed and subsequently allowed to evolve under controlled experimental conditions.

MRI image formation relies on a sequence of excitation, relaxation, signal acquisition, and reconstruction processes, which are addressed in detail in the subsequent sections.

1.2.1.2. Excitation

Prior to data acquisition, the MRI system performs an automated frequency calibration procedure, known as a pre-scan, to determine the resonant (Larmor) frequency of hydrogen nuclei in the static magnetic field. This center frequency defines the operating frequency of the radiofrequency (RF) system and ensures efficient excitation of nuclear magnetisation.

Manipulation of the net magnetisation is achieved through the application of RF pulses tuned to this resonant frequency. Resonant excitation enables selective interaction with nuclear spins precessing at the Larmor frequency, which constitutes the physical basis of magnetic resonance. The characteristics of the RF pulse, including its amplitude and duration, define the extent of rotation of the magnetisation vector.

Application of an RF pulse at the center frequency with an appropriate flip angle rotates the longitudinal magnetisation into the transverse X-Y plane, where it becomes detectable by the receiver coils (illustrated in Figure 1.6). This excitation step is a prerequisite for signal formation and the subsequent stages of MR data acquisition.

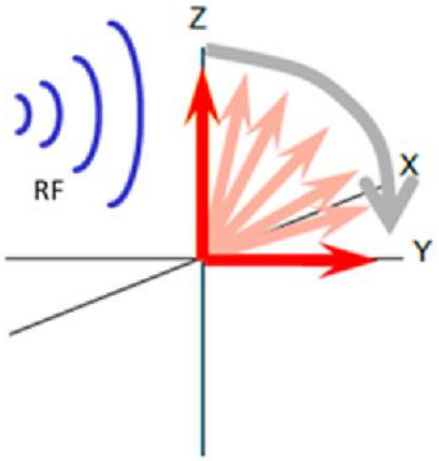


Figure 1.6. Excitation. *To perturb the alignment of the net magnetisation vector, an RF pulse is applied at the Larmor frequency. This RF pulse excites the protons, causing the net magnetisation to tilt away from the longitudinal axis (parallel to B0) into the transverse plane (perpendicular to B0).*

The Flip Angle (FA) defines the degree of rotation applied to the net magnetisation vector, induced by a RF pulse, and typically ranges from a few degrees up to 180º. The flip angle is determined by the strength and duration of the applied RF pulse, described by the following equation (Equation 1.2):

$$\alpha = \gamma B_1 t \tag{1.2}$$

where α denotes the flip angle, γ is the gyromagnetic ratio (MHz/T), B_1 is the amplitude of the magnetic field (T) and t is the duration of the RF pulse (ms).

The choice of flip angle plays a critical role in determining the amount of transverse magnetisation generated during excitation, and consequently influences signal amplitude, contrast, and signal-to-noise efficiency in MRI acquisitions.

1.2.1.3. Relaxation

The process of relaxation describes how the net magnetisation of protons returns to equilibrium following perturbation by an RF pulse. In MRI, relaxation is conventionally characterised by two distinct but concurrent mechanisms: longitudinal (T1) relaxation and transverse (T2) relaxation. Although T1 and T2 relaxation occur simultaneously, they are independent

processes. T1 relaxation governs the recovery of magnetisation along the direction of the static magnetic field (Z-axis), whereas T2 relaxation describes the decay of coherent magnetisation within the transverse (X-Y) plane.

T1 Relaxation: After being disturbed, protons seek to return to their initial state known as equilibrium. Following the cessation of the RF excitation pulse, the net magnetisation regenerates along the Z-axis while emitting radio-frequency photons (Figure 1.7). T1 relaxation, also known as longitudinal relaxation, governs the process along the Z-direction. Consequently, after a brief interval, the system returns precisely to its state prior to the RF pulse application.

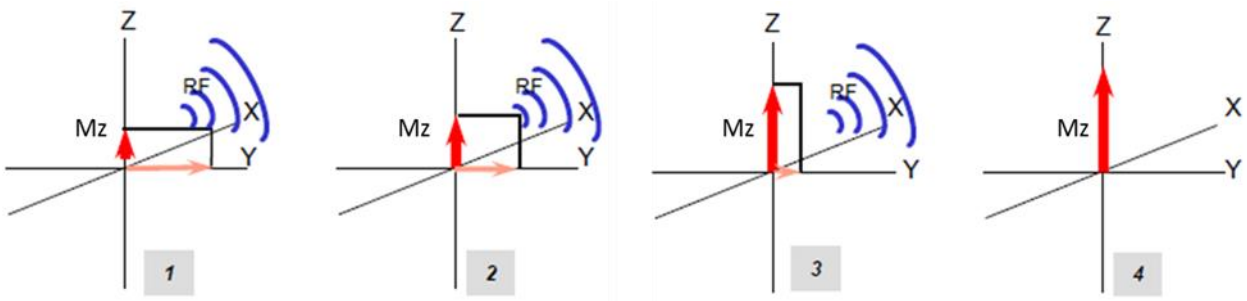


Figure 1.7. T1 Relaxation. *Describes the rate at which the net magnetisation vector (Mz) returns to its equilibrium state along the direction of the external magnetic field (B0) after the RF pulse is turned off.*

T1 relaxation is also known as Spin-Lattice relaxation, because the energy is released to the surrounding tissue (lattice).

T1 Relaxation Curves: Not all the protons are bound in their molecules in the same way. This is different for each tissue. One ^{1}H atom may be bound very tight, such as in fat tissue, while the other has a much looser bond, such as in water. Tightly bound protons will release their energy much quicker to their surroundings than protons, which are bound loosely. The rate at which they release their energy is therefore different. This relaxation rate is illustrated in Figure 1.8 A.

At time = 0, the curve indicates no magnetisation along the Z-direction immediately after the RF pulse. But immediately the Mz starts to recover along the Z-axis. T1 relaxation is a time constant. T1 is defined as the time it takes for the longitudinal magnetisation (Mz) to reach 63 % of the original magnetisation.

The recovery of longitudinal magnetisation (Mz) follows an exponential curve and can be described by Equation 1.3:

$$Mz(t) = M_0(1 - e^{-t/T_1}) \quad (1.3)$$

where $Mz(t)$ is the longitudinal magnetisation at time t, M_0 is the equilibrium magnetisation and T_1 is the longitudinal relaxation time.

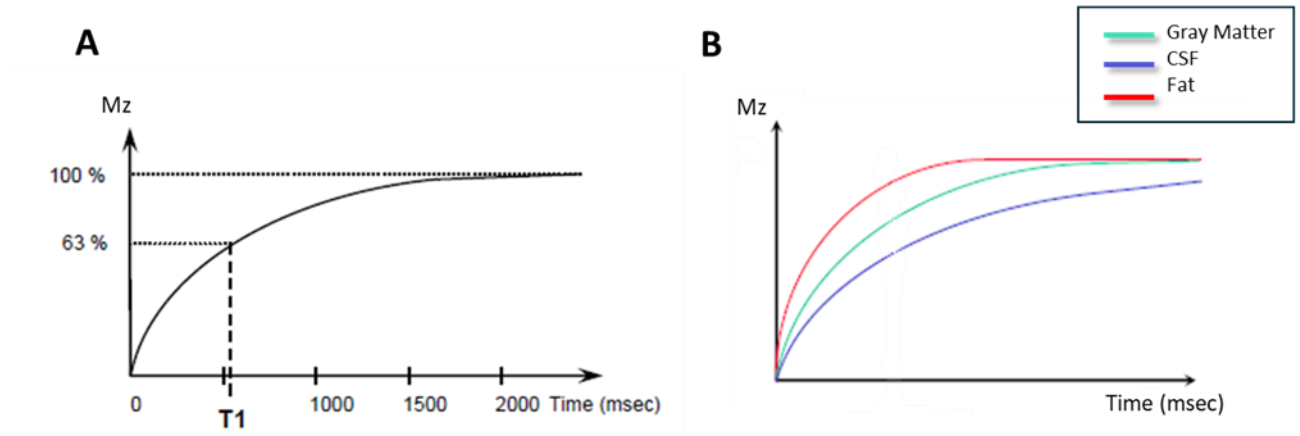


***Figure 1.8. T1 Relaxation** Curves. (A) The rate of T1 relaxation. (B) T1 relaxation curves for various tissue types.*

Each tissue will release energy (relax) at a different rate, and this gives origin to T1 contrast in MRI. T1 relaxation curves for various tissue types are shown in Figure 1.8 B. The red curve represents a tissue with a short T1 relaxation time (about 200-300 msec), showing rapid recovery of longitudinal magnetisation, the green curve represents a tissue with a moderate T1 relaxation time and the blue curve represents a tissue with a long T1 relaxation time, indicating slower recovery of longitudinal magnetisation (more than 2000 msec).

T2 Relaxation: The net magnetisation vector is the sum of all the small magnetic fields of the protons, which are aligned along the Z-axis. Each proton is spinning around its own axis. While they may spin at the same speed, they are not spinning *in-phase* or there is no phase coherence.

Upon application of the 90º RF pulse, besides flipping the magnetisation into the X-Y plane, the protons synchronize their spinning. Consequently, immediately after the 90º RF pulse, the net magnetisation vector (now termed transverse magnetisation) rotates within the X-Y plane around the Z-axis (Figure 1.9A). The vectors all point in the same direction because they are

in-phase. However, this alignment is transient. As each vector's magnetic field affects others, variations in their rotation speeds occur: some slow down while others accelerate. Consequently, the vectors rotate at different rates, leading to dephasing and the loss of alignment (Figure 1.9B, 1.9C, 1.9D). Initially, the degree of dephasing is minimal, but it progressively intensifies until complete loss of phase coherence, there is not one vector pointing in the same direction anymore. (Figure 1.9F).

Meanwhile, the whole lot is still rotating around the Z-axis in the X-Y plane.

This process of getting from a total *in-phase* situation to a total *out-of-phase* situation is called T2 relaxation or transverse relaxation.

T2 relaxation occurs significantly faster than T1 relaxation. T2 relaxation typically transpires within tens of milliseconds, whereas T1 relaxation may persist for seconds.

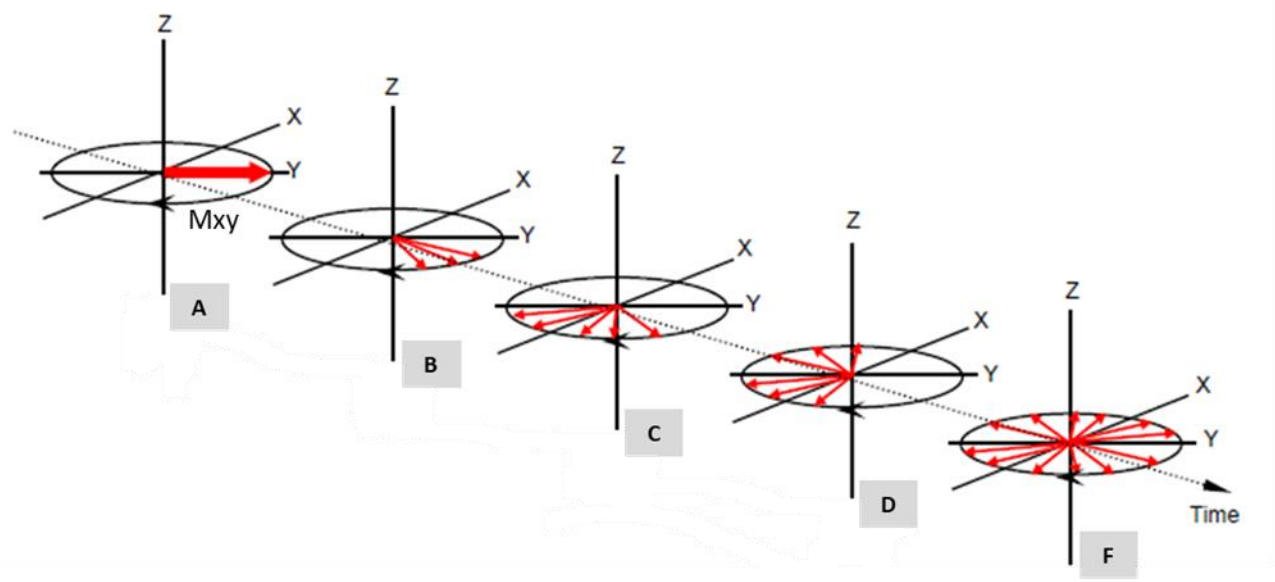


Figure 1.9. T2 Relaxation. *Describes the rate at which the transverse component of the net magnetisation vector (Mxy) decays due to interactions between spins after the RF pulse is turned off.*

T2 relaxation is also called spin-spin relaxation because it describes interactions between protons in their immediate surroundings (molecules).

T2 Relaxation Curves: Similar to T1 relaxation, T2 relaxation does not occur instantaneously. It reflects transverse dephasing driven by spin-spin interactions and microscopic field fluctuations associated with molecular motion and intermolecular interactions. Because tissue

microstructure and composition differ, T2 relaxation rates vary across tissues. The rate of T2 relaxation is illustrated in Figure 1.10 A.

Following the 90º RF-pulse, the net magnetisation is rotated into the transverse XY-plane, giving rise to a transverse magnetisation component M_{xy}. At time = 0 all spins are in-phase but immediately start to de-phase.

T2 relaxation is also a time constant. T2 is defined as the time it takes for the spins to de-phase to 37% of the original value.

The decay of transverse magnetisation follows an exponential behaviour and can be described by Equation 1.4:

$$Mxy(t) = M_{xy}(0)e^{-t/T_2} \tag{1.4}$$

where denotes the transverse magnetisation at time t, $M_{xy}(0)$ is the initial transverse magnetisation immediately after excitation, and T_2 is the transverse relaxation time.

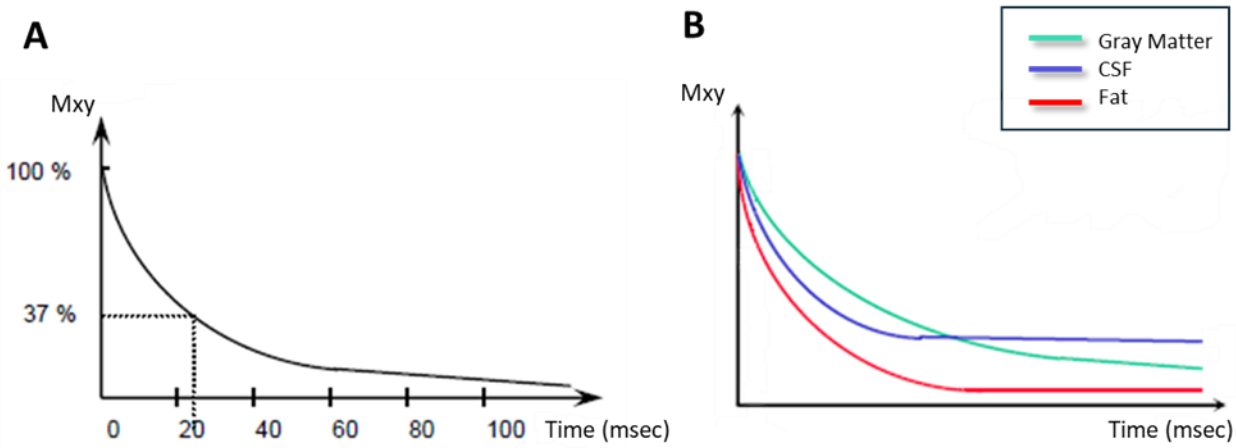


Figure 1.10. T2 Relaxation Curves. *(A) The rate of T2 relaxation. (B) T2 relaxation curves for various tissue types.*

The rate of de-phasing is different for each tissue. T2 relaxation curves for various tissue types are shown in Figure 1.10 B. The red curve represents a tissue with a short T2 relaxation time (about 50-100 msec), showing rapid decay of transverse magnetisation, which is typical for fat tissues; the green curve represents a tissue with a moderate T2 relaxation time (about 100-200 msec) and the blue curve represents a tissue with a long T2 relaxation time (more than 200

msec), indicating slower decay of transverse magnetisation, which is typical of tissues with high water content, such as cerebrospinal fluid or certain brain tissues.

1.2.1.4. Signal detection and spatial encoding

During relaxation, excited nuclear spins dissipate the energy absorbed during radiofrequency excitation through interactions with their surroundings, resulting in a progressive recovery of longitudinal magnetisation and a simultaneous decay of transverse magnetisation. The time-varying transverse magnetisation induces an electromotive force in the receiver coil, giving rise to a measurable MR signal. This signal, observed immediately following RF excitation, is referred to as the free induction decay (FID).

The ideal orientation for the receive coil is perpendicular to the main magnetic field (B_0). This alignment optimizes the coil's sensitivity to RF signals emitted by the relaxing spins, enhancing signal detection.

RF pulses and gradients can encode information about the spatial distribution of the transverse magnetisation into the frequency and phase of the signal. The gradient coil manipulates the static magnetic field, which induces a spatial variation in Larmor frequency, and imaging is feasible because the local precession frequency is proportional to the local magnetic field. The manipulation of the magnetic field is done by slice selection, frequency encoding and phase encoding.

The slice selection is determined by its position and geometry of the field of view. Gradient coil generates a linear gradient in B0 to select the slice. Therefore, each slice has a different Larmor frequency based on its location in the field and the selection is successful if the B1 magnetic field is oscillating with frequency equal to hydrogen spins in the slice of interest.

To encode the spatial distribution of the transverse magnetisation within the imaging plane, two orthogonal in-plane gradients are typically used. The choice of gradient axes is arbitrary and defined by the scanner coordinate system (conventionally denoted x and y). The first one is a spatial gradient along the x direction which encodes the frequency encoding in the x plane and the information on the position of the transverse magnetisation is acquired. A second one is for encoding the spatial information in the phase of the signal detected in the y plane, where different components of the transverse magnetisation will have diverse phase depending on their position along the y axis, but not of their precession frequency. In order to get the final

MR image, we need to transform the signal from the time domain, where numbers are stored in an array called k-space, to the frequency domain, through the Fourier transformation. There are several ways to sample k-space data, here we consider the Cartesian read-out, where data are acquired line-by-line. Moreover, in echo planar imaging readout (EPI) all the lines are acquired after one or a small number of excitations (single shot and multi-shot EPI respectively), therefore an entire 2D plane is collected following a single RF-excitation pulse. To do so, the gradients are rapidly switching to scan k-space.

1.2.2. Main MRI Modalities

Magnetic resonance imaging is an important modality in neuroimaging, due to its superior soft tissue contrast and non-invasive nature. MRI allows the acquisition of diverse image types by adjusting pulse sequences and contrast mechanisms, each highlighting different properties of brain tissue. In this work, we rely primarily on three complementary modalities: structural, diffusion, and functional MRI, which together provide a comprehensive view of brain microstructure and activity.

Structural Imaging

Conventional T1-weighted MRI is widely used to visualize the anatomical organization of the brain with high spatial resolution. Its contrast primarily reflects differences in longitudinal relaxation time (T1) across tissue types, which depend on water content, macromolecular composition, and myelin density [16], [17]. Grey matter typically appears darker than white matter due to its longer T1, while cerebrospinal fluid, with an even more prolonged T1, appears darkest, enhancing the separation between tissue classes. T1-weighted images therefore support reliable delineation of cortical boundaries, subcortical nuclei, and major white-matter pathways.

In parallel, T2-weighted imaging offers complementary information by emphasizing differences in transverse relaxation (T2). Tissues with high free-water content, such as CSF, exhibit long T2 values and appear hyperintense, whereas myelin-rich white matter, where water motion is more restricted, has shorter T2 and appears relatively darker. These contrast properties make T2-weighted scans especially useful for detecting oedema, inflammation, fluid-filled structures, or demyelinating processes, all of which alter local water mobility. The combination of T1- and T2-weighted contrasts thus provides a richer anatomical characterization than either modality alone.

Although conventional structural MRI remains central to morphometric analysis and clinical assessment, both T1- and T2-weighted contrasts are inherently qualitative and sensitive to acquisition parameters such as flip angle, TR, TE, and field strength. This dependence limits direct cross-subject or longitudinal comparisons and motivates the use of quantitative approaches discussed in the following sections.

Quantitative T1 and R1 Mapping

Conventional T1 - weighted images provide excellent anatomical contrast but remain inherently qualitative, because signal intensity depends on acquisition settings (e.g., TR, TE, flip angle) and scanner - and receive - coil - specific factors (e.g., B1 - inhomogeneity). Quantitative MRI addresses these limitations by estimating physical tissue parameters that are more comparable across subjects and sessions. In this thesis, the longitudinal relaxation rate R1 (s^{-1}), defined as the inverse of the T1 relaxation time (R1 = 1/T1), is used as a quantitative marker sensitive to myelin-related cortical tissue properties. R1 quantifies how rapidly longitudinal magnetisation recovers toward equilibrium along the main magnetic field B_0 after excitation and is sensitive to tissue microstructure, in particular macromolecular content and myelin-associated lipids. Consequently, R1 mapping has been widely adopted as a non-invasive quantitative marker related to cortical myelination [18]. Previous studies have reported a relationship between R1 and myelin content [19], [20] and a correspondence between histological myelin patterns and cortical contrast observed with high - resolution MRI [21], [22]. Importantly, R1 is not uniquely specific to myelin and can also be influenced by factors such as water content and iron concentration.

To obtain quantitative T1 (and thus R1) maps, we use the Magnetisation Prepared 2 Rapid Acquisition Gradient Echoes (MP2RAGE) sequence [23], an extension of MPRAGE originally developed for T1-weighted imaging [24]. MP2RAGE applies an adiabatic inversion pulse and acquires two 3D gradient-echo readouts at different inversion times (TI1 and TI2) within a single repetition ($MP2RAGE_{TR}$). The two readouts share identical geometry but have different T1-weighting (typically using different flip angles), enabling their combination to minimize receive bias-field effects ($B1^-$) and reduce the influence of proton density (M_0) and $T2^*$ on the final contrast; with appropriate parameter choice, sensitivity to transmit field inhomogeneity ($B1^+$) is also reduced. The MP2RAGE timing diagram is shown in Figure 1.11.

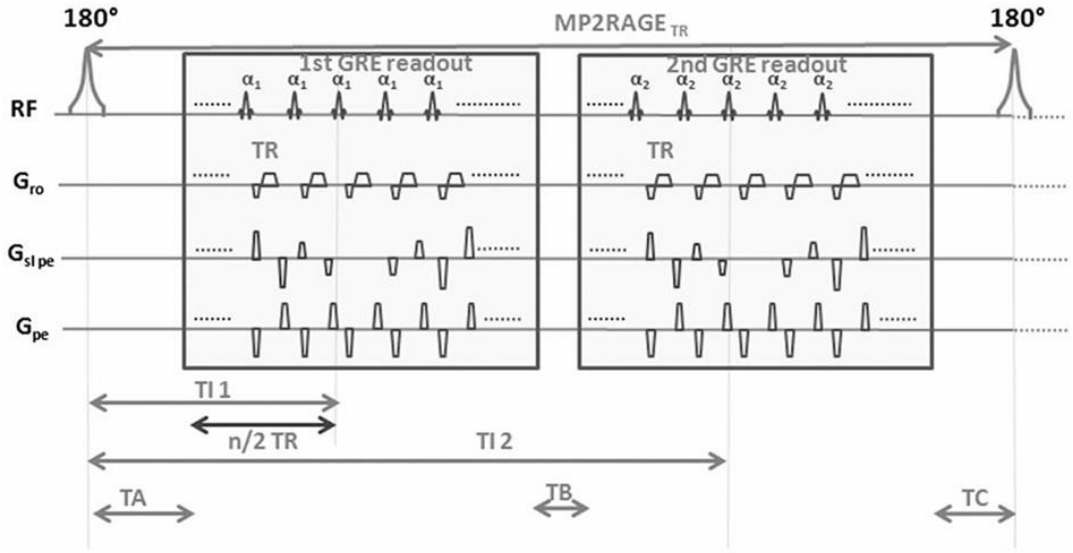


Figure 1.11. Diagram of the MP2RAGE sequence. *Inversion times TI1 and TI2 are defined as the time from the middle of the inversion pulse to the excitation corresponding to the center k-space line (phase encoding in the slab-selection direction). MP2RAGETR is the time between two successive inversion pulses, while TR is the time between successive excitation pulses in the GRE kernel, which is composed of n excitations. Adapted from (Marques et al., 2010)*

Following [23], the two images acquired at TI1 and TI2 can be combined to form a self-bias - field - corrected T1-weighted image:

$$MP2RAGE = \frac{GRE_{TI1}\, GRE_{TI2}}{GRE_{TI1}^2 + GRE_{TI2}^2} \tag{1.5}$$

Voxel-wise T1 is then estimated from the MP2RAGE signal using a sequence-specific signal model (typically implemented via Bloch simulations and a lookup table), and R1 is computed as R1 = 1/T1. Because MP2RAGE acquires both contrasts interleaved within one sequence, the two images are inherently co-registered, avoiding inter-scan motion and registration errors. Since then, the MP2RAGE technique has been widely used to detect variation in myelination across the cortex in vivo [25], [26].

Diffusion-Weighted Imaging

Diffusion-weighted imaging (DWI) measures the random (Brownian) motion of water molecules in tissue, providing information about microstructure and supporting tractography-based inference of structural connectivity within the brain. In environments with pronounced structural organization, where cellular membranes, myelinated axons, or densely packed dendrites constrain water mobility, water diffusion becomes directionally dependent, enabling the inference of tissue features far below the spatial resolution of MRI [27].

The simplest diffusion model, diffusion tensor imaging (DTI), yields metrics such as fractional anisotropy (FA) and mean diffusivity (MD), which are sensitive to tissue organization and microstructural integrity. However, DTI cannot resolve complex fibre geometries or compartment-specific microstructure.

Advanced diffusion models, such as NODDI for neurite density and orientation dispersion [28], CHARMED for restricted and hindered diffusion in axonal bundles [29], and SANDI for soma - neurite compartment estimation [30], provide richer microstructural specificity. These multi-compartment techniques are particularly relevant for studying cortical microarchitecture, where cellular density, dendritic complexity, and soma size influence the measured diffusion signal.

Functional MRI

Functional MRI (fMRI) measures changes in brain activity by detecting variations in blood oxygenation over time. The method relies on the blood-oxygenation-level-dependent (BOLD) contrast, which reflects the difference in magnetic susceptibility between oxygenated and deoxygenated hemoglobin. [31], [32] When a cortical or subcortical region increases its activity, local metabolic demand rises, triggering a vascular response that transiently elevates the concentration of oxygenated blood. This shift leads to a detectable increase in T2* - weighted signal intensity, allowing indirect inference of neural activity with millimeter-scale spatial resolution.[33]

Most fMRI studies rely on fast echo-planar imaging to acquire whole-brain volumes every 1–2 seconds, enabling measurement of time-varying signal fluctuations. Experimental designs typically involve either task-based paradigms, where activity is contrasted across conditions, or resting-state acquisitions, which assess spontaneous low-frequency correlations within distributed functional networks [34], [35]. Although the BOLD signal does not capture neuronal firing directly, the relationship between neuronal activity, energy consumption, and haemodynamic responses provides a robust proxy for functional engagement.

The spatial resolution of fMRI is influenced by several factors, including vascular geometry and partial-volume effects, while temporal resolution is limited by both acquisition speed and the intrinsic delay of the haemodynamic response, which evolves over several seconds. Despite these limitations, fMRI remains a central tool of human neuroimaging, providing investigations into perception, cognition, learning, and disease-related alterations in network function.

In the context of this thesis, functional MRI is relevant because it complements microstructural imaging by revealing how local tissue properties relate to task-evoked activity. Integrating fMRI with advanced diffusion modelling allows exploration of how local microstructural properties such as cellular density, neurite complexity, and restricted diffusion relate to the magnitude and spatial specificity of functional responses. The combination of fMRI with advanced diffusion models therefore supports a more comprehensive characterization of structure–function relationships in the human brain.

1.3. Introduction to Diffusion Weighted Imaging

Diffusion - weighted imaging (DWI) is an MRI technique that is sensitive to the microscopic random motion of water molecules within biological tissues. Unlike conventional MRI contrasts, which primarily reflect relaxation properties, DWI probes tissue architecture at a scale far below the spatial resolution of the image voxels. Because water motion is strongly influenced by cellular membranes, myelin sheaths, and other microstructural features, diffusion MRI provides indirect access to tissue microstructure *in vivo*.

In neural tissue, the displacement of water molecules over typical diffusion times occurs on the order of micrometers. Although these displacements are much smaller than the voxel dimensions, their cumulative effect leads to measurable changes in the MR signal when diffusion-sensitizing gradients are applied. As a result, diffusion MRI has become a key tool for investigating white and grey matter organization, connectivity, and microstructural alterations.

1.3.1. Basics of Diffusion MRI

Diffusion describes the random motion of particles driven by thermal energy, from a region of high concentration to a region of low concentration and is mathematically described by Fick's first law:

$$J(r,t) = -D\nabla c(r,t) \tag{1.6}$$

where $J(r,t)$ is the particle flux, D is the diffusion coefficient, $c(r,t)$ represents the particle concentration. The negative sign indicates that the direction of flow is from larger to smaller concentration. To describe the temporal evolution of the concentration field, Fick's first law (Equation 1.6) can be combined with the principle of mass conservation, expressed:

$$\frac{\partial c(r,t)}{\partial t} = -\nabla J(r,t) \tag{1.7}$$

Substituting the expression for the particle flux into the continuity equation yields Fick's second law, also known as the diffusion equation:

$$\frac{\partial c(r,t)}{\partial t} = D\nabla^2 c(r,t) \tag{1.8}$$

Even in the absence of a macroscopic concentration gradient, random molecular motion still exists due to thermal fluctuations. This phenomenon, known as Brownian motion, was first observed experimentally by Robert Brown [36] and mathematically described in 1905 by Albert Einstein (Einstein, 1905). In this case molecules undergo a process of "self-diffusion" and we are concerned with the probability $P(r_1, t_1|r_0, t_0)$ of a particle staring from r_0 and moving to r_1 in time $t_1 - t_0$. Under these conditions, the diffusion equation 1.8 can be rewritten for the probability density function as:

$$\frac{\partial P(r_1, t_1|r_0, t_0)}{\partial t_1} = D\nabla^2 P(r_1, t_1|r_0, t_0) \tag{1.9}$$

The function $P(r_1, t_1|r_0, t_0)$ is commonly referred to as the Green's function of the diffusion propagator and provides a complete statistical description of particle displacement during the diffusion process.

For diffusion in a homogeneous and isotropic medium with initial condition $P(r_1, 0|r_0, 0) = \delta(r_1 - r_0)$ and boundary condition $R \rightarrow 0$ for $r \rightarrow \infty$ the solution of equation 1.9 is:

$$P(r_1, t_1|r_0, t_0) = \left(4\pi D(t_1 - t_0)\right)^{-3/2} \exp\left(-\frac{(r_1 - r_0)^2}{4D(t_1 - t_0)}\right) \tag{1.10}$$

For free diffusion, the mean square displacement can be calculated from equation 1.9 as:

$$\langle (r_1 - r_0)^2 \rangle = \int_{-\infty}^{\infty} (r_1 - r_0)^2 P(r_1, t_1|r_0, t_0) dr_1 dr_0 = nD(t_1 - t_0) \tag{1.11}$$

with n = 2, 4, or 6 for one, two or three dimensions.

For example, for diffusion along line n = 2, for diffusion in a plane n = 4 and for diffusion in a volume n = 3.

1.3.2. Diffusion Contrast

Diffusion MRI exploits the sensitivity of the MR signal phase to molecular motion in the presence of magnetic field gradients. When the external magnetic field B_0 is homogeneous, the Larmor frequency is spatially invariant and the phase accumulated by a spin depends only on time:

$$\varphi(t) = w_0 t = \gamma B_0 t \tag{1.12}$$

Under these conditions, the accumulated phase is independent of the spatial position of the spin.

When an additional magnetic field gradient $G(t)$ is applied, the local magnetic field becomes position dependent, resulting in a spatially varying Larmor frequency. Consequently, the phase accumulated by a spin following a trajectory $r(t)$becomes:

$$\varphi(t) = \int_0^t (w_0 + \gamma G(t')r(t'))dt' = w_0 t + \gamma \int_0^t G(t')r(t')dt' \tag{1.13}$$

This principle forms the basis of spatial encoding in MRI and provides the mechanism by which molecular displacements due to diffusion can be encoded into the MR signal.

The standard sequence used to measure diffusion was introduced by Stejskal and Tanner in 1965. This sequence extends the conventional spin-echo experiment by incorporating two identical gradient pulses of duration δ placed before and after the refocusing RF pulse, separated by the time interval Δ. During the first gradient pulse, spins accumulate a phase proportional to their position. If spins remain stationary, the second gradient pulse fully refocuses on this phase. However, when spins undergo displacement between the two gradient applications, phase refocusing is incomplete, leading to a net phase dispersion across the spin ensemble and a corresponding attenuation of the MR signal. The Stejskal-Tanner sequence, which is also known in the literature as "pulsed gradient spin-echo" or "single diffusion encoding" is illustrated in Figure 1.12.

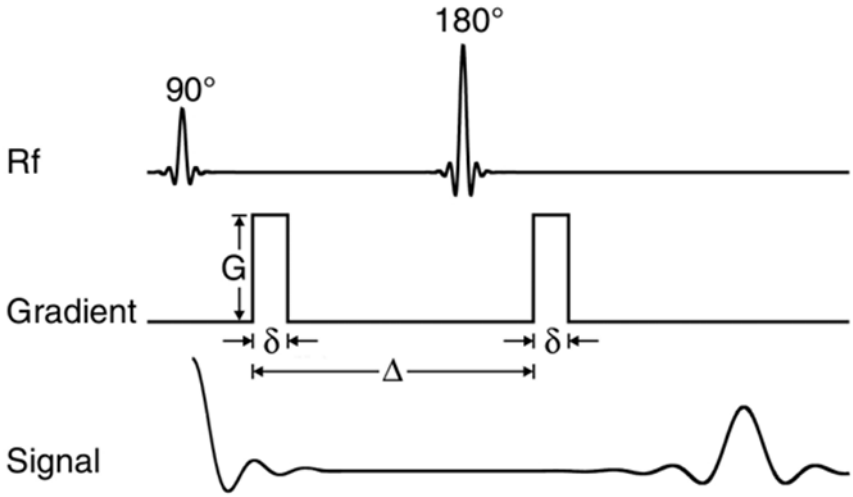


Figure 1.12. Schematic representation of the Stejskal-Tanner sequence. *Two identical diffusion-sensitizing gradient pulses of duration δ and amplitude G are applied on either side of the refocusing RF pulse and separated by the diffusion time Δ. Molecular displacement occurring between the gradient pulses leads to incomplete phase refocusing and results in diffusion-dependent signal attenuation.*

1.3.3. Free vs Restricted Diffusion in Neural Tissue

In classical diffusion theory, as formulated by Einstein, particles are assumed to move freely without encountering structural boundaries. In neural tissues, however, the motion of water molecules is strongly influenced by the surrounding microstructure. Inside cells, water is confined by the plasma membrane, and its movement is further curtailed by intracellular components such as macromolecules and organelles. Under these conditions, diffusion is considered *restricted*, as molecular displacements cannot exceed the physical dimensions of the compartment in which they are contained [37]. With respect to water in the extracellular space, the motion of molecules is also influenced by the cell membranes and macromolecules. Since diffusion is only possible around tissue structures, extra-cellular particles require longer trajectories and longer diffusion times to present similar displacements compared to free diffusion particles. In this case, diffusion is categorized as hindered because particle displacements are affected by obstacles but not limited to specific lengths [38]. Figure 1.13 schematically represents restricted and hindered diffusion processes in biological tissues.

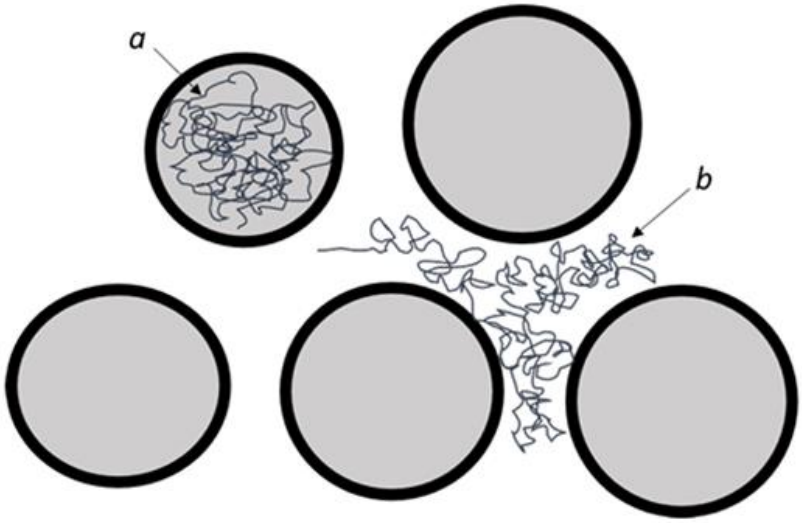


Figure 1.13. Schematic representation of water molecule trajectories under restricted and hindered diffusion in biological tissues. *In panel (a), intracellular water follows paths that remain fully confined (restricted) within the impermeable boundaries of the cell membrane. In contrast, panel (b) shows extracellular water, where molecular motion is influenced by surrounding cells and macromolecules, resulting in shortened but not strictly limited trajectories, known as hindered.*

Many biological tissues, including brain white matter, exhibit highly organized microstructural arrangements. As a result, the effects of tissue barriers can differ across spatial directions. Unlike free water diffusion, which is isotropic, diffusion in such tissues becomes anisotropic. In white matter, for example, myelinated axons form bundles of parallel fibres that constrain motion more strongly across than along the fibre axis [39]. The effects of hindered and restricted diffusion are more evident along the directions perpendicular to fibres, where water molecules translate with a larger influence of the obstacles imposed by the myelinated membranes of axons, and possibly neurofilaments and proteins aligned parallel to them [40]. Figure 1.13. illustrates a conceptual representation of the hindered and restricted effects of white matter fibres using a cylindrical fibre geometry.

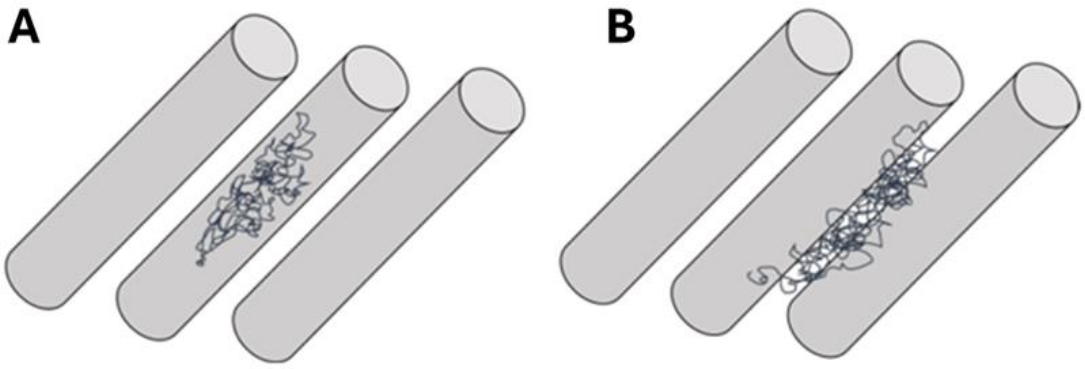


Figure 1.14. Schematic representation of water molecule trajectories within white-matter fibres represented by cylindrical geometry. *The restricted or hindered diffusion effects of the water inside and outside fibres, represented in A and B respectively, are more evident in directions perpendicular to the fibres' main direction.*

The diffusion coefficient in white matter varies with spatial direction because the angle θ defines the orientation between the measurement direction and the principal axis of the fibres. Diffusion reaches its highest values when water moves parallel to the fibres (θ = 0°) and its lowest values when displacement occurs perpendicular to them (θ = 90°), in line with the anisotropic behaviour reported in earlier diffusion studies [39], [41]. Since water motion in restricted and hindered regimes depends on the diffusion time, the apparent diffusion coefficient also changes with t. In particular, diffusion values decrease as diffusion time increases, an effect that is especially pronounced inside axons and in directions transverse to the fibre orientation, where the movement of water molecules is strongly constrained by axonal membranes and myelin [42]

In addition to their dependence on time and orientation, the displacement of water molecules in biological tissues might also not follow a Gaussian distribution as predicted by Einstein. Since tissue barriers produce multiple microstructural sub-compartments with a range of different sizes, the displacement distribution of all water molecules for all tissue compartments normally shows a non-Gaussian bell-shaped profile [38].

1.3.4. Diffusion Tensor Imaging

Diffusion tensor imaging (DTI), early dMRI technique, was proposed to model the anisotropy of brain water diffusion and obtain diffusion measures that do not depend on the direction of

the applied diffusion gradient. Instead of the constant scalar apparent diffusion coefficient, DTI represents diffusion of each image voxel using a second order tensor known as the diffusion tensor (D). Thus, the scalar diffusivity D in equations 1.16 to 1.9 is replaced by a 3x3 symmetric tensor $\widetilde{D}$ with elements $D_{\alpha\beta}$, where α and β take each of the Cartesian coordinates:

$$\widetilde{D} = \begin{pmatrix} D_{xx} & D_{xy} & D_{xz} \\ D_{yx} & D_{yy} & D_{yz} \\ D_{zx} & D_{zy} & D_{zz} \end{pmatrix} \tag{1.14}$$

In this case the diffusion signal depends on the gradient direction:

$$S = S_0 \exp\left(-b\hat{g}^T \widetilde{D} \hat{g}\right) \tag{1.15}$$

where S_0 is the signal without diffusion encoding gradient, b is the diffusion weighting factor and $\hat{g}$ denotes the gradient direction. Equation 1.15 has 6 independent parameters, thus at least 7 measurements are necessary to estimate the diffusion tensor $\widetilde{D}$: one measurement with $b = 0$ and 6 measurements with non-zero diffusion weighting and non-collinear gradient orientations ($g_i \times g_j \neq 0,\ for\ i \neq j$). In practice, for robust parameter estimates and to reduce the influence of noise and the orientational variance, at least 20-30 isotropically distributed gradient directions are used. Most diffusion tensor imaging (DTI) studies use b-values in the range 600-1200 s/mm^2, which yields on average an approximate signal attenuation of 0.5.

After the diffusion tensor is estimated from the data, we can perform an eigen decomposition of $\widetilde{D}$ in order to calculate the eigenvectors $\hat{d}_1$, $\hat{d}_2$ and $\hat{d}_3$ and the corresponding eigenvalues $\lambda_1 \geq \lambda_2 \geq \lambda_3$. This representation provides the principal directions of diffusion and the corresponding diffusivities. In practice, different functions of the eigenvalues are used to characterize the size and shape of the diffusion tensor. The simplest metric is mean diffusivity:

$$MD = \frac{1}{3} Trace(D) = \frac{D_{xx}+D_{yy}+D_{zz}}{3} = \frac{\lambda_1+\lambda_2+\lambda_3}{3} \tag{1.16}$$

Another commonly used metric which is rotationally invariant is fractional anisotropy, which describes the departure of D from isotropic diffusion:

$$FA = \sqrt{\frac{3}{2}} \frac{\sqrt{(\lambda_1-\overline{\lambda})^2+(\lambda_2-\overline{\lambda})^2+(\lambda_3-\overline{\lambda})^2}}{\sqrt{\lambda_1^2+\lambda_2^2+\lambda_3^2}} \tag{1.17}$$

DTI is widely used for brain imaging, however there are a number of clear limitations of this technique. First, the DTI model provides only a voxel-averaged diffusion tensor, which cannot

accurately describe more complex tissue configurations such as crossing fibres in the brain. Second, as the *b*-value is increased, there is a departure from mono-exponential decay due to diffusion in the intracellular space, and the Gaussian displacement model is no longer appropriate.

These limitations highlight the need for diffusion models that go beyond a single Gaussian description and are capable of representing multiple tissue compartments and complex microstructural organization. In the following sections, we therefore consider biophysically motivated approaches that model restricted and hindered diffusion in neural tissue.

1.3.5. The Composite Hindered And Restricted Model of Diffusion (CHARMED)

The theoretical framework proposed by Assaf et al. [40] was developed to overcome the limitations of the conventional Diffusion Tensor Imaging (DTI) model, most notably the assumption that water diffusion in biological tissues can be adequately described as a Gaussian process. While this assumption may hold under certain conditions and at low diffusion weightings, it becomes increasingly inaccurate in WM, where cellular membranes impose restrictions and hindrance on water displacement.

Within the CHARMED framework, diffusion in WM is described as arising from two distinct, non-exchanging compartments: a hindered extra-axonal compartment and a restricted intra-axonal compartment. Diffusion in the extra-axonal space is assumed to be hindered but effectively Gaussian, and therefore fully characterised by a diffusion tensor. In contrast, diffusion within the intra-axonal space is restricted by the axonal membrane. The two compartments are assumed not to exchange water, based on the assumption that the characteristic exchange time across the axonal membrane is much longer than the diffusion time probed by the MRI sequence. Under this assumption, the measured diffusion-weighted signal attenuation can be expressed as the weighted sum of the signals arising from the two compartments (with subscripts h and r denoting hindered and restricted components, respectively):

$$S(q,\Delta) = f_h \cdot S_h(q,\Delta) + f_r \cdot S_r(q,\Delta) \tag{1.18}$$

where f_h and f_r represent the signal fractions of the hindered and restricted compartments, respectively.

The vector q represents the reciprocal wavevector defined as $q = \gamma\delta G/2\pi$, where γ is the gyromagnetic ratio, δ is the diffusion gradient duration, and G is the diffusion gradient amplitude. This vector is defined in the laboratory reference frame and can be written as a sum of vectors parallel and perpendicular to the principal axonal axis, such that $q = q_{\perp} + q_{/\!/}$.

The signal contribution from the hindered diffusion component, corresponding to the extra-axonal compartment (which includes not only the extracellular space but also contributions from glial cells and astrocytes) can be modeled by the mono-exponential attenuation of the signal. Given the anisotropic nature of the diffusion process, this compartment is described using a diffusion tensor, yielding:

$$S_h(q,\Delta) = e^{-4\pi^2(\Delta-\frac{\delta}{3})\boldsymbol{q}^t D\boldsymbol{q}} \tag{1.19}$$

where D denotes the diffusion tensor of the hindered compartment.

The contribution from the restricted intra-axonal compartment can be further decomposed into components describing diffusion parallel and perpendicular to the axonal axis. These two displacement components are assumed to be statistically independent, allowing the restricted signal to be written as:

$$S_r(q,\Delta) = S_{\perp}(q_{\perp},\Delta)\cdot S_{/\!/}\left(q_{/\!/},\Delta\right) \tag{1.20}$$

It is reasonable to assume, in the first approximation, that diffusion along the axonal direction is assumed to be Gaussian. This contribution is therefore represented by:

$$S_{/\!/}\left(q_{/\!/},\Delta\right) = e^{-4\pi^2 {q_{/\!/}}^2(\Delta-\frac{\delta}{3})D_{/\!/}} \tag{1.21}$$

where $D_{/\!/}$ denotes the intra-axonal diffusivity along the axonal axis.

For the component perpendicular to the axon, the axon is approximated as an cylinder with a fixed radius. Under this geometrical assumption, diffusion perpendicular to the axon is restricted by the axonal membrane. The asymptotic form of the signal attenuation for restricted diffusion, accounting for the finite duration of the diffusion gradients, was derived by van Gelderen et al. [43]. This formulation expresses the perpendicular signal attenuation in terms of cylindrical harmonics or Bessel functions, leading to:

$$S_{\perp}(q_{\perp},\Delta) = e^{-4\pi^2 r^4 {q_{\perp}}^2(\Delta-\frac{\delta}{3})D_{/\!/}} \tag{1.22}$$

where r denotes the axonal radius. This expression highlights the sensitivity of the diffusion signal at high diffusion weightings to axonal caliber, a feature that underpins the ability of the CHARMED model to probe microstructural properties beyond those accessible with conventional DTI.

1.3.6. The Soma And Neurite Density Imaging Model (SANDI)

Traditional brain microstructure imaging models include two diffusive compartments, intra-neurite and extra-neurite, where neurites are modelled by infinite cylinders of null radius embedded in the hindered extra-neurite water. The extra-neurite pool in WM corresponds to water in the extra-axonal space, whereas, in GM, this pool includes both water in the extra-cellular space and water within the cell bodies of neurons and glia, called the soma, combined into a single diffusive compartment. This model is sufficient to describe DW-MRI signal attenuation in WM and GM for diffusion weights up to b=3000 s/mm^2 (or, equivalently, 3 ms/μm^2), but it becomes inadequate at higher b values (b>3000 s/mm^2), where it fails to capture the observed signal decay [44], [45].

The SANDI model [30] addresses this limitation by incorporating a third diffusive compartment, which accounts for the unmodeled contribution of soma within GM. The SANDI model builds on the assumptions of the standard model (SM) and experimental evidence suggesting that, at short diffusion times t_d (t_d<20ms given a water bulk diffusivity of ~3 μm^2/ms and an estimated pre-exchange time >500 ms), the effects of cell membrane permeability and water exchange between intra-cellular and extra-cellular spaces are negligible [46]. Additionally, this model assumes, as tested through numerical simulations [30] that, at these short t_d, the intracellular sub-compartments, i.e. soma and neurites, can be treated as separate, non-exchanging compartments.

According to the SANDI model, the signal attenuation from the DW-MRI experiment as a function of b-value (S(b)), normalized to the image without diffusion weighting, (S(0)) is:

$$\frac{S(b)}{S(0)} = f_{ic}(f_{in}A_{in}(b) + f_{is}A_{is}(b)) + f_{ec}A_{ec}(b) \tag{1.23}$$

where f_{ic} and f_{ec} are the intra-cellular and extra-cellular relative signal fractions (for which the condition $f_{ic} + f_{ec} = 1$ is always valid), f_{in} and f_{is} are the intra-neurite and intra-soma relative signal fractions (for which the condition $f_{in} + f_{is} = 1$ is always verified), A_{in} and A_{is}, A_{ec} are

the normalized signals of the neurites, soma and extra-cellular space, respectively. To obtain orientationally independent diffusion metrics, the powder-averaged signal (that is, the average of the signal across various uniformly distributed directions) can be considered. The normalized, direction-averaged signal is indicated by $\frac{\tilde{S}(b)}{S(0)}$, comprising $\tilde{A}_{in}$ and $\tilde{A}_{is}$, $\tilde{A}_{ec}$, detailed below.

For the *extra-cellular compartment* or space, $\tilde{A}_{ec}(b, D_{ec})$ depends on the b-value and the extra-cellular diffusivity (D_{ec}, from now on simply named D_e) and can be expressed, assuming isotropic Gaussian diffusion in this compartment, as:

$$\tilde{A}_{ec}(b, D_e) \approx e^{-bD_e} \tag{1.24}$$

For the *intra-neurite compartment*, $\tilde{A}_{in}(b, D_{in})$ depends on the b-value and the axial intra-neurite diffusivity (D_{in}), which describes the diffusion of water along the length of neurites, modeled as randomly oriented cylinders or sticks with negligible radial diffusivity ($D_\perp \approx 0$). The normalized signal from neurite diffusion is thus:

$$\tilde{A}_{in}(b, D_{in}) \approx \sqrt{\frac{\pi}{4bD_{in}}}\,\mathrm{erf}\left(\sqrt{bD_{in}}\right) \tag{1.25}$$

Finally, for the intra-soma compartments, $\tilde{A}_{is}(b, D_{is}, r_s)$ depends not only on the b-value, the intra-soma diffusivity (D_{is}) and the cellular size (r_s) but also on additional parameters such as the diffusion gradient amplitude (g), the gradient pulse duration (δ), and the time between the gradient pulses (Δ). It represents the normalized signal arising from diffusion within somas, which are modeled as spheres:

$$\tilde{A}_{is}(b, D_{is}, r_s) \approx exp\left\{-\frac{2(\gamma g)^2}{D_{is}} \sum_{m=1}^{\infty} \frac{a_m^{-4}}{a_m^2 r_s^2 - 2} \times \left[2\delta - \frac{2 + e^{-a_m^2 D_{is}(\Delta-\delta)} - 2e^{-a_m^2 D_{is}\delta} - 2e^{-a_m^2 D_{is}\Delta} + e^{-a_m^2 D_{is}(\Delta+\delta))}}{a_m^2 D_{is}}\right]\right\} \tag{1.26}$$

where γ is the gyromagnetic ratio, a_m is the root of a Bessel function-related equation, and r_s quantifies the radius or apparent soma size. Parameter D_{is} characterizes water diffusion inside somas (for practical applications, D_{is} is often set to the self-diffusion coefficient of water at tissue temperature).

By substituting Eqs. (1.24), (1.25) and (1.26) into Eq. (1.23), we obtain the approximated expression for the total direction-averaged signal:

$$\frac{\tilde{S}(b)}{S(0)} = (1 - f_{ec})(f_{in}\tilde{A}_{in}(b, D_{in}) + (1 - f_{in})\tilde{A}_{is}(b, D_{is}, r_s)) + f_{ec}\tilde{A}_{ec}(b, D_e) \quad (1.27)$$

The parameters to be estimated fitting the DWI signal to Eq. (5) are five in total, as D_{is} is set to a fixed value of 3 μm²/ms (corresponding to $3*10^{-3}$ mm²/s), corroborated by numerical simulations and Pulsed Gradient Spin Echo experiments [30], while fextra (the extra-cellular intensity fraction) is equal to fextra=1-fsoma-fneurite (with fsoma equivalent to $(1-f_{ec})(1-f_{in})$ in Eq.(1.27), and fneurite equivalent to $(1-f_{ec})f_{in}$ in Eq.(1.27)).

1.4. Introduction to fMRI

Functional magnetic resonance imaging (fMRI) is a non-invasive neuroimaging technique that enables the investigation of brain function by indirectly measuring neuronal activity through haemodynamic changes. In contrast to structural MRI, which characterizes anatomical and tissue-related properties, fMRI is sensitive to dynamic physiological processes associated with neural activation and therefore enables the mapping of functional organization within the brain in vivo.

The most widely used fMRI approach is based on the blood oxygenation level-dependent (BOLD) contrast. BOLD-fMRI does not measure neuronal activity directly; rather, it reflects changes in blood oxygenation, blood flow, and blood volume that accompany local neuronal recruitment. For this reason, fMRI provides a functional readout that complements structural and microstructural MRI measures.

1.4.1. Physiological And Physical Basis of fMRI Signal

The brain, like any other organ in the human body, requires a continuous supply of oxygen to metabolize glucose and thereby produce energy. The oxygen required for metabolic processes is delivered by blood. Because oxygen is poorly soluble in water, blood contains a specialized protein capable of binding oxygen, known as hemoglobin. The functional core of hemoglobin consists of an iron atom bound within an organic structure, which also contributes to the

characteristic color of blood. When an oxygen molecule binds to hemoglobin, it is referred to as oxyhemoglobin, whereas hemoglobin not bound to oxygen is termed deoxyhemoglobin.

In 1935, it was demonstrated that the magnetic properties of hemoglobin depend on the amount of oxygen it carries[47]. This dependence has provided the basis for a method of measuring brain activity using functional magnetic resonance imaging [32], [48], [49].

1.4.2. The BOLD Mechanism

The blood oxygen level-dependent (BOLD) contrast arises from the different magnetic properties of oxygenated and deoxygenated hemoglobin. Deoxyhemoglobin is paramagnetic, whereas oxyhemoglobin is diamagnetic. The presence of deoxyhemoglobin within blood vessels generates local magnetic susceptibility differences between the vasculature and the surrounding tissue, leading to microscopic magnetic field inhomogeneities. These inhomogeneities cause additional dephasing of the proton spins and result in a reduction of the effective transverse relaxation time T_2^* [50]. In a T_2^*-weighted imaging experiment, the presence of deoxyhemoglobin within blood vessels results in darker signal intensity in voxels containing the vessels. Since oxyhemoglobin is diamagnetic and does not produce the same degree of signal dephasing, variations in blood oxygenation can be observed through signal changes in T_2^*-weighted images [37], [49], [51].

The BOLD effect depends on the interplay between multiple physiological variables, including regional cerebral blood flow (rCBF), regional cerebral blood volume (rCBV), and the cerebral metabolic rate of oxygen consumption ($\mathrm{CMRO_2}$). The sequence of events linking neuronal activation to the measured BOLD signal involves a cascade of processes, schematically illustrated in Figure 1.15. An external stimulus first induces local neuronal activity, which is accompanied by an increase in metabolic demand. This metabolic response is followed by a substantial increase in rCBF, a moderate increase in rCBV, and a relatively small increase in oxygen extraction ($\mathrm{CMRO_2}$).

The marked increase in rCBF requires vasodilation of the local vasculature and is accompanied by a concomitant increase in rCBV. Experimental studies have demonstrated a correlation between changes in rCBF and rCBV, reporting increases of approximately 30 - 70% in rCBF and 20 - 30% in rCBV during functional activation [52], [53]. These two effects influence the BOLD signal in opposite ways. While the increase in rCBF leads to a dilution of

deoxyhemoglobin and thus enhances the BOLD signal, the increase in rCBV raises the absolute amount of deoxyhemoglobin per unit tissue, partially counteracting the positive BOLD effect.

It is possible to estimate the reduction of the BOLD effect associated with the concomitant increase in regional cerebral blood volume (rCBV) to be approximately 30% of the theoretical BOLD signal change driven solely by an increase in regional cerebral blood flow (rCBF). The presence of an rCBV-related effect may also account for an additional component in the temporal evolution of the activation response, consisting of a signal decrease below baseline that follows the positive BOLD peak approximately 7 - 10 seconds after the end of stimulation (Figure 1.17).

Since changes in blood volume are generally assumed to evolve more slowly than changes in blood flow, the negative effects of an increased rCBV on the BOLD signal remain uncompensated after rCBF has returned to baseline, thereby giving rise to the observed signal undershoot [53].

The overall mechanism governing the interaction between rCBF, rCBV, and cerebral metabolism is considerably more complex. It is sufficient here to note that this interaction is not static, but varies over the course of activation, particularly during sustained stimulation [54].

Overall, the predominant increase in rCBF, in the presence of only a modest rise in oxygen extraction and a concurrent increase in rCBV, leads to an overall increase in local blood oxygenation, resulting in a positive BOLD effect (Figure 1.15). Consequently, the net outcome of neuronal activity is a regional reduction in paramagnetic deoxyhemoglobin and, therefore, an increase in the measured MR signal (Figure 1.16).

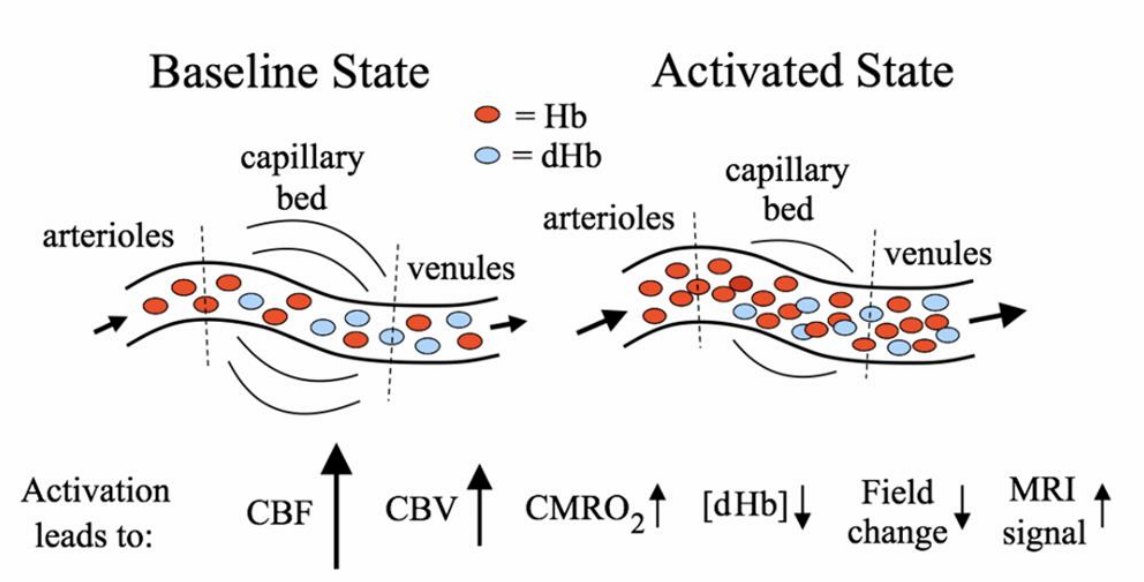


Figure 1.15. Schematic illustration of the BOLD effect. *Following neural activation, regional cerebral blood volume (rCBV) and oxygen extraction by the tissue increase, leading to a transient rise in the concentration of deoxyhemoglobin. This effect is subsequently compensated by an increase in regional cerebral blood flow in the vicinity of the activated tissue, ultimately resulting in a net increase in oxyhemoglobin concentration. Figure adapted from (Michael Chappell et al.)*

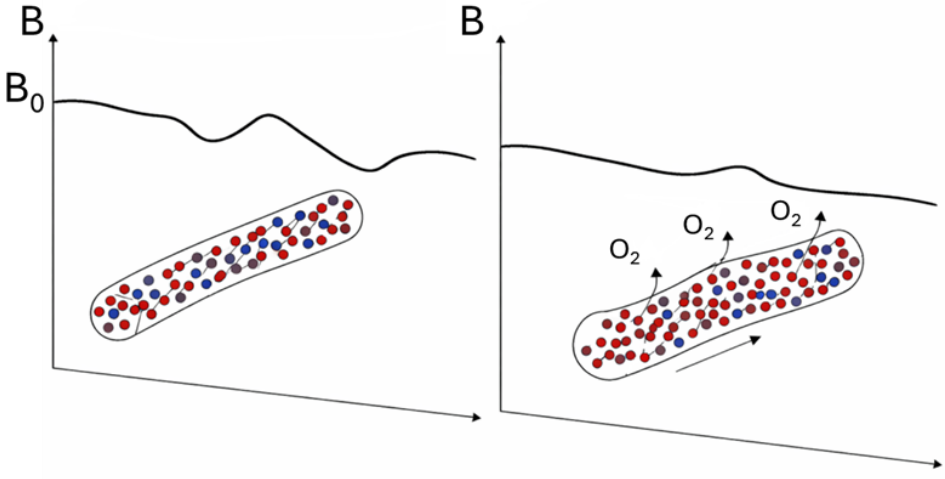


Figure 1.16. The BOLD effect. *Paramagnetic deoxyhemoglobin induces local magnetic field distortions in the vicinity of blood vessels and capillaries. During the resting state (left), blood is more deoxygenated than during activation (right), resulting in stronger local magnetic field perturbations. During activation, the reduction in deoxyhemoglobin concentration leads to decreased field inhomogeneities and, consequently, an increase in the MR signal.*

The temporal evolution of BOLD signal variations is delayed by a few seconds relative to the onset of neuronal activity and appears temporarily smoothed, reflecting changes in regional cerebral blood flow (Figure 1.17). Some recent experiments have also demonstrated a small initial signal decrease occurring approximately 150 - 300 ms after stimulus presentation, likely due to an early, uncompensated extraction of oxygen from the blood by the activated cells, which leads to a transient increase in deoxyhemoglobin concentration [31], [55]. The temporal profile of the activation response is commonly referred to as the haemodynamic response to the stimulus.

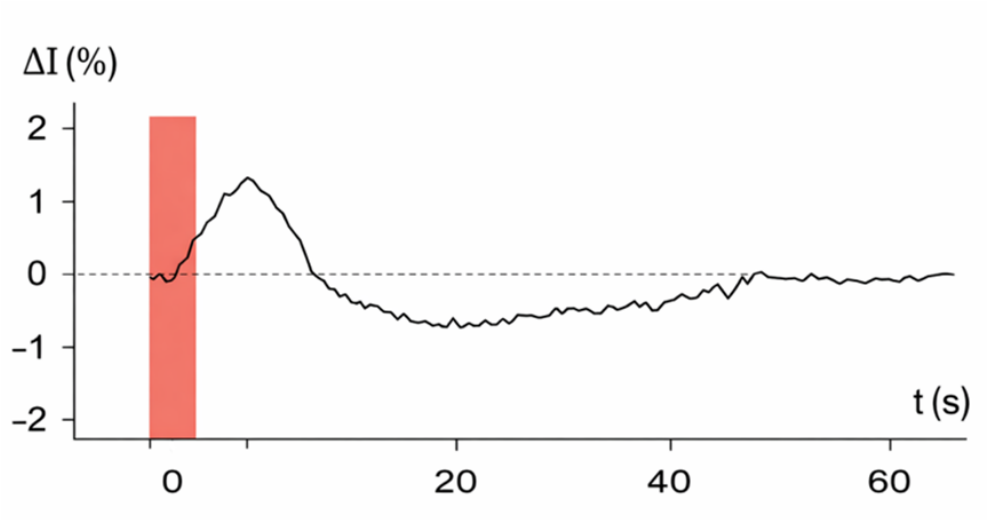


Figure 1.17. BOLD signal time course. *Typical temporal evolution of the BOLD signal in an fMRI experiment, with the stimulus indicated by the red bar.*

1.4.3. Functional Mapping with fMRI

To investigate brain function using fMRI, repeated whole-brain scans (volumes) are acquired while the participant is exposed to sensory stimulation or performs a specific task. Functional mapping relies on detecting small, stimulus-related changes in the BOLD signal over time, making fMRI an inherently dynamic imaging technique. The success of an fMRI experiment depends on three main factors: the imaging sequence employed, the design of the experimental paradigm, and the methods used for data analysis.

The strength of the static magnetic field plays a critical role in determining the magnitude of BOLD signal changes observed during activation. This is because magnetic susceptibility differences, which underline the BOLD contrast, induce stronger signal dephasing at higher

magnetic field strengths. While many fMRI studies have traditionally been conducted at 1.5 T, advances in MRI technology have enabled the use of high-field scanners operating at field strengths up to 7 T in cutting-edge research. With increasing field strength, the BOLD contrast increases more rapidly than the intrinsic system noise, resulting in improved sensitivity to functional activation.

A key requirement of fMRI acquisition sequences is that they provide strong T_2^*-weighting. Most fMRI studies therefore employ echo planar imaging (EPI), which enables rapid image acquisition and allows the detection of haemodynamic responses to brief stimuli. In addition to its high temporal efficiency, EPI offers the advantage of reduced sensitivity to subject motion, which is particularly important in functional imaging experiments.

The degree of T_2^*-weighting in the acquired images is governed primarily by the echo time (TE). If the TE is too short, the difference between the T_2^* decay curves corresponding to the activated and resting states is small, resulting in limited BOLD sensitivity. Conversely, if the TE is too long, signal loss due to transverse relaxation may reduce the signal intensity in both conditions. To maximise the BOLD signal change in a tissue with a given T_2^* value, the optimal TE should be approximately equal to the T_2^* of that tissue (Figure 1.18).

In addition, the contrast-to-noise ratio (CNR) of the BOLD signal depends on voxel size and slice thickness. Smaller voxels contain fewer spins and therefore yield lower signal intensity, whereas larger voxels may suffer from partial volume effects, which can reduce CNR. Partial volume effects arise when activation-related signal changes originate from only a small subregion within a voxel, thereby diminishing their contribution to the overall signal variation measured in that voxel.

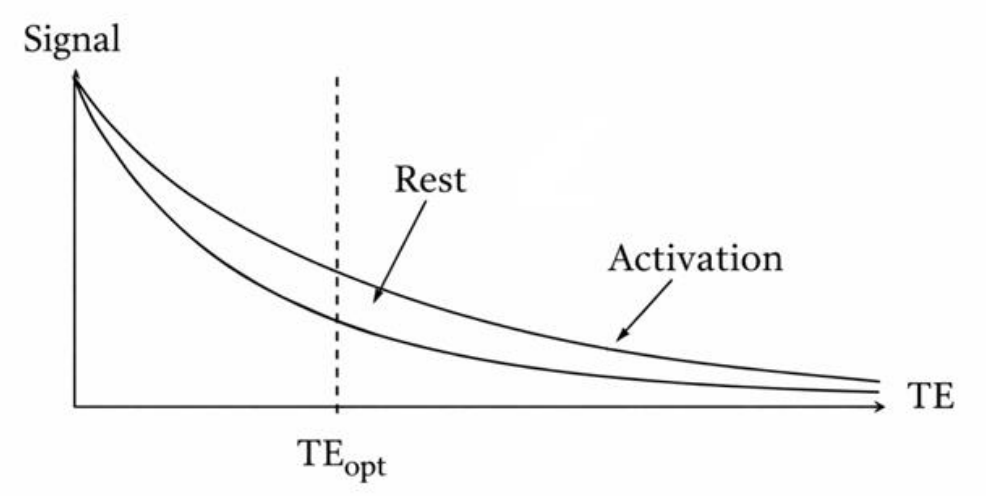


Figure 1.18. Optimal echo time (TE) for the BOLD effect. *Dependence of the BOLD signal on echo time, illustrating the optimal TE at which the signal difference between rest and activation is maximized.*

1.4.4. The fMRI Experiment

An fMRI experiment involves the presentation of stimuli capable of eliciting a neuronal response. In many fMRI experiments, participants do not merely perceive a stimulus passively but are required to perform a specific task. In general, fMRI data are analyzed by comparing different states of neuronal activity defined by the stimulation conditions that generate them.

Task-based fMRI therefore relies on detecting condition-related changes in the BOLD signal over time, typically by contrasting task and control or rest conditions. A variety of experimental designs can be used depending on the aims of the study and on the temporal characteristics of the expected haemodynamic response. The specific visuomotor learning paradigm used in this thesis is described in detail in Chapter 3.

2. Exploring the Contribution of Grey Matter Microstructure to R1 Contrast via Multi-Compartment Diffusion Modelling in the Healthy Brain

This chapter tests the hypothesis that, in healthy volunteers, diffusion metrics with high sensitivity to cortical grey matter (GM) microstructure, derived from high b-value diffusion-weighted data using the three-compartment Soma and Neurite Density Imaging (SANDI) model, are significantly associated with the longitudinal relaxation rate R1 (1/T1), a quantitative marker sensitive to myelin-related cortical tissue properties. For completeness and comparison, associations in white matter (WM) are also reported.

The results presented in this chapter formed the basis of an article published in NeuroImage [56].

Abstract

The Soma And Neurite Density Imaging (SANDI) model extends the sensitivity of MRI-derived water diffusion metrics to grey matter (GM) microstructural complexity. In this work, we investigated the hypothesis that the diffusion metrics derived from the three-compartment SANDI model contribute to the longitudinal relaxation rate R1 (1/T1) contrast in brain tissue. To this aim, twenty healthy volunteers underwent diffusion-weighted imaging and quantitative R1 mapping using MP2RAGE sequence at 3 T.

Specifically, we investigated the association between SANDI-derived diffusion metrics and R1 in the healthy brain by examining voxel-wise and regional correlations between SANDI

metrics and R1, a quantitative marker sensitive to myelin-related cortical tissue properties, within cortical GM. For completeness and comparison, associations observed in white matter (WM) are also reported. The diffusion metrics included intra-neurite signal fraction (fneurite), intra-soma signal fraction (fsoma), extra-neurite fraction (fextra), soma radii (Rsoma), and intra-neurite and extra-neurite diffusivities (D_{in} and D_e).

In GM, a moderate negative spatial correlation was observed between R1 and soma-related metrics, namely fsoma and Rsoma (r = -0.47, -0.35, respectively), indicating that GM microstructure contributes to R1 contrast. These findings are consistent with evidence of structural heterogeneity in the cortex, where variation in myelin-related and other microstructural tissue properties may contribute to differences in neuroplasticity. Notably, similar effects and trends were identified when evaluating across subjects' correlations of the metrics of interest (fsoma and Rsoma, with r = -0.56, -0.48, respectively).

In WM, moderate to strong positive spatial correlations were observed between R1 and intra-neurite metrics, specifically D_{in} and fneurite, (r = 0.53 and 0.30, respectively), reflecting the contribution of myelinated axons to the intra-neurite water pool.

Overall, these results suggest that both GM and WM microstructural characteristics contribute to R1 contrast, with R1 reflecting, among other factors, myelin-related and other microstructural tissue properties within brain tissue. These findings contribute to a more detailed understanding of regional relaxation differences across the brain parenchyma. Future studies should explore whether these relationships are preserved in clinical populations with demyelination and neurodegeneration.

2.1. Introduction

The myelin sheath, generated from the oligodendrocyte membranes wrapping around axons, plays a critical role in ensuring the efficient transmission of electrical signals between neurons. While it is traditionally associated with white matter (WM), significant amounts of myelin are found in the cortical grey matter (GM), where it may affect the organization and functional dynamics of intracortical circuits by stabilizing connections and limiting synaptic plasticity [57]. The mechanisms and functions of cortical myelination still need to be fully understood. Current hypotheses suggest that GM myelination plays a key role in neuroplasticity [57], i.e. the brain's ability to adapt and reorganize itself in response to learning, experience, or injury,

and contributes to shaping neural pathways and supporting cognitive and motor functions. On the other hand, in diseases such as Multiple Sclerosis, cortical demyelination is associated with disease progression and worsening pathology [58], and even at the earliest stages of the disease, aberrant GM myelination correlates with clinical impairment [59].

Myelin alters the magnetic properties of brain tissues by shortening T1, the MRI longitudinal relaxation time (T1), which depends on the local microstructural properties such as macromolecular components, iron, and water content [60], [61], [62]. A relationship of proportionality between R1 and brain myelin content has been demonstrated with higher myelin content resulting in larger R1 values [19], [63], [64]. Additionally, there is strong evidence of correspondence between histological data and myelin patterns in the cortex observed via T1-weighted high-resolution MRI [65], which can detect distinct myelination patterns across the cortex [22]. As a result, R1 mapping has been widely adopted as a non-invasive quantitative marker sensitive to myelin-related tissue contrast in vivo. [66]. However, R1 is not uniquely specific to myelin, as it is also influenced by the water-to-macromolecule ratio (i.e. effectively, tissue water content) and by iron, both of which may confound its interpretation in terms of myelin content [67].

In macromolecule-rich environments such as brain tissue, water can be found in different states within macromolecular systems, including free, unbound water, water associated with hydration layers at the surface of macromolecules, and crystalline water confined within macromolecular structures. In addition, the hydration layer can be divided into two types: specific absorbed water which is bound tightly to the macromolecular structure, and general hydration water, which is more loosely bound [68].

The longitudinal relaxation rates that we can measure in brain parenchyma through MRI are influenced by the ratio of hydrogen in free water relative to that inside the macromolecules or on their surface (de Boer RW, 1995). The restricted movement of water associated with macromolecules, compared to free water, results in a subset of water experiencing static magnetic fields (increasing the transverse relaxation rate R2) and interactions at frequencies near the Larmor frequency (increasing R1). The extent of R1 and R2 lengthening depends on the concentration of macromolecules, their size, and the quantity of hydrophilic groups (including amines, hydroxyls, and carboxyl groups) capable of binding water molecules [69]. As detailed in Fullerton et al. . [68], the crystalline component can be discarded in the limit of fast exchange, and only the free water and the hydration layer contribute substantially to the longitudinal relaxation rate. In summary, R1 is influenced by multiple factors, including water

content, iron concentration [61], macromolecular composition, and tissue microstructure, such as axonal size and axonal density in WM [62] as well as other constituents contributing to the effective constant in the solvent model.

In addition to influencing the tissue longitudinal relaxation rate because of its macromolecular structure, the presence of myelin in the voxel of tissue reduces the amount of free diffusion in that voxel, as axons are covered by a lipid protein bilayer, which hinders and restricts water diffusion. This latter mechanism is thought to originate from multiple diffusive compartments [70]. Indeed, water diffusion varies within the brain parenchyma, exhibiting isotropic behaviour in GM and anisotropic properties in WM regions, characterized by densely packed myelinated fibres. By exploiting the endogenous contrast provided by self-diffusion of water molecules in tissues, diffusion-weighted MRI (DW-MRI) can be used to probe the microstructure of biological tissues permitting the study of brain development [71] and the assessment of structural integrity in normal and pathological states [72], [73], [74], [75].

The mathematical models that parameterize brain tissue microstructure from diffusion signals necessarily simplify the underlying cellular geometry, which may limit the accuracy and completeness of microstructure estimation [76]. Additionally, several key factors need to be considered for GM: water exchange across the cell membrane - between neurites and the extracellular space [77], [78]; non-Gaussian diffusion along neuronal and glial processes - resulting from structural disorder [79], [80]; the signal contribution from soma [30]. Traditional diffusion models have historically schematized neural tissue as a combination of two diffusive compartments: one corresponding to the confined space within the neurites (intra-neurite compartment), the other including the water diffusing in the extra-cellular space (extra-neurite compartment). However, recent studies have shown that the ‘Standard Model’ of diffusion (SM) with its two compartments fails in representing diffusion signal attenuation at high b-values [44], [45]. As a result, diffusion MRI in GM requires ‘rethinking the basic microstructure modeling blocks’ to more accurately reflect the complex interplay between cellular compartments and diffusion processes [77]. More recently, the intra-soma compartment (including neurons and neuroglia) was added in the Soma And Neurite Density Imaging (SANDI) diffusion model [30]. This model is particularly promising for studying cortical architecture and cortical myelination in that it describes water diffusion within tissue compartments more comprehensively.

Given these considerations, we hypothesized that GM microstructural characteristics, particularly its cytoarchitecture, contributing to R1 contrast, determined an association between

SANDI-derived diffusion metrics in GM and R1. For completeness, we also investigated such associations in WM. Towards this aim, we decided to employ the Magnetization Prepared 2 Rapid Acquisition Gradient Echo (MP2RAGE) sequence (Marques et al., 2010) for R1 mapping as it is becoming increasingly widespread in research and it is a clinically viable approach, considering its contained acquisition time.

This study aims thus to determine whether specific microstructural properties captured by the SANDI model corresponded to variations in R1, which depends, among other things, on the myelin content.

By establishing these relationships, our study seeks to clarify the contribution of cytoarchitecture to R1 contrast, providing new insights into how neuronal architecture and myelin content interact in the healthy brain.

2.2. Methods

2.2.1. Data acquisition

Participants

The study participants were 20 healthy adult volunteers (9 males and 11 females). The age range was 24 – 31 years (mean = 27.5 years; standard deviation (SD) = 3.8 years). Handedness was not formally recorded in this cohort. Participants provided written informed consent, and they were screened for MRI compatibility. None of the subjects had a history of neurological disease, psychological disorders, drug or alcohol abuse, or use of neuropsychiatric medication. Participants were instructed to maintain their usual intake of food, drink (including alcohol), and caffeine on the day of the study. The study was approved by the Cardiff University School of Psychology Ethics Committee.

MRI protocol

The imaging protocol was conducted on a Siemens Prisma 3T scanner (Siemens Healthineers, Erlangen, Germany) at the Cardiff University Brain Research Imaging Centre (CUBRIC), using a 32-channel, receive-only head coil. All participants underwent a protocol including diffusion-weighted imaging (DWI) with varying gradient strengths and quantitative R1

mapping via Magnetization Prepared 2 Rapid Acquisition Gradient Echo (MP2RAGE) sequence [23], with detailed sequence parameters listed in Table 2.1.

The MP2RAGE sequence models R1 assuming that water exchange between free water and water bound to macromolecules is negligible, and that each voxel comprises a single spin pool of water molecules, whose signal recovery after excitation can be theoretically described by a mono-exponential behavior.

DWI included six non-zero b-shells with increasing diffusion directions at higher b-values and 13 b0 volumes acquired with phase-encoding in an anterior-posterior direction. In addition, an image with no diffusion weighting but an opposite phase-encoding direction was acquired for susceptibility distortion correction. b-value shuffling was adopted to avoid excessive gradient coil heating [81].

Table 2.1. Sequence details. *Overview of parameters for Diffusion - Weighted Imaging (DWI) and R1 protocols.*

Parameter	DWI Protocol	R1 mapping Protocol
Total DWI Volumes	266	-
Diffusion Directions/Volumes per b-shell	13 / 20 / 20 / 30 / 61 / 61 / 61	-
Diffusion Weightings (b-values)	0 / 200 / 500 / 1200 / 2400 / 4000 / 6000 s/mm²	-
Acquisition Method	Double-refocused spin-echo DW echo-planar imaging	MP2RAGE
Repetition Time (TR)	3000 ms	5000 ms
Echo Time (TE)	85 ms	2.36 ms
Flip Angle (FA)	50°	FA1 = 7°, FA2 = 5°
Refocusing Flip Angle	180°	-
Diffusion Gradient Separation (Δ)	40 ms	-
Diffusion Gradient Duration (δ)	28 ms	-
Resolution	2.5-mm isotropic	1-mm isotropic
Number of Slices	42	160
Field of View (FOV)	220 x 220 mm²	224 x 224 mm²
Bandwidth	1496 Hz/pixel	350 Hz/pixel
GRAPPA Acceleration	2	2
Inversion Times (TI)	-	TI1=700 ms, TI2=1500 ms
Echo Spacing	0.75 ms	5.8 ms
Slice orientation	Transversal	Sagittal
Scan duration	13.48 min	7.55 min

GRAPPA=GeneRalized Autocalibrating Partial Parallel Acquisition; DW=diffusion weighted; MP2RAGE=Magnetization Prepared 2 Rapid Acquisition Gradient Echoes.

2.2.2. Data processing

Diffusion weighted images (DWIs) were denoised [82] and corrected for Gibbs ringing artifacts with MRtrix3 [83]. The b0-images acquired in opposite phase encodings were used to estimate the susceptibility induced distortions via FSL TOPUP (FSL, FMRIB Software Library, v6.0.1 [84]). FSL BET was used to provide a binary mask to FSL EDDY, which was employed to correct for eddy-current induced distortions and subject motion, exploiting the output from TOPUP. A diffusion data quality check was conducted via the evaluation of the signal-to noise ratio, using in-house MATLAB scripts (MATLAB version: R2022b, Natick, Massachusetts: The MathWorks Inc). MATLAB was also used to derive a map of apparent R1 (apparent due to the single compartment assumption; thereafter, simply named R1) from the quantitative T1 map produced by the MP2RAGE sequence, and for the correlation analysis, detailed below. FSL DTIFIT was used to extract the diffusion tensor using b-values up to 1200 s/mm^2, yielding mean diffusivity and fractional anisotropy (FA) maps, and the tensor eigenvalues and eigenvectors. FA maps were later used for parcellation of white and grey matter.

The SANDI toolbox (https://github.com/palombom/SANDI-Matlab-Toolbox-Latest-Release) was used to estimate via a Machine Learning approach based on Random Forest Regression, five model parameters: *fsoma* (equivalent to $(1-f_{ec})(1-f_{in})$ in Eq.(1.26)), *fneurite* (equivalent to $(1-f_{ec})f_{in}$ in Eq.(1.26)), the signal fractions of intra-soma and intra-neurite compartments (the extra-neurite signal fraction *fextra* was computed from them as *fextra*=1-*fsoma*-*fneurite* and corresponds to f_{ec} in Eq. (1.26)); D_{in}, D_e, the apparent diffusivity of intra-neurite and extra-neurite compartment; *Rsoma* (r_s), the estimated magnetic resonance (MR) apparent radius of soma and/or cellular bodies (e.g. glia).

Signal to noise ratio of DWIs

A critical aspect to consider when analyzing DWI data is the reliability of the acquired signal. Indeed, noise can introduce bias into the estimated diffusion metrics [85]. To ensure robust data quality, the signal-to-noise ratio (SNR) of the DW images was evaluated. Conventionally,

SNR is evaluated for each diffusion-encoded volume and thus, each b-value, allowing to verify whether the measured signal falls below the noise floor at the highest b-value [72]. SNR is calculated as the ratio between the diffusion signal in WM and GM and the standard deviation of the noise in the background. This approach (hereafter referred to simply as SNR) provides an overall measure of signal reliability across the dataset. To this aim, the SNR averaged across subjects for each diffusion direction was calculated. However, because of the use of parallel imaging and a multi-channel receiver head coil, SNR was evaluated also following the definition proposed by Dietrich et al. (2007) [86], employing two raw, uncorrected images without diffusion weighting, or b=0 s/mm^2 images. Because the method considers the difference between two consecutive b0 images, it will be referred to as SNR_{diff} hereafter. The SNR_{diff} was thus defined as:

$$SNR_{diff} = \frac{1}{\sqrt{2}} \frac{mean_{ROI}(S_1(b=0)+S_2(b=0))}{std_{ROI}(S_1(b=0)-S_2(b=0))} \quad (2.1)$$

where S_1(b=0) and S_2(b=0) represent the signal in the first two consecutive $b = 0$ s/mm^2 images acquired. The two SNRs were calculated in two regions of interest (ROIs), namely the WM and GM, and were reported as the mean ± standard deviation. The corpus callosum was chosen because, due to the presence of highly coherent WM fibres, it represents a region where the diffusion is highly facilitated along the fibre directions (corresponding roughly to the left-right direction) and highly hindered in the perpendicular directions. Therefore, considering the direction of facilitated diffusion, it may represent the worst-case scenario in the SNR evaluation.

The FA maps were used to mask the corpus callosum for SNR evaluation and normalization of the parametric maps to the standard Monreal Neurological Institute (MNI) space. For SNR calculation, the corpus callosum was selected in an automated way, by retaining voxels with FA larger than 0.75 and with the first eigenvector (V1) magnitude larger than 0.9 to allow the selection of coherent WM fibers and to avoid partial volume effects at the borders. For the same reason, GM was selected in an automated way by retaining voxels with FA comprised between 0.15 and 0.38. These thresholds were set empirically considering the average FA and V1 values in the respective tissues of interest (the corpus callosum and GM) and were applied only for SNR evaluation purposes. Noise was evaluated in the background by automatically selecting four squares at the corners of the image (size of the square was roughly 1/5 of the matrix size). The code is available at https://github.com/caporaleas/SNR_DWI.

Parametric maps normalization and white and grey matter parcellation

The FA map was registered to the anatomical T1-weighted image via rigid body transformation. The structural image was normalized to the MNI-2-mm space via non-linear transformation. These transformations were combined to obtain the warps that mapped the FA onto the MNI standard space, and the warps were applied to the R1 and SANDI parametric maps. A hard segmentation of the T1-image was used based on the absolute maximum partial volume estimate, obtaining masks of GM and WM, which were further eroded. For cortical parcellation, the Human Connectome Project atlas, including 180 regions of interest (ROIs) [87], was used. In this atlas information related to the architecture, topography, function and connectivity of the GM areas were used to obtain the cortical parcellation. The analysis was restricted to cortical grey matter (GM) due to the atlas chosen for cortical parcellation. In Supplementary Materials we reported the results of an analysis including also subcortical structures. The ICBM-DTI-81 [88] atlas, including 50 ROIs, was used instead for WM parcellation. GM and WM ROIs exceeding the 20^{th} percentile in voxel count were retained to exclude residual noise. Voxels with cell density (*fsoma*) higher than 0.1 were retained ensuring brain parenchyma selection and a reliable estimate of Rsoma in the parenchyma [89].

2.2.3. Statistical Analysis

The median regional values of SANDI and parametric maps of R1 were evaluated across subjects and across ROIs, with standard deviations and errors. Pearson's correlation was evaluated between the regional values of R1 and SANDI metrics, correcting for multiple comparisons (using Benjamini-Hochberg false discovery rate criterion, thereafter, simply named FDR). The distribution of correlation coefficients was also evaluated across subjects. In the correlation between SANDI metrics and R1 across ROIs the effect of several potential confounders (ROI volume, the cortical thickness and curvature for GM, and ROI volume only for WM) was evaluated. The ROI volume was expressed as the number of voxels constituting the GM or WM ROI. The cortical thickness and the curvature were estimated using FreeSurfer (FreeSurfer [90], v7.3.2) for each ROI of the HCP atlas, considering then the median across subjects. A regression analysis was performed using the 'General Linear Model' (fitglm) in MATLAB and employing standardized variables. The model tested for the GM ROIs was the following:

$$SANDImetric_i = \beta_0 + \beta_1 \cdot R1_i + \beta_2 \cdot C1_i + \beta_3 \cdot C2_i + \beta_4 \cdot C3_i + \varepsilon_i \quad (2.2)$$

Where C1, C2 and C3 were the ROI volume, the cortical thickness and the curvature, respectively. The model tested for the WM ROIs included a single confounding factor, the ROI volume:

$$SANDImetric_i = \beta_0 + \beta_1 \cdot R1_i + \beta_2 \cdot C1_i + \varepsilon_i \quad (2.3)$$

A conservative p-value of p'=0.05/6=0.0083, with 6 the number of SANDI metrics was considered as statistically significant, to control for the family-wise error rate.

Mean values +/- standard deviations of R1 and SANDI metrics were evaluated in GM and WM without any threshold, using the binarized partial volume estimate maps, to enable comparison with other studies. The code is available at https://github.com/caporaleas/STR_CORR.

2.3. Results

No subject was excluded due to severe movement or ringing artifacts, leading to a dataset of 20 healthy subjects.

The calculated mean SNR_{diff} values were 28.56 ± 5.11 for GM and 29.77 ± 4.01 for WM, indicating a comparable level of data quality across both tissue types and to recent studies in healthy subjects at 3T [91]. The conventional SNR evaluated in the corpus callosum (CC) and in the GM for each b-value is shown in Figure 2.1. The across-subject average was calculated for each distinct diffusion direction. Notice the spread of SNR values in the CC (and not in the GM) due to the inhomogeneous diffusion attenuation depending on the diffusion sensitizing gradient direction. This is caused by the directionality of the diffusion phenomenon in WM. Even for the diffusion direction with the highest signal attenuation (that is [1 0 0], corresponding to the orientation of the most coherent fibers in the corpus callosum) the SNR remains above the inferior limit allowed for the reliability of DW data (SNR=3), according to Jones et al. [92].

Parametric maps of R1 and SANDI metrics obtained in the current study, normalized to the standard MNI space and averaged across subjects are shown in Figure 2.2. The intensity fractions of the three diffusive compartments (neurites, cellular bodies or soma, and extra-

cellular space) are shown, together with the quantitative maps of average soma size, and the diffusivities of the intra-neurite and extra-neurite domains.

R1 ranged between a value of 0.77 ± 0.02 s^{-1} to 1.11 ± 0.03 s^{-1} in GM and WM, respectively. On average, GM presented signal fractions of the soma, extra-neurite and intra-neurite compartments of 0.41 ± 0.01, 0.36 ± 0.01 and 0.19 ± 0.01, respectively. On average, in WM the largest signal fraction originated from the neurite compartment (fneurite=0.41 ± 0.02), followed by the signal fraction of the extra-neurite and the soma water pools (0.31 ± 0.01 and 0.27 ± 0.01, respectively). The estimated soma radius showed minimal differences between GM and WM (Rsoma=13.00 ± 0.14 in GM and 13.08 ± 0.17 μm in WM). Regarding diffusivity measures, the intra-neurite diffusivity (D_{in}) was 1.75 ± 0.02 μm²/ms in GM and 1.87 ± 0.02 μm²/ms in WM, while the extra-neurite diffusivity (D_e) was 1.90 ± 0.06 μm²/ms in GM and 1.64 ± 0.06 μm²/ms in WM.

Scatter plots of R1 and SANDI metrics across ROIs are shown in Figure 2.3. Since R1 presents different ranges of values for GM and WM, the correlation plots for these two tissue types were illustrated separately. For each ROI, the marker indicates the median value for that ROI, plotted against the median value of R1 across subjects. Correlation analyses revealed a moderate negative association between R1 and soma-related parameters in GM ROIs, with R1 negatively correlated with fsoma ($r=-0.51$, $p < 0.0001$) and Rsoma ($r=-0.47$, $p<0.0001$). Additionally, R1 showed a positive correlation with fextra and D_e ($r=0.38$, $p<0.0001$) but only a weak association with neurite density (fneurite, with $r=0.18$, FDR-adjusted $p=0.028$, data not shown) while no significant relationship was found with neurite diffusivity (D_{in}). The scatter plots of the SANDI parameters and R1 across ROIs including the subcortical structures are shown in the Supplementary Materials. The inclusion of the subcortical structures increased the entity of the correlation between the signal fraction of soma and neurite compartments (fneurite, fsoma) and R1. In particular, the correlation between fneurite and R1 became statistically significant with the inclusion of the subcortical structures. On the other hand, the correlation between Rsoma and R1 decreased.

Within WM ROIs, moderate to strong positive correlations were observed between R1 and intra-neurite metrics, with D_{in} ($r=0.62$, $p< 0.0001$) and fneurite ($r=0.43$, FDR-adjusted $p=0.019$. The ROI volume was not related to R1 in GM ($r=0.05$ and $p=0.52$, Supplementary Materials, Figure S4a) but it was related with R1 in WM ($r=0.47$, $p=0.002$). The cortical thickness was not related to R1 in GM ($r=-0.08$, $p=0.32$, Figure S4b), and the curvature was weakly related to R1 in GM ($r=0.17$, $p=0.046$, Figure S4c). The estimated beta coefficients of the regression

analysis with the respective p-values are reported in Table 2.2. For the WM only the fneurite and Din were included as dependent variables because the other diffusion metrics did not show a significant correlation with R1 in the original analysis. A conservative p-value of p'=0.05/6=0.0083, with 6 the number of SANDI metrics was considered as statistically significant, to control for the family-wise error rate. A significant p-value of the β_1 coefficient indicates that there is a linear relationship between the specific diffusion metric and R1 that is not explained by the confounding factors included in the model. In the GM, the correlations between fsoma and R1, fextra and R1, Rsoma and R1 and De and R1 remained significant after including the confounding factors. In the WM, the correlation between fneurite and R1 was not significant after including the ROI volume but the correlation between the intra-neurite diffusivity (Din) and R1 remained significant.

The subject-wise spatial correlation coefficient between SANDI metrics and R1 in both GM and WM is illustrated in Figure 2.4. Including the subcortical structures did not affect significantly the results of the correlations between SANDI metrics and R1 across subjects, as shown in Figure S3. The scatter plots of global GM R1 and SANDI metrics across subjects are shown in Figure 2.5. Each marker represents the median across regions of a given parameter for a different subject. A positive correlation was observed between fneurite and R1 (r=0.67, FDR-adjusted p=0.0056), while fsoma and R1 exhibited a negative correlation (r=-0.56, FDR-adjusted p=0.024). Additionally, a negative trend was noted between Rsoma and R1 (r=-0.48, FDR-adjusted p=0.056). The distributions of correlation coefficients between R1 and SANDI metrics across subjects, for each grey matter ROI, are shown in Figure 2.6.

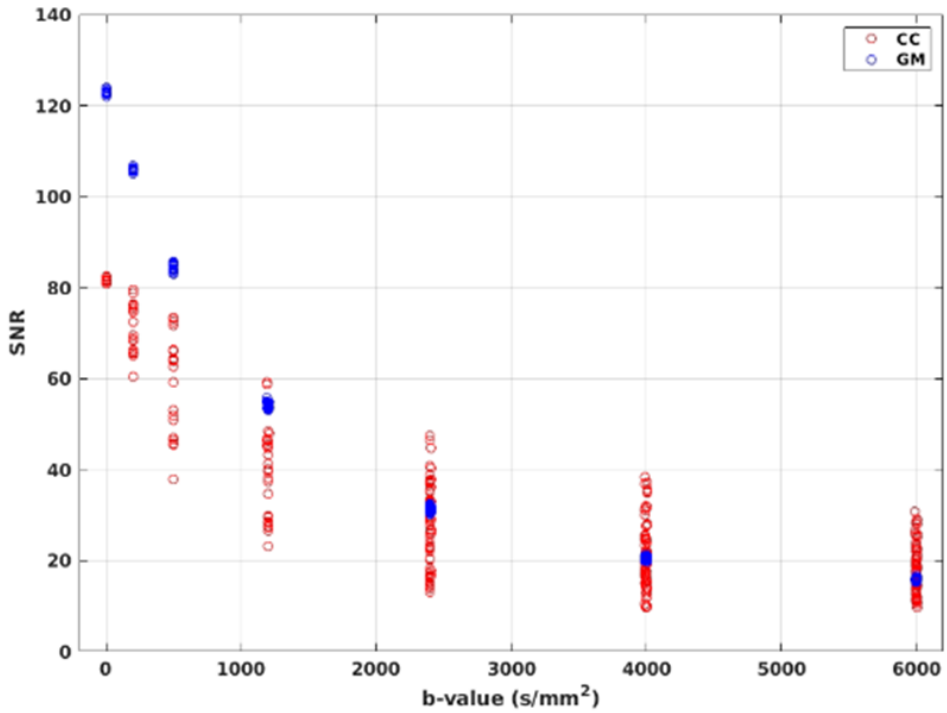


Figure 2.1. Signal-to-noise ratio (SNR) of diffusion-weighted images. *The SNR evaluated for each diffusion volume (averaged across subjects) is plotted against the b-values for the corpus callosum and grey matter (CC and GM, shown in red and blue, respectively). Experimental points represent the mean SNR across subjects.*

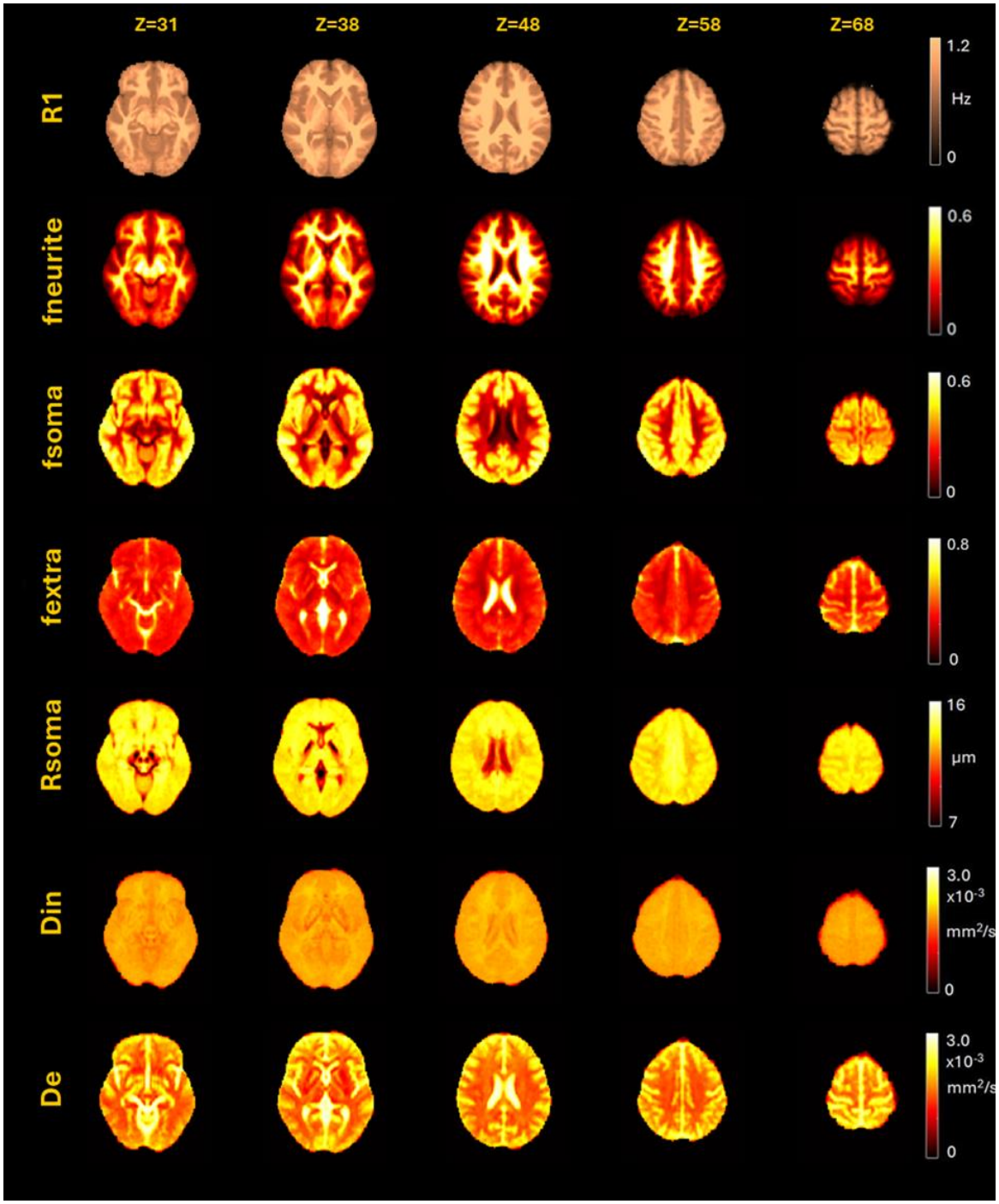


Figure 2.2. Group average parametric maps. *Parametric maps of R1 and SANDI metrics normalized to MNI space and averaged across all subjects. R1 = 1/T1, relaxation rate; fneurite = signal intensity fraction of neurite compartment; fsoma = signal intensity fraction of cellular compartment; fextra = signal intensity fraction of extra-cellular compartment; Rsoma = average size of cellular bodies; Din = diffusivity of the intra-neurite compartment; De = diffusivity of the extra-neurite compartment. The different slices correspond to axial sections at different Z-coordinates (Z = 31, 38, 48, 58, 68) in MNI space.*

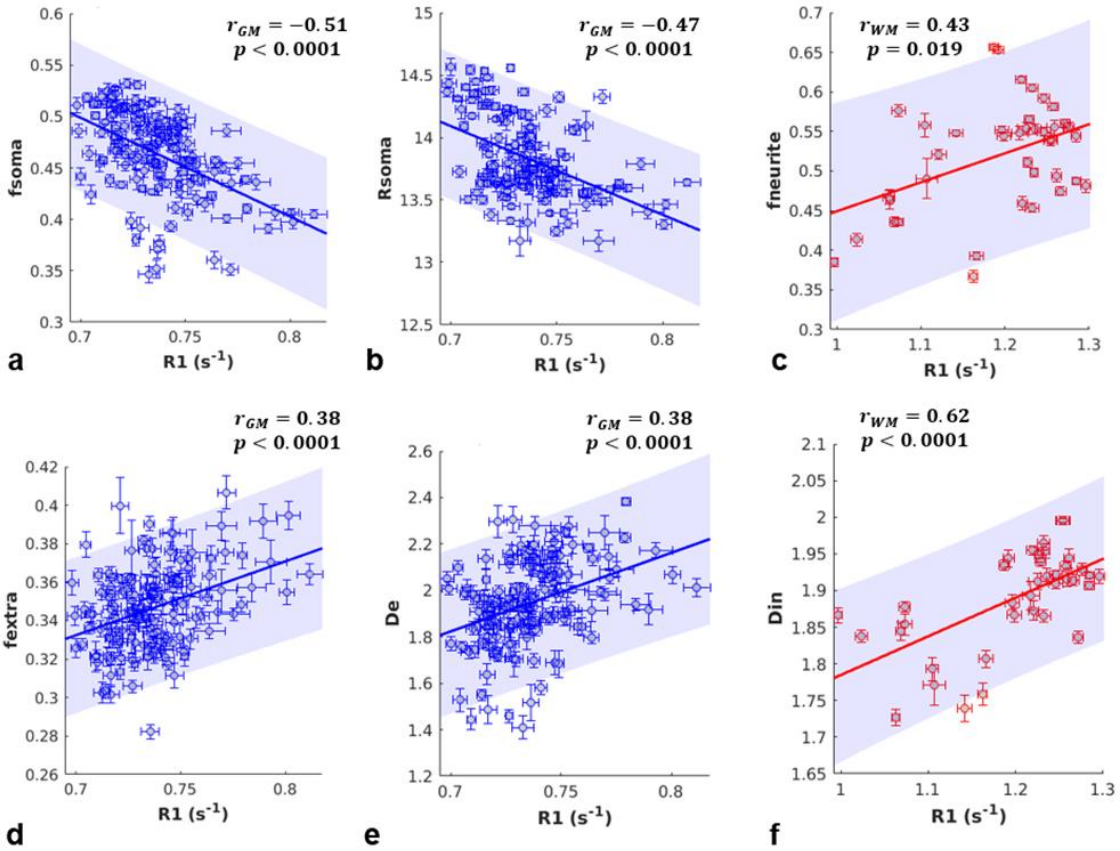


Figure 2.3. Scatter plots of SANDI metrics vs R1 in Grey and White Matter regions (GM and WM, respectively). *The Pearson's correlation coefficient between R1 and SANDI metrics quantified in GM and WM regions is indicated (with FDR-adjusted p-values shown). Each marker represents, for a different brain region, the median across subjects of the regional median of the parameter. Error bars are standard errors (median absolute deviations/squared root of number of subjects). Markers and regression lines are shown in blue and red for GM and WM, respectively. Shaded areas represent 95% confidence intervals.*

Table 2.2. Beta coefficients of the regression analysis performed in GM considering the model in eq.7 and in WM considering the model in eq.8. The respective p-value is indicated in parentheses.

	SANDI metric	β_0 (intercept)	β_1 (R1)	β_2 (ROI volume)	β_3 (cortical thickness)	β_4 (curvature)
GM	**fneurite**	0.0088 (0.92)	0.19 (0.024)	-0.0081 (0.92)	0.14 (0.087)	-0.028 (0.75)
	fsoma	0.0042 (0.96)	**-0.47 (<0.0001)**	-0.039 (0.61)	-0.14 (0.056)	0.050 (0.53)
	fextra	-0.010 (0.89)	**0.39 (<0.0001)**	0.0032 (0.97)	0.11 (0.16)	-0.026 (0.75)
	Rsoma	0.0061 (0.94)	**-0.35 (<0.0001)**	-0.10 (0.19)	0.13 (0.09)	-0.027 (0.75)
	Din	0.0072 (0.93)	-0.097 (0.26)	-0.012 (0.89)	0.019 (0.83)	0.035 (0.70)
	Dextra	-0.0076 (0.92)	**0.42 (<0.0001)**	0.054 (0.49)	-0.11 (0.14)	-0.061 (0.45)
WM	**fneurite**	<0.0001 (1)	0.30 (0.069)	0.27 (0.098)	-	-
	Din	<0.0001 (1)	**0.53 (0.0003)**	0.27 (0.052)	-	-

fneurite = signal fraction of the neurite compartment; fsoma = signal fraction of the soma compartment; fextra = signal fraction of the extra-neurite compartment; Rsoma = average size of cellular bodies; Din = intra-neurite diffusivity; De = extra-neurite diffusivity; GM = grey matter; WM = white matter

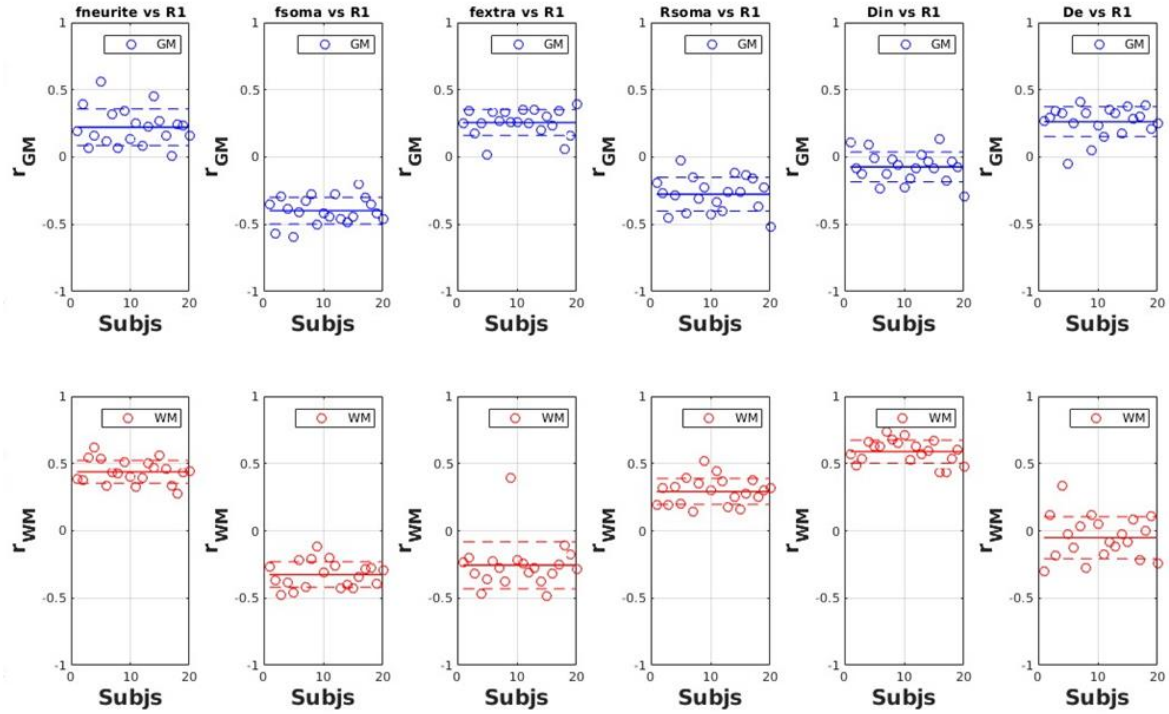


Figure 2.4. Subject-wise correlation coefficient between SANDI metrics and R1. *Each marker represents the correlation coefficient between SANDI metrics and R1 in the Grey Matter (GM) or White Matter (WM) regions, for each subject. The grand mean +/- standard deviation of r are indicated by the thick and dashed lines, respectively.*

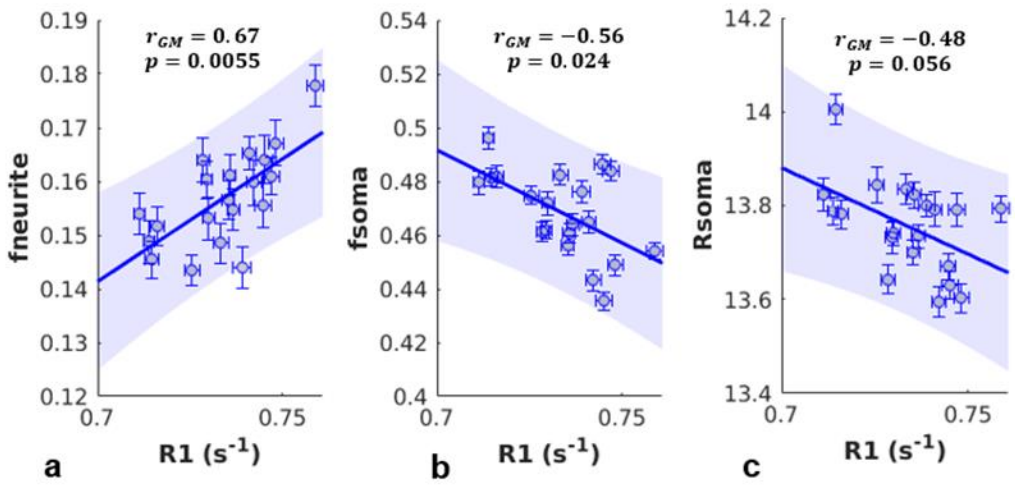


Figure 2.5. Scatter plots of SANDI metrics vs R1 in Grey Matter across subjects. Pearson's correlation coefficient between *SANDI metrics quantified in GM regions is indicated (with FDR-adjusted p-values shown). Each marker represents, for a different subject, the median across regions of the specific parameter. Error bars are standard errors (median absolute deviations/squared root of number of subjects). Markers and regression lines are shown in blue. Shaded areas represent 95% confidence intervals.*

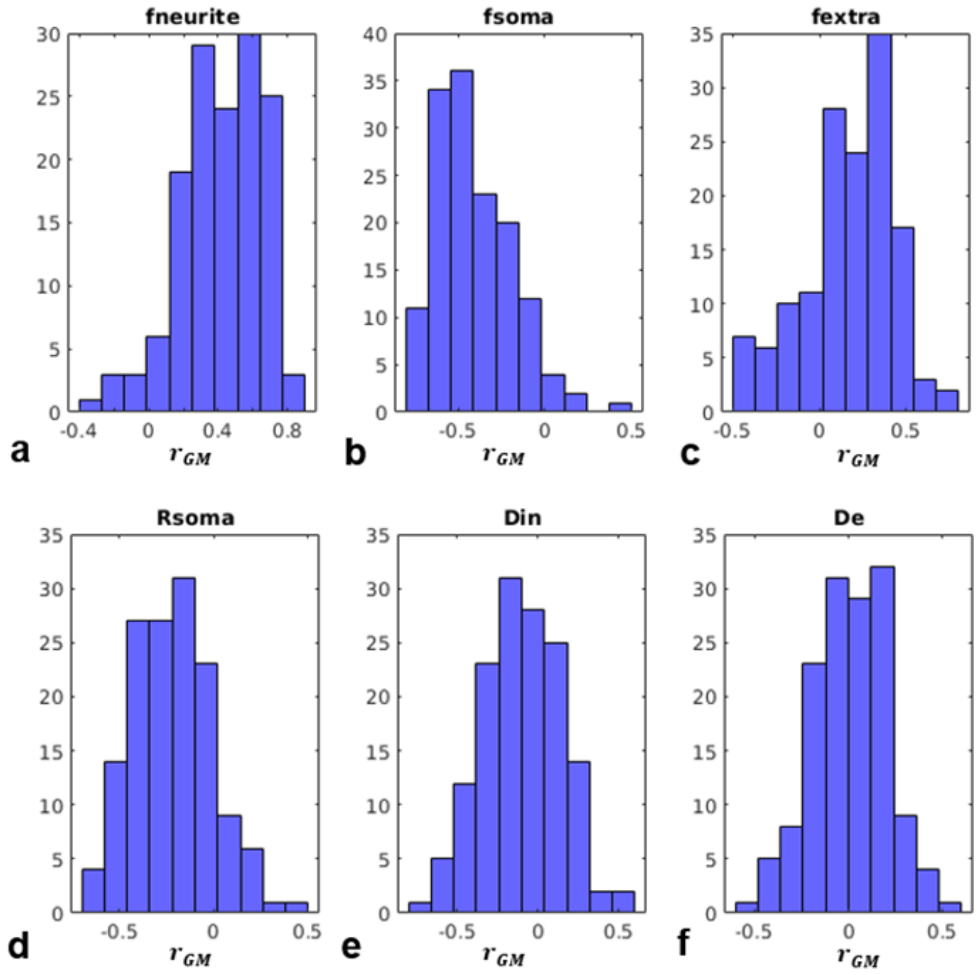


Figure 2.6. Distribution of correlation coefficients between SANDI metrics and R1 across subjects for various Grey Matter regions (ROIs). *Histograms of the Pearson's correlation coefficients between R1 and SANDI metrics across-subjects, for each grey matter ROI.*

2.4. Discussion

In this study, we tested the hypothesis that the GM microstructural characteristics, specifically its cytoarchitecture, contributed to R1 contrast, determining associations between SANDI-derived diffusion metrics in GM and R1 in healthy subjects. R1 was derived using the MP2RAGE sequence, based on a mono-compartmental model of longitudinal magnetization recovery. The findings revealed distinct associations between microstructural properties and R1 in GM and WM, providing complementary insights into cortical organization.

Diffusion data metrics and R1 mapping

Given that the diffusion protocol included b-values larger than 3000 s/mm^2, an assessment of data reliability was necessary. The evaluation of SNR confirmed that the signal remained above the noise floor, and the SNR_{diff} in the image without diffusion weighting was reasonable and comparable to a previous study evaluating SANDI metrics in healthy adults using the same clinical 3T scanner model [91].

Overall, the R1 values measured in this study aligned well with published benchmarks for healthy individuals at 3T, supporting the robustness of R1 mapping. In WM, R1 averaged 1.11 ± 0.03 s^{-1}, in agreement with previously reported ranges [93], [94] In GM, R1 averaged 0.77 ± 0.02 s^{-1}, in agreement with the values reported by Marques et al. (Marques et al., 2010) but (slightly exceeding the reported range of 0.61 - 0.75 s^{-1} [93], [94]. This deviation may reflect methodological differences, such as variations in MRI acquisition protocols, segmentation techniques, or demographic characteristics of the studied cohort.

Overall, some of the SANDI metrics were comparable with the literature, while others were not. The average extracellular signal fraction (fextra) measured in this study was 0.36 ± 0.01 in GM and 0.31 ± 0.01 in WM, which are consistent with the literature: for instance, Schiavi et al. [91] observed fextra values of 0.40 in GM and 0.30 in WM, while Krijnen et al. (Krijnen et al., 2023) reported fextra values ranging from 0.23 - 0.52 in GM and 0.15 - 0.46 in normal-appearing WM, for diffusion times Δ = 19 and Δ = 49 ms, respectively. Similarly, the average neurite signal fraction (fneurite) measured in this study was 0.19 ± 0.01 in GM and 0.41 ± 0.02 in WM. These values fall well within the range reported by [91], [95] for healthy individuals. The soma signal fraction (fsoma) measured in this study was 0.41 ± 0.01 in GM and 0.27 ± 0.01 in WM. These values are higher than those reported by [91], who observed fsoma values of approximately 0.27 in GM and 0.15 in WM, and align more closely with the findings of Krijnen et al. (Krijnen et al., 2023), who reported fsoma values of 0.55 and 0.33 in GM (averaged across cortical and deep GM) and 0.43 and 0.26 in normal-appearing WM of healthy controls, for diffusion times Δ = 19 and Δ = 49 ms, respectively. The soma radius (Rsoma) measured in this study was 13.00 ± 0.14 μm in GM and 13.08 ± 0.17 μm in WM exceeding the range reported by [91], [95]. Schiavi et al. observed Rsoma values of 12.68 μm in GM and of 10.02 μm in WM, while Krijnen et al., reported Rsoma values of 10.10 in GM and 10.23 and 10.33 in normal - appearing WM for diffusion times Δ = 19 and Δ = 49 ms, respectively. The

small difference in Rsoma between GM and WM in the present study could reflect the insensitivity of the diffusion protocol to true compartment differences, rather than a biologically meaningful similarity. This would affect particularly WM estimates, where cell body density (fsoma) is lower and the axonal components dominate the diffusion signal. Finally, the intra- and extra-neurite diffusivities (Din and De, respectively) measured in this study were respectively underestimated and overestimated by approximately 30-35% with respect to (Schiavi et al., 2023) while (Krijnen et al., 2023) did not provide explicit Din and De values, limiting a direct comparison.

When comparing the SANDI-derived diffusion metrics obtained in this study for GM and WM with values reported in literature for healthy subjects, we must consider that: first, the diffusion time employed (given by $\Delta - \delta/3$, with Δ diffusion gradient separation and δ diffusion gradient duration, which in our case is roughly 31 ms) modulates the sensitivity of the diffusion sequence to inter-compartmental water exchange; second, the values obtained from the multi-parametric fitting of diffusion data at different gradient strengths were obtained by fixing the intra-soma diffusivity (D_{is}) to a value of 3 μm²/ms, without directly constraining the upper bound in the fit; third, methodological differences in the data acquisition (e.g., the number and arrangement of b-shells) and analysis (e.g, the fitting algorithm used to extract the SANDI metrics) potentially affect the estimation of the diffusion metrics. Due to the first point, the diffusion time employed in the sequence slightly influences the estimated fraction of the three diffusive compartments. Regarding the second point, simulations and in vitro experiments have shown that the fitting remains stable across a wide range of D_{is} values, from 0.1 to 3 μm²/ms, with only minimal variations in the estimated parameters [30]. Finally, regarding the third point, the discrepancies in parameter estimates can arise first of all from the use of different b-values in the diffusion protocol. Indeed, while Schiavi et al.'s protocol employs 0/500/1000/2000/3000/4000/6000 s/mm^2, our protocol included a b-value of 200 s/mm^2, but did not include a b-value of 3000 s/mm^2. Future studies regarding the impact of adding more b-values between 200 and 1000 s/mm^2 are warranted. Another source of difference between our results and those reported in Schiavi's and Krijnen's studies lies in the fitting approach. While we used a machine learning non-linear fitting, the other two studies employed a linearized and heavily regularized version of the fitting using the AMICO framework. This difference in methodology can lead to slightly different parameter estimates.

Associations between R1 and diffusion-derived metrics

The associations between R1 and SANDI metrics could be confounded by some macroscopic tissue differences, such as cortical thickness, or the volume of the region. Although the use of median values in the ROI is less sensitive to outliers and therefore more robust to 'noise', it is important to take into account the potential confounding factors in the correlation analysis. In GM, across ROIs, a significant negative correlation was observed between R1 and soma-related metrics, with lower R1 values corresponding to higher fsoma and larger soma radii (Rsoma), as depicted in Figure 2.3. These results were significant even when controlling for GM ROI volume, cortical thickness and curvature (Table 2.2). However, the absence of a measurement of water content confounds the interpretation of the results, therefore the correlations between SANDI metrics and R1 need to be interpreted with care.

We can only speculate that these findings suggest that less myelinated regions tend to harbor larger neuronal somas, and that this may reflect differences in network functionality across cortical areas [96]. A potential link to learning remains thus only a hypothesis that requires further investigation. In this hypothetical view, such a relationship may represent a functional adaptation, where cortical areas with lower myelination maintain larger somas to support higher metabolic demands and synaptic plasticity. Such structural variations across the cortex could contribute to differential processing and learning capacities in different brain regions, underscoring the potential role of GM myelination in facilitating neuroplasticity, as regions with varying myelination levels may exhibit different capacities for adaptation and learning. The association between larger neuron sizes and lower myelination (assuming that the measured R1 depends on myelin content, among other factors) may suggest that specific cortical regions are structurally optimized for distinct functional roles, potentially influencing how information is processed within the brain. In this way, the variability in GM myelination across the human cortex could be pivotal in supporting complex cognitive functions [97], [98]. These explanations remain, however, speculative. Another possible reason why more densely myelinated regions would present smaller soma density and soma size could be linked to regional differences in cell type composition that may also influence soma size estimates. Indeed, the smaller size of oligodendrocyte cell bodies densely packed in the voxel would decrease the 'apparent' Rsoma measured with MRI, which represents a volume weighted mean of the cell sizes within a given voxel.

Moreover, considering the median across ROIs and the correlation across subjects, a positive correlation was observed between fneurite and R1 (r=0.67, FDR-adjusted p=0.0056), while fsoma and R1 exhibited a negative correlation (r=-0.56, FDR-adjusted p=0.024). These results indicate that individuals with higher global R1 in GM also exhibit a higher intensity fraction of neurites, and a lower intensity fractions of somas, which is in line with the fact that R1 depends, among other factors, on the myelin content (and the intensity fraction of neurites is proportional to the density of myelinated fibers), and suggests that myelination patterns in the cortex are influenced by different neuron intrinsic factors, other than the size, such as neuronal identity, as shown in literature [97]. Additionally, a negative trend was noted between Rsoma and R1 (r=-0.48, FDR-adjusted p=0.056), which was marginally significant (Figure 2.5).

Finally, in the WM, a strong positive correlation was found between R1 and the intensity fraction and the diffusivity of the intra-neurite compartment (namely, fneurite and D_{in}). After controlling for the confounding effect of ROI volume, only the association between D_{in} and R1 remained significant (Table 2.2). These results reinforce the notion that the intra-neurite diffusivity serves as a reliable proxy for myelin content in WM. The observed associations highlight how diffusion-weighted imaging has the potential to capture changes in microstructural integrity related to myelination, which is crucial for understanding both neurodevelopmental processes and age-related changes in brain structure [74], [99]. The strong positive correlations found in WM suggest that as myelin content increases, so do the intra-neurite characteristics reflected by D_{in}. This relationship is critical for elucidating how WM integrity supports efficient neural communication across different brain regions.

Limitations and implications for Future Research

One of the primary limitations of this study stems from the physical and technical constraints of the 3 T scanner used, which has a maximum gradient strength of 80 mT/m. Achieving a maximum b-value of 6000 s/mm^2 required a gradient pulse duration (δ) of 28 ms and a time between pulses (Δ) of 40 ms, resulting in an effective diffusion time ($\Delta - \delta/3$) of approximately 31 ms. This diffusion time is around 50% longer than the 20 ms recommended in previous studies [30], [77], [78], where a non-exchanging multi-compartment model can be used with minimal bias due to unaccounted exchange mechanisms. The use of longer gradient pulses (28 ms) and diffusion times (31 ms) in this study could result in unaccounted exchange between neurites and the extracellular compartment (occurring in the order of 20-50 ms in vivo,

according to animal studies by [77]). Using the Neurite Exchange Imaging (NEXI) model to simulate the impact of such exchange, we estimated that the unaccounted exchange between diffusion compartments in SANDI could lead to a potential underestimation of fneurite by up to 8% and D_e by up to 16%, and an overestimation of Rsoma by up to 4%. However, while these exchange effects cannot be disregarded at the diffusion time employed, their contribution to bias in parameter estimates is likely to be lower than or comparable to the noise-related bias for SNR∼100, which is the case of this study (Schiavi et al., 2023).

The diffusion acquisition protocol was originally optimized for CHARMED and included high b-values to increase sensitivity to restricted diffusion in white and grey matter, while keeping scan time as short as possible within a broader multiparametric protocol. The same acquisition was also naturally suited to SANDI modelling, enabling a more biologically specific characterization of grey-matter microstructure. In contrast, the present protocol was less well suited to NODDI, because the angular sampling at moderate b-values was limited relative to what is typically preferred for robust neurite density and orientation-dispersion estimation.

Secondly, the fitting approach to derive the diffusion-metrics via the SANDI model (linear and regularized fitting versus machine learning non-linear fitting, for instance) can lead to slightly different parameter estimates. To improve comparability and harmonization across studies, future research should adopt consistent fitting strategies. Additionally, refining noise and distortion correction algorithms in the DWI preprocessing phase and comparing different machine learning algorithms for diffusion-metrics estimation could further improve the robustness of the obtained findings.

A third limitation of the present study is represented by the premises of the MP2RAGE technique to map R1, i.e., the assumption that each voxel comprises a single spin pool of water molecules, whose signal recovery after excitation can be theoretically described by a mono-exponential behavior. This model faces limitations due to factors like the complexity of tissue composition and the influence of magnetization transfer effects [100]. Indeed, myelin has a complex structure with bound water molecules and different T1 relaxation properties than free water. Moreover, T1 relaxation in WM is not solely determined by myelin. Factors like tissue iron content [61], water-to-macromolecule ratio, i.e. effectively the water content, axonal density, and the size of axons [62] can also influence T1. Besides that, we acknowledge that mono-exponential fits of longitudinal relaxation may oversimplify the inherently multi-exponential nature of the GM, characterized by a complex cytoarchitecture with a higher density of cell bodies, dendrites and synapses [101].

As pertains to WM, other approaches exist to estimate both the short and long longitudinal relaxation components, such as inversion recovery fast-spin echo (IR-FSE) with multiple inversion times, or an MP2RAGE pulse sequence opportunely tuned, as shown in Rioux et al. [102]. In this work the authors estimated the expected bias in measuring the long T1 component as a function of the chosen TIs. This bias could not be determined in our case, as only the first TI was in the range tested by the authors. Future work will focus on exploring the biexponential relaxation in both WM and GM using clinically viable sequences such as MP2RAGE.

For the present study, which examined correlations between MP2RAGE-derived 'apparent' R1 and SANDI-derived metrics, assuming that inaccurate modeling introduced a systematic bias of the quantified R1 per tissue type [103], correlations are expected to be preserved. Future studies would ideally combine T1 mapping with complementary indices such as proton density or quantitative magnetization transfer, which better disentangle water content and macromolecular contributions.

Finally, by performing a post hoc power analysis on our data, the achieved power in detecting significant correlations between SANDI metrics and R1, given our sample size of N=20 (assuming a single tail test and a coefficient of determination R^2=0.25, considering the correlation between fsoma and R1) is 76%. Based on this analysis, our study is slightly underpowered, bringing a slightly higher risk of missing true effects (or finding significant correlations between SANDI metrics and R1).

Despite these limitations, our results highlight a significant association between cortical R1 and diffusion-derived microstructural metrics, highlighting the utility of combining R1 mapping with SANDI-based diffusion modeling and underlining the contribution of GM cytoarchitecture into R1 contrast. Future research should explore whether these relationships hold in clinical populations, particularly in conditions characterized by demyelination or altered cortical microstructure, such as Multiple Sclerosis or other neurodegenerative disorders [63], [104]. Investigating longitudinal changes in R1 and SANDI-derived metrics could provide valuable insights into disease progression and treatment response, proving useful also for advancing research in personalized medicine. Another important direction for future studies should focus on the relationship between learning-induced microstructural changes, as reflected by SANDI metrics and R1. Such research could provide further insights into the processes driving brain adaptability and resilience, shedding light on the dynamic nature of structural and functional plasticity in the human brain.

2.5. Conclusions

We found that microstructural metrics derived from the SANDI model fitting of diffusion-weighted data are significantly associated with R1 estimated via MP2RAGE. The observed correlations support the role of GM cytoarchitecture in shaping R1 contrast in GM and highlight the potential of SANDI to probe cortical microstructure related to myelination. Moreover, the findings highlighted the structural diversity of cortical GM, potentially linked to its role in supporting neuroplasticity and complex cognitive functions. The correlations found in WM validated the utility of diffusion metrics as reliable biomarkers for assessing myelin integrity in WM.

Continued methodological advance are necessary to refine diffusion-based metrics and expand their applicability in both research and clinical settings, and to make advantage of clinically viable methods optimized to be sensitive to different relaxation components. By addressing current limitations and integrating multi-parametric and multimodal imaging approaches, future studies will contribute to a deeper understanding of the structural and functional architecture of the brain in both health and disease.

3. Functional Brain Activation During Visuomotor Learning and the Role of Restricted Diffusion in Grey Matter

In this chapter we aimed to clarify the biophysical meaning of the fraction of restricted water diffusion in grey matter (GM), expressed by FR in the Composite Hindered and Restricted Model of Diffusion MRI (CHARMED) [40], [105]. To this end, we investigated the relationship between FR, R1 (1/T1), a quantitative marker sensitive to myelin-related cortical tissue properties, and the functional activation expressed by the variation in Blood-Oxygen Level Dependent (BOLD)-functional MRI (fMRI) contrast during repeated execution of a visuomotor learning task, in healthy volunteers (HV).

The results presented in this chapter were presented at the XV National Congress of the Italian Chapter of the International Society of Magnetic Resonance in Medicine (Associazione Italiana per la Risonanza Magnetica in Medicina, AIRMM) at Padova, Italy, 2024.

Abstract

Diffusion attenuated signal from the myelinated and unmyelinated axons, namely, the white matter (WM), has been largely employed to infer information on WM integrity and structure. On the other hand, the interpretation of diffusion weighted signal in the grey matter (GM) is less straightforward. In this work we focused on the fraction of restricted diffusion (FR) in GM, as estimated by the CHARMED model. In order to better understand its biophysical meaning, we investigated its relationship with cortical myelination (expressed by R1=1/T1) and the functional activation (BOLD-fMRI) in healthy volunteers (HV). Data from 20 HV (11F/9M, age = 27.5±3.8y) were analysed. MRI (3T, Siemens) included sequences to obtain BOLD-fMRI responses to a visuomotor learning task, brain quantitative R1-maps and diffusion weighted

MRI for FR quantification. FSL-FEAT was used to quantify BOLD responses. Pre-processed diffusion data were fitted to the CHARMED model using a non-linear least square estimation procedure with Levenberg-Marquardt minimization to obtain parametric FR maps. Regions of interest (ROIs) were chosen based on a GM atlas. ROIs were thresholded at 0.7 GM partial volume estimate and projected onto functional maps, where only the voxels positively responding (higher than 50^{th} percentile) to the task execution were retained. These were then used as the new subject specific ROI to extract BOLD task-response, FR and R1. A Pearson's correlation analysis was performed, with Bonferroni correction.

A positive correlation across subjects between FR and R1 was found in most of the GM ROIs suggesting a strong link between microstructural characteristics and myelination in GM. A significant negative correlation was found between FR and BOLD response to the task, only in the left supplementary motor cortex ($r = -0.79$, $p < 0.0001$), which is implicated in the control of internally generated movements. Importantly, the left supplementary motor cortex showed no significant FR-R1 association, indicating that the region-specific FR-BOLD effect is not trivially explained by R1 and may involve other microstructural or neurovascular contributors to the observed BOLD response amplitude.

3.1. Introduction

In recent years, advance in neuroimaging techniques have significantly contributed to our understanding of the intricate architecture and functional dynamics of the human brain. Among these techniques, diffusion-weighted magnetic resonance imaging (DW-MRI) has played a pivotal role in unraveling the structural complexities of brain parenchyma. This technique exploits the endogenous contrast provided by self-diffusion of water molecules in water solutions and offers the opportunity to infer non-invasively the microstructure of biological substrates probed by water protons, beyond the spatial resolution provided by MRI. Water diffusion is diversified in brain parenchyma, showing anisotropic properties in the regions with densely packed myelinated fibres (conventionally named 'white matter', WM). As illustrated in Chapter 1, the first experimental and modeling framework to describe diffusion anisotropy in WM was Diffusion Tensor Imaging (DTI), with the rotationally invariant metric fractional anisotropy (FA). DTI is based on a Gaussian model of the random displacements of water molecules in an excited volume of tissue [70], [106], [107]. This tensor represents the diffusion

properties averaged over various microdomains in a voxel, including compartments where water diffusion is slow (usually associated with the intracellular space) and fast (usually associated with the extracellular space).

In 2004, Assaf et al. [40] introduced the Composite Hindered and Restricted Model of Diffusion (CHARMED) to extend the conventional diffusion tensor imaging model (DTI) by considering both hindered and restricted diffusion within the tissue with the volume fraction of the restricted (FR) compartment reflecting highly hindered water diffusion due to cell membranes and microstructural elements. Studies showed that this parameter may serve as a valuable indicator of tissue microstructure, at least in WM, for its informativeness regarding cell density, axonal packing, and cellular organization [108]. On the other hand, the extent to which FR captures microstructural intricacies in GM and its potential implications for functional and structural aspects of the brain remain relatively unexplored. It was reported that it may reflect neuroplastic changes induced by learning/adaptation, however the literature is still sparse [109].

This study aims to delve into the role of FR in GM, addressing two key hypotheses. First, we posit that FR serves as a proxy for myelination in GM, a crucial aspect of neural architecture associated with signal transmission efficiency. Second, we hypothesize that FR correlates with functional network efficiency during demanding task execution, such as the execution of a visuomotor learning task.

To test our hypotheses, we investigated the relationship between microstructural characteristics (FR) and myelination in GM (as indicated by R1 values) and between FR and functional activation during the execution of a motor task using BOLD-fMRI.

Towards these aims, we conducted an imaging study involving twenty healthy volunteers, utilizing a 3T MRI system. Participants engaged in a motor task while their brain activity was monitored through blood-oxygen-level-dependent functional magnetic resonance imaging (BOLD-fMRI). To assess microstructural characteristics in GM, we employed the CHARMED model and obtained FR maps. Additionally, whole brain quantitative R1 (1/T1) maps were acquired to evaluate myelination levels in the GM.

The selection of the motor task was based on its relevance to understanding functional activation patterns within the brain, particularly in regions associated with motor control, execution and visuomotor learning. A glove, equipped with fibre optic sensors, allowed the

participants to control the size of a visual stimulus by performing hand movements, creating a well-defined motor task paradigm for our imaging study.

Through this study, we aim to provide insights into the relationship between FR, GM microstructure, and functional aspects of the human brain, by assessing whether FR is associated with BOLD signal changes during visuomotor learning in healthy individuals.

3.2. Methods

3.2.1. Data acquisition

Participants

This study was conducted on the same cohort described in Chapter 2 (N = 20 healthy volunteers; 9 males and 11 females; age range 24 - 31 years). Handedness was not formally recorded in this cohort. Full participant details, inclusion/exclusion criteria, and ethical approval are provided in Chapter 2.

MRI protocol

During the MRI session, participants underwent both structural and functional MRI scans. The structural acquisitions, including diffusion-weighted imaging (DWI) and quantitative R1 mapping (MP2RAGE) [110], were identical to those used in the previous investigation and are described in Chapter 2 (see Table 2.1 for sequence parameters). The functional MRI sequence parameters and task design are described below.

Functional sequences

Functional data were acquired during the visuomotor task using pseudo-continuous arterial spin labelling (pCASL) with pre-saturation and background suppression [111], combined with a dual-excitation (DEXI) readout with two different echo times [112]. This implementation was designed to obtain an arterial spin labelling (ASL) signal from the short echo time (TE1) and BOLD contrast from the longer echo time (TE2). Tag - control modulation was applied throughout the acquisition and therefore characterized both echoes. Sequence parameters were: TE1=10 ms, TE2=30 ms, labelling duration = 1.5 s, post-labelling delay (PLD) = 1.5 s, GRAPPA acceleration factor = 3, effective TR (including labelling and both readouts) = 4.9 s, 16 slices, in-plane resolution = 3.4 × 3.4 mm, slice thickness = 7 mm with a 20% slice gap. For

ASL quantification, a calibration M_0 image was additionally acquired with pCASL and background suppression switched off (TR = 6 s, TE = 10 ms).

Experimental design and visuomotor task

During the functional scans the participants performed a visuomotor learning task (Figure 3.1) using an MRI-compatible right-hand data glove (Fifth Dimension Technologies, 5DT Data Glove 16 MRI https://5dt.com/5dt-data-glove-ultra/). The glove was equipped with 14 fibre optic sensors measuring finger flexion (two sensors per finger) as well as the abduction between fingers. The device was MRI-safe and does not contain ferromagnetic components. The data glove was worn by the subjects in the scanner and connected via a set of fibre optic cables (5 m long) to the control room, where the glove was connected to the stimulus PC and the motor responses were recorded using PsychoPy [113].

Prior to the task, the glove was calibrated for each participant while positioned in the scanner. Participants were asked to alternately extend and flex their fingers (index, middle, ring, and all fingers together) to estimate each individual's maximum subjective extension and flexion. This calibration was performed in real time to establish a direct correspondence between the participant's hand movements and the visual feedback displayed on the screen.

During the task, a white circle presented on a black screen expanded and contracted according to a fixed sequence (Figure 3.1). Participants controlled the size of a green circle superimposed on the white target circle, by squeezing their hand into a fist, such that the diameter of the green circle varied as a function of finger flexion/extension.

Specifically, hand closure was mapped to circle expansion, while finger extension was mapped to circle contraction; this inverse mapping was adopted to increase task difficulty and promote visuomotor learning. Participants were instructed to continuously match the two circles as accurately as possible and were not informed that the target followed a fixed repeating sequence.

The task lasted 12 minutes and followed a block design comprising 10 task blocks interleaved with rest periods (45 s task; 30 s rest; Figure 3.1). Within each task block, the predefined target sequence was presented three times.

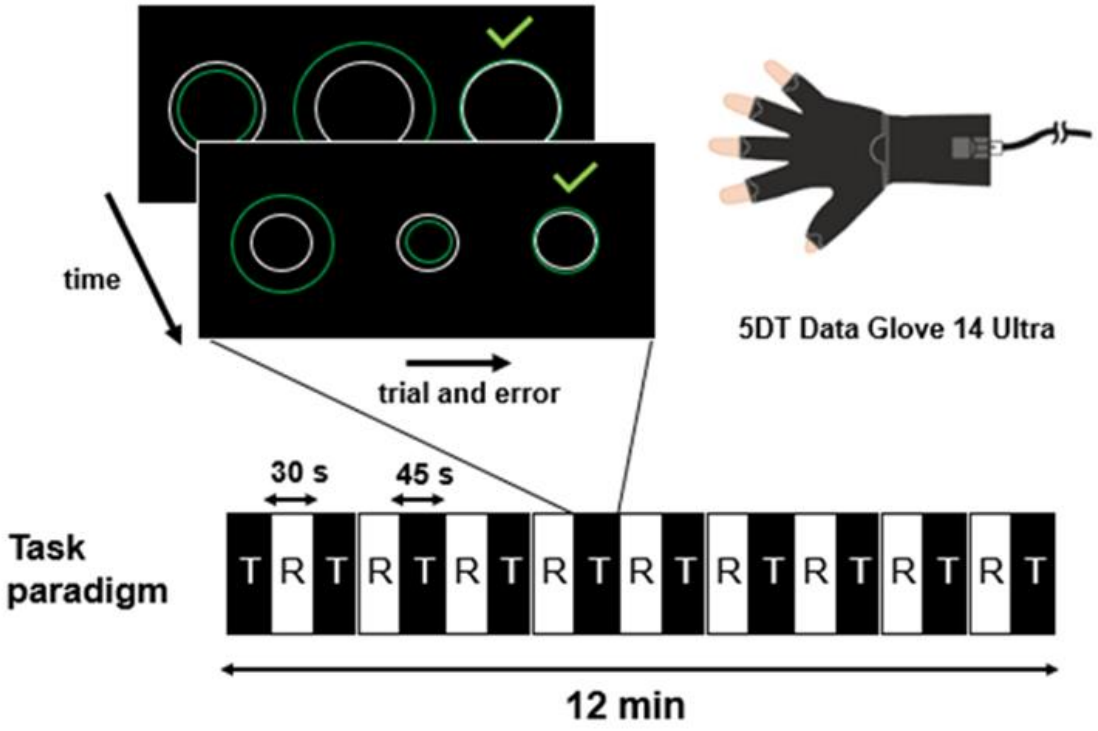


Figure 3.1. Visuomotor learning task paradigm. *The participants performed a 12 - min visuomotor task using a right - hand fibre - optic data glove (5DT Data Glove 14 Ultra). They were instructed to control the size of a green circle by squeezing their hand to match an expanding/contracting white target circle. The task consisted of 10 task blocks (T, 45 s) alternating with rest periods (R, 30 s). Within each task block, the same predefined sequence of targets was presented three times.*

3.2.2. Data processing

A combination of bash scripts, FSL tools and routines (FSL, FMRIB Software Library, v6.0.1) were used for data pre-processing, image registration and fMRI data analysis. In-house MATLAB scripts (MATLAB version: R2021a, Natick, Massachusetts: The MathWorks Inc) were used for the extraction of FR parametric maps and for the correlation analysis.

Functional MRI (fMRI) Analysis.

Functional data were analyzed using FSL FEAT. The first and second echo from the pCASL sequence's data were motion corrected using FSL tool MCFLIRT [114] and then brain extracted using Brain Extraction Tool (BET) [115]. Spatial smoothing (FWHM = 4.5 mm) of the BOLD data (surround average of TE2) was carried out with SUSAN noise reduction [116], with high-pass temporal filter applied with a cut off of 90s.

ASL data (surround subtraction of TE1) and M_0 acquisition were spatially smoothed using a 3D Gaussian kernel (FWHM = 4.5 mm). FSL tool FLIRT [117] was used to linearly register BOLD data (surround average of second echo) to individual T1- structural data (affine transformation, with 12 degrees of freedom, DOF) and then to linearly register it to MNI standard space (affine transformation, with 12 DOF). The resulting registration matrix was then used to transform CBF data (first echo) into T1 and MNI spaces using FLIRT. Functional DEXI data was registered to the structural T1-weighted image using FSL's epi-reg tool, and GM, WM and CSF partial volume estimate (PVE) output were created through FAST segmentation of the T1-weighted image. The T1-image and the GM-PVE image were transformed into DEXI space, using the inverse of this matrix. The GM-PVE image was thresholded at probability 0.7 and binarized and used as a GM mask for the parameter estimates.

FSL FEAT was used to analyse task fMRI data. BOLD and CBF changes were modelled through a gamma convolution. The BOLD task responses were modelled for the middle 12-min portion of data: task-evoked activation and deactivation were estimated with the contrasts TASK > REST and REST > TASK, respectively, to capture both increases and decreases in BOLD signal during task performance. To test for systematic changes in response magnitude across successive task blocks (adaptation or learning-related modulation), additional regressors modelling a linear dependence on block number (1-10) were included, with corresponding contrasts assessing increasing-with-block and decreasing-with-block responses (a positive task-evoked BOLD response progressively getting smaller with increasing block number). In addition, CBF was modelled within the same FEAT framework (using the tag-control modulation and a mean CBF regressor). Motion correction parameters were added as regressors.

A higher-level analysis was performed with FEAT to model the functional responses (BOLD) to the task across all participants using a mixed effects model (FLAME 1).

Z statistic images were thresholded at $Z > 2.3$ with a statistical cluster threshold of $p < 0.05$ was set.

CHARMED Analysis

DW images were pre-processed with customized MATLAB scripts (MATLAB R2021) calling for FSL pre-processing routines to suppress thermal noise, correct for distortions caused by magnetic field inhomogeneities/eddy current and signal drift. The «Multishell DTI analysis pipeline» developed at CUBRIC (Cardiff University Brain Imaging Center) was employed,

in a modular fashion (to analyze all the participants with uniform individual steps). The pipeline is included in the GitHub archive at gitlab.cubric.cf.ac.uk/scm6gp/ModularPipe. A section of the pipeline was carefully edited to allow the correct preprocessing of the DWI images (in particular, to ensure FSL TOPUP would correct the diffusion artifacts based on the actual phase-encoding direction of the B_0 and the B_0 in reverse phase-encoding, including the actual readout time, as suggested by the FSL guide. The distortion correction (DISCO) for gradient non-linearity was not applied, as not recommended by the developers of the Modular pipeline for data acquired at Siemens Prisma 3T. DWI data was denoised using the Marchenko-Pastur distribution, Principal Component Analysis (MPPCA).[82] Motion distortion correction included TOPUP to correct for susceptibility induced distortions and EDDY to correct for eddy-current distortions via FSL. A drift correction using a second order polynomial was also applied (as indicated for diffusion volumes interspersed with b0). FSL DTIFIT was employed to extract the diffusion tensor components from DWI data using a linear model and employing b-values up to 1200 s/mm^2, yielding mean diffusivity and fractional anisotropy (FA) maps, and the tensor eigenvalues and eigenvectors. FA maps were later used for parcellation of grey matter (GM). The CHARMED model (as illustrated in the theory section (Chapter 1, Eq. 1.18)) was then fitted to pre-processed data using a non-linear least square estimation procedure with Levenberg-Marquardt minimization. The FR maps obtained were transformed to MNI standard space by applying the composite affine + warp obtained co-registering the b0 to the anatomical T1 image and the structural image to the MNI standard space (in-house script written in bash calling for FSL functions).

A critical aspect to consider when analyzing DWI data is the reliability of the acquired signal. [85]. To ensure robust data quality, the signal-to-noise ratio (SNR) of the DW images was evaluated, as illustrated in Caporale et al. [72]. SNR was calculated as the ratio between the diffusion signal in WM and GM and the standard deviation of the noise in the background, providing an overall measure of signal reliability across the dataset. Please see the methods described in Chapter 2 for further details.

R1 parametric maps

MATLAB was used to derive apparent R1 maps (apparent due to the single-compartment assumption; thereafter referred to as R1) from the quantitative T1 maps produced by the MP2RAGE sequence [110], following the procedure described in Chapter 2. R1 maps were then used in the correlation analyses described below.

ROI selection and statistical analysis

The outputs of FSL FAST segmentation of the T1-weighted image were used to generate a mask of GM partial volume estimate (PVE) map. GM masks were obtained by thresholding the GM-PVE at 0.7 (Figure 3.2). Anatomical regions showing significant task-evoked BOLD responses (positive or negative) were identified at the group level using the FSL tool *atlasquery*. For the region-wise analysis, 14 regions of interest (ROIs) were selected based on the Harvard - Oxford Atlas (Figure 3.3). However, the selected ROIs did not include all regions showing any degree of activation. Considering the volume of each Harvard Oxford atlas ROI, expressed in number of voxels, were retained only those GM ROIs for which at least 50% of voxels showed a z-score higher than 2.3 in the group-level BOLD activation map (where a positive BOLD response indicated that the activity during TASK was larger than during REST, averaged over the task blocks).

To obtain subject-specific ROIs (Figure 3.4) for parameter extraction, each selected atlas ROI was first constrained to grey matter by intersecting it with the subject's GM mask derived from FAST and thresholded at PVE = 0.4 or PVE = 0.7. Unless otherwise stated, the main results are reported for PVE = 0.7, as the stricter GM masking provided cleaner ROI estimates. The resulting GM-constrained ROIs were then projected into functional space.

For each selected ROI, the regional median values of FR, R1, and $\Delta S/S$ were extracted across all voxels within the ROI, where $\Delta S/S$ denotes the change in the BOLD signal relative to its temporal mean. Pearson's correlation analysis was then performed across subjects between FR and $\Delta S/S$, and separately between FR and R1, for each ROI and hemisphere. Correction for multiple comparisons across ROIs was applied using Bonferroni correction.



Figure 3.2. Grey matter (GM) partial volume estimate (PVE) masks derived from FAST segmentation. *(A) GM mask without thresholding. (B) GM mask thresholded at PVE = 0.4. (C) GM mask thresholded at PVE = 0.7. Thresholds are shown for comparison.*

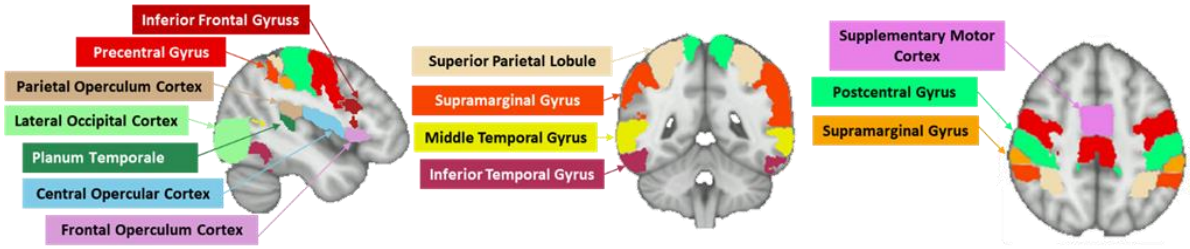


Figure 3.3. Harvard - Oxford atlas. *Representative sagittal, coronal, and axial views showing the 14 grey-matter ROIs selected based on the fMRI response; colors denote different ROIs and labels indicate the corresponding anatomical regions.*

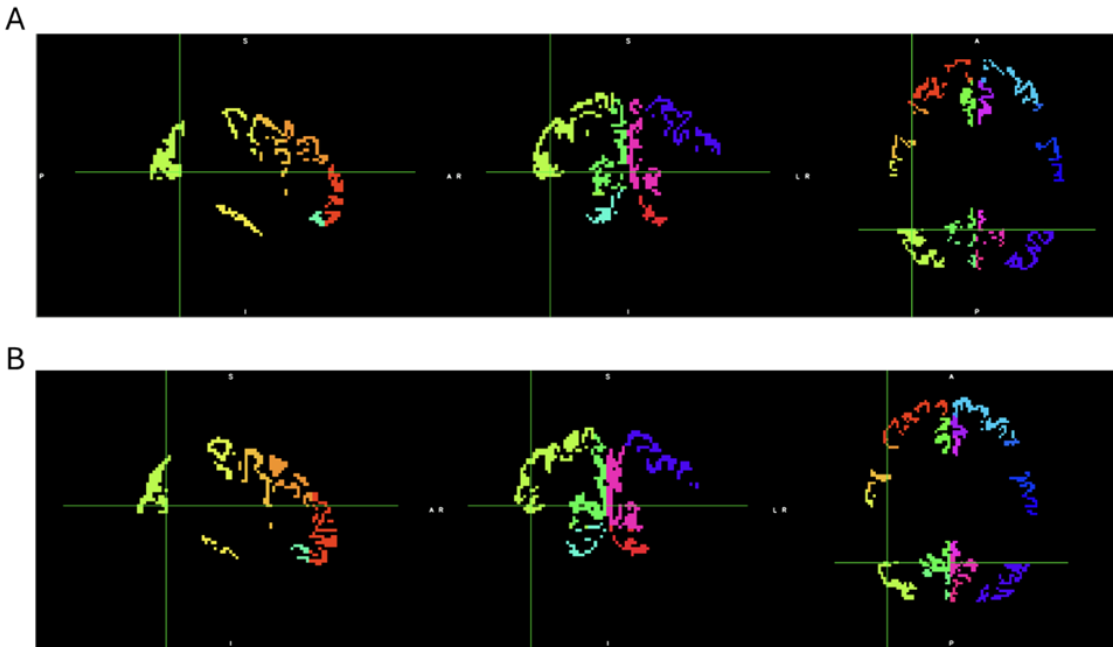


Figure 3.4. Subject-specific ROIs. *Example slices illustrating Harvard - Oxford atlas ROIs after projection into subject functional space and intersection with the subject's GM mask thresholded at PVE = 0.7: (A) participant pil002; (B) participant pil022. Colors denote different ROIs.*

3.3. Results

Reliability of DWIs and FR maps

Data quality was assessed by evaluating the signal-to-noise ratio (SNR) of diffusion-weighted images as described in Chapter 2. Since the present study used the same dataset, acquisition protocol and preprocessing pipeline, the SNR results are reported in Chapter 2 (see Figure 2.1). Briefly, SNR values in both corpus callosum and grey matter remained above the commonly accepted lower limit for reliable diffusion measurements, including the diffusion direction associated with the strongest attenuation in the corpus callosum.

Figure 3.5 shows representative restricted fraction (FR) maps for two subjects (one male and one female), displayed with a fixed color bar range of 0 - 1 to facilitate visual comparison.

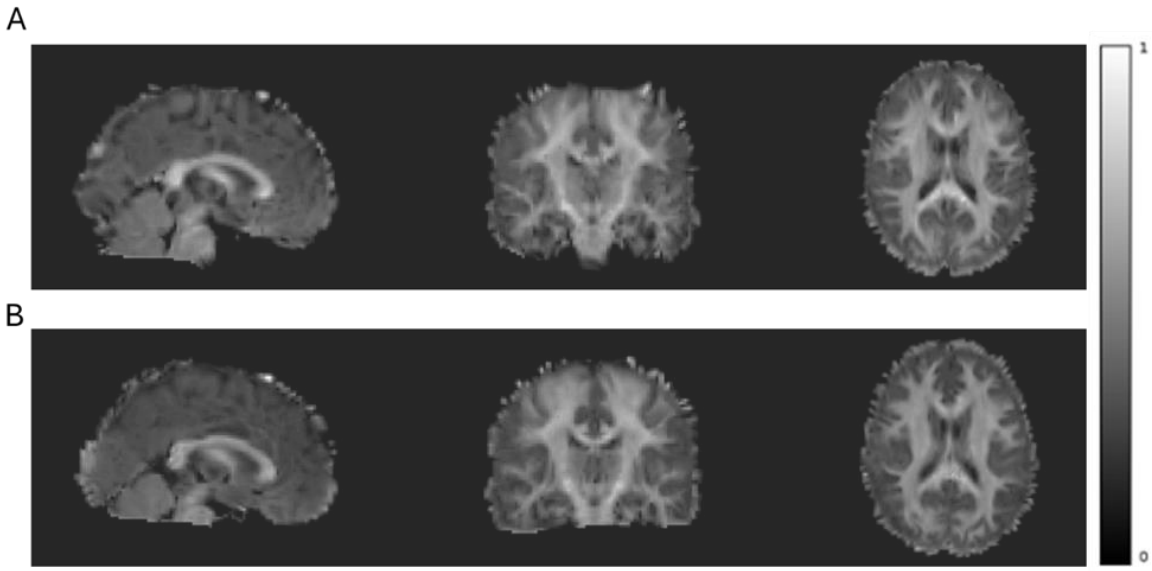


Figure 3.5. Representative restricted fraction (FR) maps. *FR maps for two representative participants: (A) male (pil002) and (B) female (pil022). Maps are shown in MNI space and displayed using a greyscale range of 0-1.*

BOLD activation during visuomotor task

Main BOLD task responses were observed predominantly in sensorimotor and parietal regions. Specifically, significant task-related responses were identified in the Precentral Gyrus, Postcentral Gyrus, Superior Parietal Lobule, and Supramarginal Gyrus (anterior and posterior divisions). Additional task-related responses were detected in opercular and supplementary motor regions (Supplementary Motor Cortex, Frontal Operculum Cortex, Central Operculum Cortex, and Parietal Operculum Cortex), as well as in temporal and occipital ROIs (Planum Temporale, Middle Temporal Gyrus, Inferior Temporal Gyrus, and Lateral Occipital Cortex). The Inferior Frontal Gyrus also showed a significant task-related BOLD response. The group-level TASK > REST activation map is shown in Figure 3.6, and its overlap with the selected Harvard-Oxford ROIs is shown in Figure 3.7.

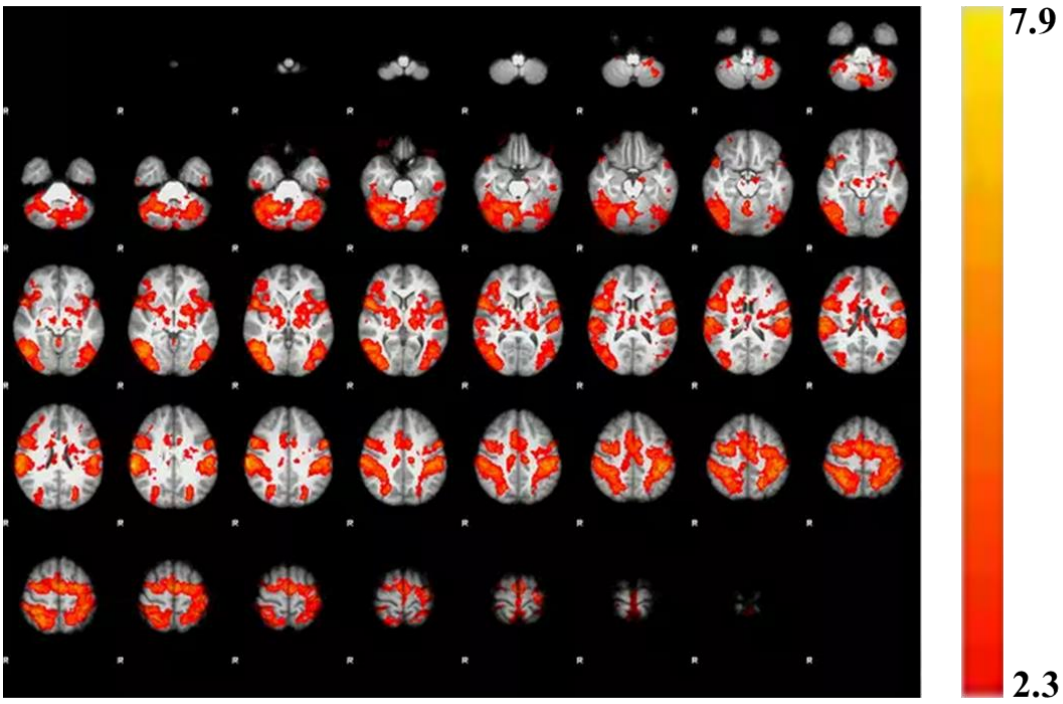


Figure 3.6. BOLD activation during the visuomotor task. *Group-level BOLD Task > Rest activation map, displayed on axial slices. Maps are thresholded at Z > 2.3 with cluster-corrected p < 0.05.*

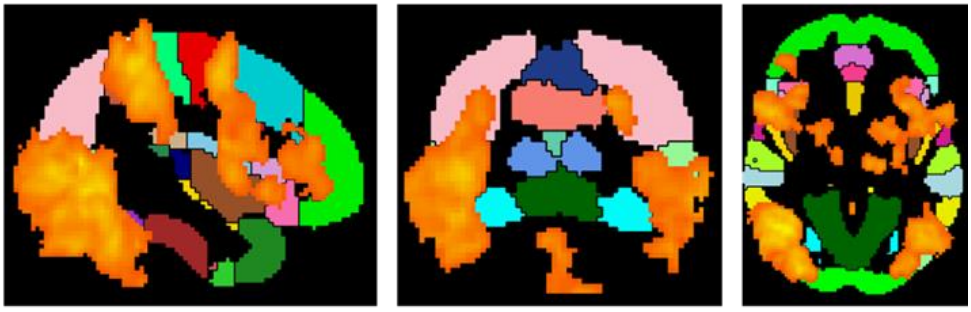


Figure 3.7. BOLD activation map overlaid on selected ROIs. *Group-level BOLD Task > Rest activation map overlaid on the selected Harvard - Oxford grey-matter ROIs (representative sagittal, coronal, and axial views). Maps are thresholded at Z > 2.3 with cluster-corrected p < 0.05.*

FR vs BOLD signal change during visuomotor task

Trend analyses using increasing-with-block and decreasing-with-block contrasts did not show significant group-level effects at $Z > 2.3$ (cluster-corrected $p < 0.05$); consequently, the reported FR-BOLD correlations refer to the median task-evoked response averaged across blocks.

BOLD task responses were quantified as fractional signal change ($\Delta S/S$), where S is the BOLD signal intensity and $\Delta S/S$ denotes the change in the BOLD signal relative to its temporal mean (reported as a unitless ratio).

For the region-wise analysis, correlations were assessed separately for the left and right hemispheres. Results are summarized in the Table 3.1. For each participant and ROI, a single data point represents the regional median FR and the regional median BOLD signal change ($\Delta S/S$), extracted from the subject-specific ROI. ROI inclusion was restricted to GM regions in which at least 50% of voxels showed a Z-statistic > 2.3 in the group-level BOLD activation map. Pearson's correlation between FR and $\Delta S/S$ was then performed across subjects, with Bonferroni correction for multiple comparisons.

Across ROIs, a significant negative correlation was observed between FR and BOLD response to the task in the left supplementary motor cortex (juxtapositional lobule cortex) with $r = -0.79$, $p < 0.0001$ (Figure 3.8). Other ROI-wise effects were weaker and did not survive correction for multiple comparisons across ROIs.

In the right hemisphere, negative FR-BOLD correlations were observed in the supramarginal gyrus (particularly the posterior division; $r = -0.61$, $p = 0.01$, with additional trend-level effects in frontal ROIs (e.g., inferior frontal gyrus and frontal operculum cortex). However, these associations were weaker than the left Supplementary Motor Cortex effect and did not survive correction for multiple comparisons across ROIs.

Table 3.1. Results. Correlation between microstructure (FR) and task response (BOLD) across GM ROIs. *A significant negative correlation was found between FR and BOLD response to the task only in the left supplementary motor cortex.*

GM ROIs	Left hemisphere		Right hemisphere	
	Correlation BOLD-FR		Correlation BOLD-FR	
	R	p value	R	p value
Inferior Frontal Gyrus	-0,40	0,10	-0,48	0,04
Precentral Gyrus	-0,33	0,18	-0,06	0,83
Middle Temporal Gyrus	-0,26	0,30	0,18	0,49
Inferior Temporal Gyrus	-0,36	0,14	-0,27	0,28
Postcentral Gyrus	0,30	0,23	0,04	0,87
Superior Parietal Lobule	-0,24	0,33	0,01	0,97
Supramarginal Gyrus AntDiv	-0,04	0,87	-0,44	0,07
Supramarginal Gyrus PosDiv	-0,37	0,13	-0,61	0,01
Lateral Occipital Cortex	-0,29	0,25	0,19	0,45
Supplementary Motor Cortex	**-0,79**	**0,000087**	0,15	0,55
Frontal Operculum Cortex	-0,19	0,44	-0,58	0,01
Central Opercular Cortex	-0,39	0,11	-0,26	0,29
Parietal Operculum Cortex	-0,01	0,97	-0,21	0,4
Planum Temporale	-0,24	0,34	-0,17	0,51

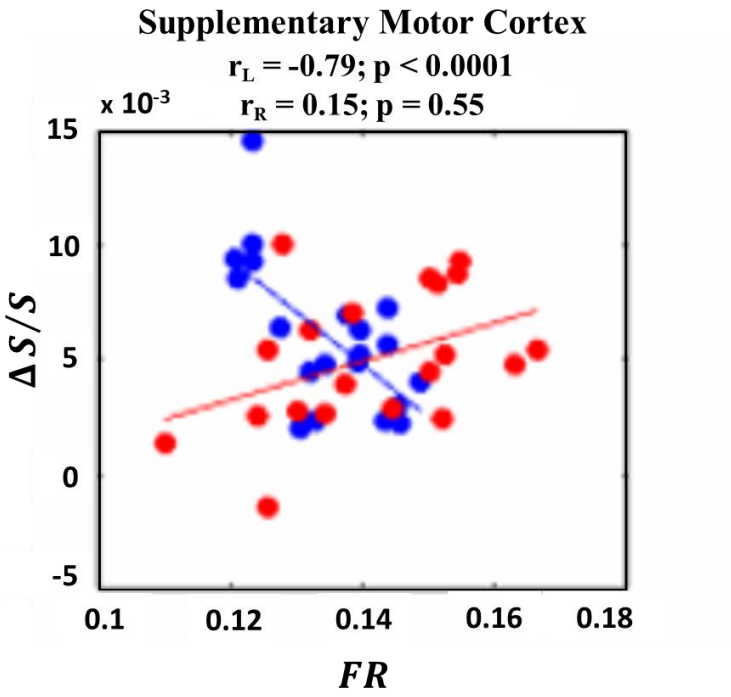


Figure 3.8. FR vs BOLD in the supplementary motor cortex. *Scatter plot shows the relationship between restricted fraction (FR) and task-evoked BOLD response across subjects. Blue and red markers indicate left and right hemisphere values, respectively. Solid lines denote linear regression fits. Pearson's correlation coefficient (r) and p-value are reported.*

FR vs R1 in the Supplementary Motor Area and other relevant regions

ROI-wise correlations between restricted fraction (FR) and R1 were assessed separately for the left and right hemispheres across the 14 GM ROIs. Overall, FR and R1 showed predominantly positive associations across cortical regions, consistent with a coupling between restricted diffusion fraction and cortical tissue properties reflected by R1 (Figure 3.9; Table 3.2).

In the left hemisphere, significant positive FR-R1 correlations were observed in the Inferior Frontal Gyrus (r = 0.72, p = 0.0008), Precentral Gyrus (r = 0.74, p = 0.0004), Middle Temporal Gyrus (r = 0.70, p = 0.0011), Supramarginal Gyrus (posterior division) (r = 0.68, p = 0.0018), Lateral Occipital Cortex (r = 0.71, p = 0.001), Frontal Operculum Cortex (r = 0.70, p = 0.0011), Superior Parietal Lobule (r = 0.75, p = 0.0004), and Parietal Operculum Cortex (r = 0.78, p = 0.0001). In contrast, no significant FR-R1 associations were detected in the Inferior Temporal Gyrus, Supramarginal Gyrus (anterior division), Supplementary Motor Cortex, Central Opercular Cortex, or Planum Temporale (Figure 3.9; Table 3.2).

Table 3.2. Results. Correlation between microstructure (FR) and R1 across GM ROIs. *A positive correlation between FR and R1 was found in most of the ROIs.*

GM ROIs	Left hemisphere		Right hemisphere	
	Correlation FR-R1		Correlation FR-R1	
	R	p value	R	p value
Inferior Frontal Gyrus	0,72	0,0008	0,66	0,0031
Precentral Gyrus	0,74	0,0004	0,65	0,0036
Middle Temporal Gyrus	0,7	0,0011	0,66	0,0026
Inferior Temporal Gyrus	0,46	0,0466	0,41	0,16
Postcentral Gyrus	0,62	0,003	0,65	0,0034
Superior Parietal Lobule	0,75	0,0004	0,91	0,0000001
Supramarginal Gyrus AntDiv	0,38	0,1	0,85	0,000001
Supramarginal Gyrus PosDiv	0,68	0,0018	0,71	0,001
Lateral Occipital Cortex	0,71	0,001	0,48	0,03
Supplementary Motor Cortex	0,42	0,08	0,74	0,0001
Frontal Operculum Cortex	0,7	0,0011	0,49	0,03
Central Opercular Cortex	0,55	0,03	0,73	0,0005
Parietal Operculum Cortex	0,78	0,0001	0,33	0,31
Planum Temporale	0,26	0,27	0,61	0,003

In the right hemisphere, significant positive correlations were detected in the Inferior Frontal Gyrus ($r = 0.66$, $p = 0.0031$), Precentral Gyrus ($r = 0.65$, $p = 0.0036$), Middle Temporal Gyrus ($r = 0.66$, $p = 0.0026$), Postcentral Gyrus ($r = 0.65$, $p = 0.0034$), Superior Parietal Lobule ($r = 0.91$, $p < 0.0001$), Supramarginal Gyrus (anterior division) ($r = 0.85$, $p < 0.0001$), Supramarginal Gyrus (posterior division) ($r = 0.71$, $p = 0.001$), Supplementary Motor Cortex ($r = 0.74$, $p = 0.0004$), Central Opercular Cortex ($r = 0.73$, $p = 0.0005$), and Planum Temporale ($r = 0.61$, $p = 0.003$). Other regions did not show significant FR-R1 associations (Figure 3.9; Table 3.2).

Notably, the left Supplementary Motor Cortex showed a strong FR-BOLD association but did not show a significant FR-R1 relationship, suggesting that the FR-BOLD effect in this region is not trivially explained by inter-individual differences in R1.

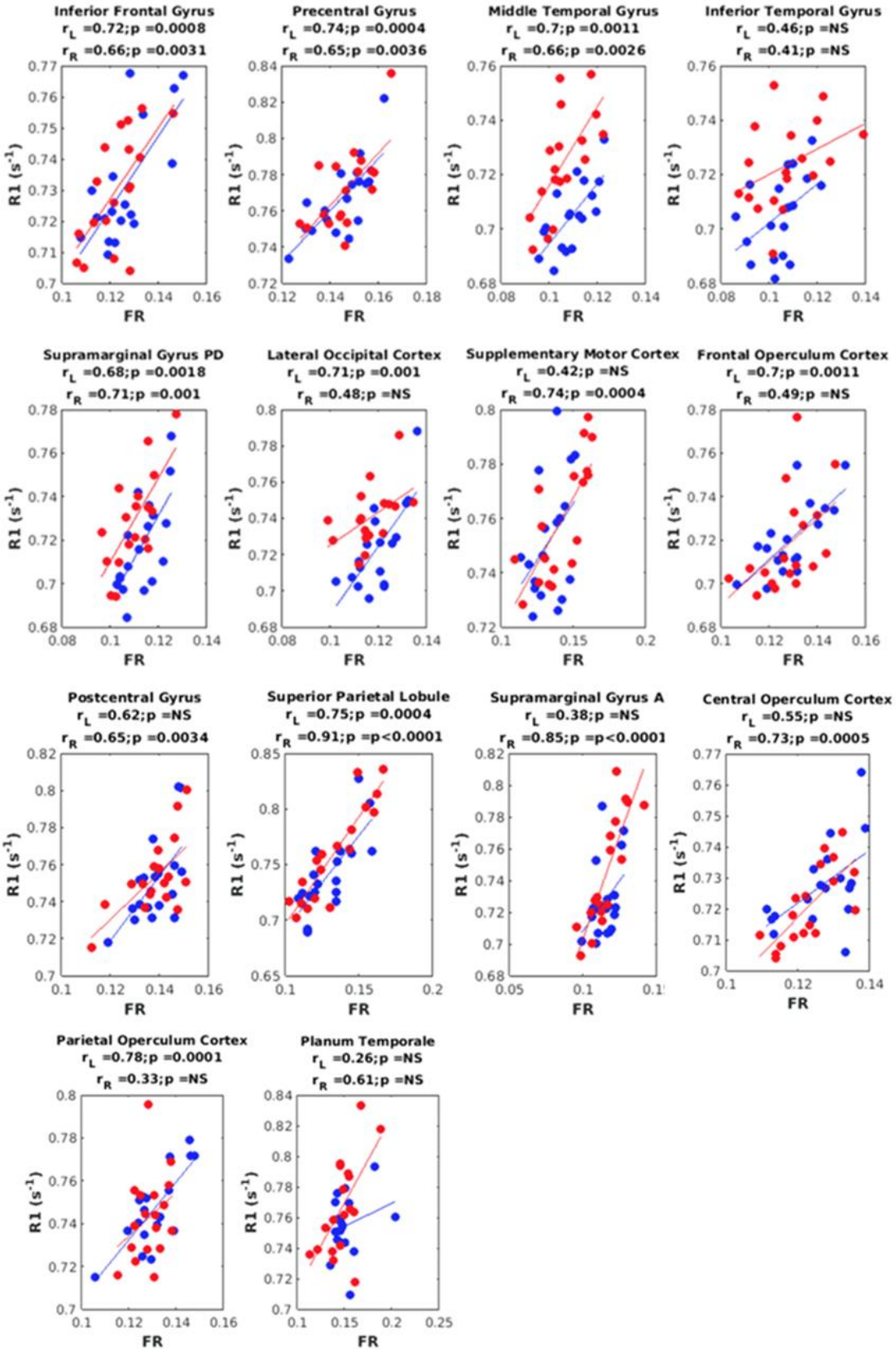


Figure 3.9. FR vs R1 in the two hemispheres. *Scatterplots are reported for each ROI separately, indicating a positive correlation or a positive trend between FR and R1. Mean values are reported in blue for the left and in red for the right hemisphere, respectively. Regression lines are depicted. Pearson's correlation r and significance p are indicated.*

3.4. Discussion

In this chapter we investigated the relationship between the fraction of restricted water diffusion in grey matter (GM), expressed by FR in the Composite Hindered And Restricted Model of Diffusion MRI (CHARMED) and cortical myelination (expressed by R1=1/T1) and the functional activation expressed by the variation in Blood-Oxygen Level Dependent (BOLD)-functional MRI (fMRI) contrast during repeated execution of a visuomotor learning task, in healthy volunteers. Two main findings emerged. First, FR showed predominantly positive associations with R1 across multiple GM regions. Second, FR did not exhibit widespread associations with task-evoked BOLD responses across the motor network; rather, a robust negative FR-BOLD association was observed specifically in the left supplementary motor cortex (juxtapositional lobule cortex), surviving correction for multiple comparisons across ROIs. This finding is anatomically plausible given that the visuomotor task was performed with the right hand, which would be expected to preferentially engage contralateral motor regions. However, handedness was not formally recorded in this cohort and should therefore be considered a limitation when interpreting the lateralization of the observed effect.

Across subjects, the region-wise FR-R1 relationship was largely positive, supporting the interpretation that FR in GM is sensitive to microstructural features that covary with cortical tissue properties captured by R1. R1 mapping is widely used as a myelin-sensitive metric, although it is not specific to myelin alone and can be influenced by other factors such as iron content and tissue water [118]. In this context, the observed FR-R1 coupling is consistent with the idea that higher restricted diffusion fraction reflects a microenvironment with greater neurite density and/or more barriers to diffusion (e.g., membranes and myelinated processes), which may co-vary with tissue properties contributing to increased R1. Importantly, FR-R1 associations were not uniform across all ROIs and differed between hemispheres, suggesting that the relationship between restricted diffusion and R1 is region-dependent in cortex and methodological factors (GM partial volume, ROI size, local susceptibility, registration accuracy) can modulate sensitivity to correlations. Taken together, these results support the use of CHARMED - derived metrics to probe GM microstructure, while also highlighting that FR does not map one-to-one onto “myelin” and likely reflects a broader set of microstructural contributors.

The group-level BOLD Task > Rest map identified the expected sensorimotor-parietal network engaged by visuomotor control (pre/postcentral, parietal, opercular and supplementary motor regions), supporting the validity of the task and the FEAT modelling choices.

However, the interpretation of BOLD amplitude during tasks repeated within a session requires caution, because the BOLD responses can vary over time due to multiple factors, including habituation, learning, fatigue, and vascular or attentional fluctuations. Within-session variability of BOLD responses has been explicitly documented, indicating that both amplitude and temporal characteristics can drift during prolonged paradigms and may not solely reflect neuronal changes [119]. This is relevant here because the visuomotor paradigm consisted of repeated blocks over ~ 12 minutes, which can elicit both learning-related and non-learning-related changes in BOLD magnitude. Moreover, during repeated motor performance and motor learning, BOLD responses may exhibit region-specific and non-linear temporal dynamics across blocks; therefore, apparent increases or decreases in activation cannot be interpreted unambiguously as “more” or “less” neural engagement, but may also reflect changes in strategy, efficiency, or neurovascular coupling [119].

The broader learning literature reports mixed patterns-both increases and decreases in BOLD activity depending on the learning stage, task structure, and regions considered. For example, learning-related activation changes have been observed in distributed networks during visuomotor transformation learning [120]. Recent work combining behavioural outcomes with imaging measures also supports the view that practice can be associated with both functional and microstructural changes, with the balance between functional activation and structural markers depending on the timescale and the aspect of performance being predicted [121]. In addition, a recent critical re-evaluation of commonly reported fMRI signatures of motor sequence learning highlights that apparent “learning effects” in BOLD can depend strongly on modelling choices and behavioural confounds, cautioning against over-interpreting simple increases/decreases in activation as direct markers of learning [122].

Overall, our findings fit within this literature in that robust task activation was present, but the relationship between microstructure and task-evoked BOLD was not globally expressed across all motor ROIs. Instead, the key association was region-specific (left supplementary motor cortex), suggesting that inter-individual microstructural differences may modulate functional recruitment in specific nodes of the motor learning network rather than across the entire activated system.

Region-specific FR-BOLD association in left supplementary motor cortex

The most striking result was the negative correlation between FR and BOLD task response in the left supplementary motor cortex, which remained significant after correction for multiple comparisons across ROIs. The supplementary motor area is strongly implicated in the preparation and control of learned movement sequences and in the internal generation/organization of actions [123]. Interpreting a negative FR-BOLD relationship requires careful consideration of what BOLD fractional signal change ($\Delta S/S$) reflects: in general, a reduced positive BOLD response (or a more negative BOLD response) may indicate reduced task-related recruitment relative to baseline, increased neural efficiency, or differences in neurovascular coupling, rather than simply "less neural activity".

Two non-mutually exclusive interpretations can be considered:

1. Individuals with higher FR in this region (potentially reflecting denser neurite microstructure) may require less metabolic/vascular upregulation to perform the same visuomotor tracking demands, resulting in smaller BOLD increases. This interpretation is consistent with findings from visuomotor learning studies where practice or neuromodulatory interventions can be associated with reduced BOLD responses while performance improves or stabilizes [124].

2. FR reflects restricted diffusion within cellular processes and can covary with the local microstructural environment. Higher microstructural density could be associated with differences in vascular density, baseline oxygenation, or flow–metabolism coupling, which would influence the observed BOLD amplitude. This is particularly relevant given that BOLD is an indirect vascular signal and not a direct readout of neuronal firing.

Crucially, the left supplementary motor cortex showed a strong FR-BOLD association but did not show a significant FR-R1 association, suggesting that the FR-BOLD effect is not trivially explained by between-subject differences in R1 (as a quantitative marker sensitive to myelin-related cortical tissue properties) in this region. This dissociation supports the interpretation that FR captures microstructural variance that may relate to functional recruitment through mechanisms not fully captured by R1 alone (e.g., neurite density, micro-geometry, extracellular space, or vascular-related factors).

Limitations and implications for Future Research

The quantitative R1 data analyzed in this chapter were acquired and processed using the same protocols and pipelines described in Chapter 2; accordingly, all methodological limitations affecting the estimation and interpretation of R1 (MP2RAGE-derived "apparent" R1) apply here unchanged. For a detailed discussion of the limited biological specificity of R1, given its sensitivity to multiple tissue constituents, the reader is referred to Chapter 2.

The diffusion acquisition protocol was tailored for CHARMED modelling and included high b-values to increase sensitivity to restricted diffusion while keeping scan time as short as possible within a broader protocol comprising structural and functional acquisitions. Among the parameters provided by the model, we focused specifically on the restricted fraction (FR), as this metric was the most directly relevant to our hypothesis and had previously been quantified in studies of short-term brain plasticity related to motor learning in the cortex. In contrast, NODDI is primarily oriented toward neurite density and orientation dispersion and typically benefits from stronger angular sampling at moderate b-values. For this reason, CHARMED was the more appropriate model for the specific question addressed in this chapter.

The interpretation of FR derived from the CHARMED model is subject to several limitations. First, FR is a model-dependent parameter whose biological meaning depends on the validity of the assumed compartment structure and signal model; this is particularly relevant in cortical GM, where microstructure is heterogeneous and partial-volume effects are prominent. Second, CHARMED fitting is sensitive to the acquisition regime (b-values, diffusion times, gradient pulse durations) and may be biased by inter-compartment water exchange and by departures from the model's simplifying assumptions (e.g., idealized restricted geometries). Third, FR estimates can be influenced by preprocessing and fitting choices (e.g., denoising, distortion correction, parameter constraints) and by residual motion and noise, which may impact parameter stability across regions.

Beyond these shared considerations, the present chapter includes a functional component that introduces additional sources of variability. BOLD-fMRI provides an indirect vascular proxy of neural activity and depends on neurovascular coupling; as a consequence, inter-individual differences in vascular responsivity and within-session fluctuations in physiology and attention can contribute to variability in BOLD amplitude independently of neuronal recruitment. This is particularly relevant for paradigms with repeated blocks over several minutes, where changes in BOLD magnitude across blocks may reflect a mixture of learning-related adaptation and

non-specific time-on-task drifts. Future studies should therefore incorporate behavioural performance metrics and explicit modelling of block-wise dynamics, and where possible use complementary hemodynamic measures (e.g., ASL-derived CBF or calibrated fMRI approaches) to help disambiguate neuronal and vascular contributions when relating microstructure to task-evoked responses.

3.5. Conclusions

This chapter investigated the relationship between GM microstructure, R1-related cortical tissue properties, and task-evoked functional activation in healthy volunteers using CHARMED-derived restricted diffusion fraction (FR), quantitative R1 mapping (R1 = 1/T1), and BOLD-fMRI during a visuomotor learning task. Region-wise and hemisphere-specific analyses led to three main conclusions:

1. FR showed predominantly positive associations with R1 across multiple GM ROIs, supporting the view that restricted diffusion fraction in GM is sensitive to tissue properties that co-vary with a myelin-sensitive quantitative MRI marker.

2. FR was not broadly associated with BOLD task responses across the entire activated motor network. Instead, a robust negative FR-BOLD association emerged specifically in the left supplementary motor cortex, suggesting that inter-individual microstructural differences in this region may modulate functional recruitment during repeated visuomotor performance.

3. The absence of a significant FR-R1 association in left supplementary motor cortex, despite the strong FR-BOLD relationship, indicates that the observed microstructure-function coupling is not trivially driven by inter-individual differences in R1 and may reflect additional microstructural or neurovascular factors.

Overall, these findings support FR as a promising diffusion-derived marker for probing GM microstructure and its functional relevance, while motivating future work to clarify the biological substrates underlying FR and its relationship with task-evoked brain activity.

4. Depth-Dependent Associations Between Grey Matter Microstructure and R1 Revealed by R1 Mapping and SANDI Modelling

This chapter tests the hypothesis that the relationship between R1, a quantitative marker sensitive to myelin-related cortical tissue properties, and diffusion-derived microstructural metrics estimated using the Soma and Neurite Density Imaging (SANDI) model is systematically dependent on cortical depth and differs across cellular compartments. We investigate whether neurite- and soma-related metrics exhibit distinct depth-dependent associations with R1 across the cortical ribbon in healthy subjects. Using surface-based depth-resolved analysis, this chapter aims to determine whether such compartment-specific associations are obscured by conventional cortex-averaged approaches. In this context, the intra-soma signal fraction (fsoma) and intra-neurite signal fraction (fneurite) are of particular interest, as they reflect distinct aspects of the underlying tissue microstructure: fsoma is associated with cytoarchitectonic features such as cell body density and organization, whereas fneurite relates to myeloarchitectural properties, in particular the distribution of aligned neurites, including axons and dendrites. In addition, we examine the apparent soma radius (Rsoma), which provides complementary information on cell body size and composition and may further modulate the relationship between microstructure and R1 across cortical depth.

Abstract

Characterizing depth-dependent cortical microstructure is essential for understanding the cellular basis of human brain organization. Here, we investigated the relationship between R1, a quantitative marker sensitive to myelin-related cortical tissue properties, and diffusion-

derived microstructural metrics estimated using the SANDI model in vivo. Data was acquired in 40 healthy adults using a standard clinical 3T MRI system and analyzed using surface-based sampling across normalized cortical depth.

Distinct depth-dependent profiles were observed for neurite- and soma-related metrics. The intra-neurite signal fraction (fneurite) decreased monotonically from deep to superficial cortical depths, closely matching the R1 profile, whereas the intra-soma signal fraction (fsoma) exhibited a non-monotonic pattern with a maximum at intermediate depths (≈0.4 - 0.6), and the estimated soma radius (Rsoma) peaked at intermediate-to-deep depths (≈0.6 - 0.8). Here, cortical depth is expressed as a normalized distance from the white matter boundary (0) to the pial surface (1).

Depth-resolved correlation analysis revealed a strong compartment-specific coupling between R1 and SANDI metrics. R1 correlated positively with fneurite, with the strongest associations in superficial depths (left hemisphere: $r \approx 0.40$ - 0.47; right hemisphere: $r \approx 0.55$ - 0.63) and progressively weaker correlations toward deeper regions. In contrast, fsoma and Rsoma showed pronounced negative correlations with R1 in superficial and mid-cortical depths (up to $r \approx -0.57$ for fsoma and $r \approx -0.68$ for Rsoma), followed by attenuation and partial inversion near the white matter boundary.

These findings show that cortex-averaged analyses fail to capture systematic depth-dependent relationships between microstructural metrics and R1 and that depth-resolved multi-parametric MRI provides a richer description of cortical organization in vivo. The observed profiles were reproducible across subjects and regions and consistent with known histological distributions. Importantly, our results demonstrate that depth-dependent mapping of cortical microstructure is feasible using clinically available MRI systems, supporting its potential for developing non-invasive biomarkers sensitive to subtle microstructural alterations in health and disease.

4.1. Introduction

Quantitative MRI has increasingly been used to probe cortical microstructure in vivo, offering indirect markers of tissue properties such as myelination, cellular composition, and neurite architecture. However, most MRI-derived measures provide voxel-averaged information, which limits their ability to resolve the pronounced microstructural heterogeneity that characterizes the cortical ribbon. In particular, conventional analyses often overlook the

laminar organization of the cortex, despite extensive evidence from histology indicating systematic layer-dependent variations in both myelin content and cellular architecture.

The cerebral cortex is organized into a layered structure. Cortical layers differ in neuronal content but also in their connectivity to other parts of the brain. The relative sizes of layers vary across the cortex in line with their functions and connectivity [125]. Cortical lamination is classically described in terms of six layers (I - VI), which can be broadly grouped into supragranular layers (I - III), the granular layer (IV), and infragranular layers (V - VI) [125], [126]. Each of these layers is characterized by distinct molecular composition, neuronal and glial cell density, soma size, dendritic organization, and patterns of intra- and inter-regional connectivity. This structural differentiation forms the anatomical basis for hierarchical information processing and functional specialization across cortical areas [6], [127].

Myelin, a key determinant of efficient neural signal transmission, is heterogeneously distributed across the cerebral cortex. Both histological investigations and quantitative MRI studies have consistently shown that deeper cortical layers, particularly layers III and V, exhibit higher myelin content, whereas superficial layers are comparatively less myelinated [128], [129].

Among quantitative MRI metrics, the longitudinal relaxation rate R1 (1/T1) has been widely adopted as a non-invasive quantitative marker sensitive to myelin-related cortical tissue contrast, owing to its sensitivity to macromolecular composition and myelin-associated lipids [130], [131].

In parallel, advances in diffusion MRI have enabled the investigation of grey matter microstructure using biophysically informed multi-compartment models. Among these, SANDI model provides separate sensitivity to soma-related and neurite-related signal components, yielding microstructural parameters such as the intra - soma signal fraction (fsoma), the estimated soma radius (Rsoma), and the intra - neurite signal fraction (fneurite) [30]. Because these parameters are linked to cellular features that vary across layers, they are expected to exhibit depth-dependent profiles within the cortex.

Previous studies have reported moderate associations between R1 and SANDI-derived microstructural parameters across grey and white matter regions, particularly involving fsoma and Rsoma, suggesting a complex interplay between myelination and cellular architecture [56]. However, these investigations have largely relied on voxel-averaged measures and have not explicitly examined how such relationships vary across the cortical ribbon.

At the time this study was initiated, no studies had systematically investigated the relationship between R1 and SANDI-derived microstructural metrics as a function of cortical depth. Given the pronounced heterogeneity of both myelin content and cellular composition across cortical layers, it therefore remains unclear whether the coupling between R1 and diffusion-derived microstructural metrics is uniform throughout the cortex or whether it exhibits layer-specific patterns. A layer-wise approach has the potential to identify specific layers where these associations are more pronounced, possibly reflecting localized functional specialization or increased vulnerability to neurological and neurodegenerative processes.

In this study, we address this gap by examining how correlations between R1 and SANDI-derived microstructural metrics vary across cortical depth in healthy volunteers. Specifically, we investigate depth-dependent associations between R1, a quantitative marker sensitive to myelin-related cortical tissue properties, and SANDI parameters reflecting grey matter microstructure, namely the intra-soma signal fraction (fsoma), the estimated soma radius (Rsoma), and the intra-neurite signal fraction (fneurite).

A layer-wise correlation analysis was performed using cortical profiles derived from FreeSurfer [132]. Quantitative measures were sampled along the cortical ribbon at normalized surface - based coordinates defined by the *projfrac* parameter (0 - 1, step = 0.1), corresponding to positions interpolated between the white matter boundary (*projfrac* = 0) and the pial surface (*projfrac* = 1).

4.2. Methods

4.2.1. Data acquisition

Participants

The study participants were 40 healthy adult volunteers (22 males and 18 females). The age range was 22 - 54 years (mean = 32.3 years; standard deviation (SD) = 6.5 years). All participants provided written informed consent prior to participation, and they were screened for MRI compatibility. None of the subjects had a history of neurological disease, psychological disorders, drug or alcohol abuse, or use of neuropsychiatric medication. Participants were instructed to maintain their usual intake of food, drink (including alcohol), and caffeine on the day of the study. The research protocols were reviewed and approved by

the Ethics Committee of the Provinces of Chieti and Pescara for research involving human participants (CRRM), “G. D’Annunzio” University.

MRI protocol

The imaging protocol was conducted on a Siemens Prisma 3T scanner (Siemens Healthineers, Erlangen, Germany) at the Institute for Advanced Biomedical Technologies (ITAB), “G. D’Annunzio” University of Chieti-Pescara, using a 32-channel, receive-only head coil. All participants underwent a protocol including diffusion-weighted imaging (DWI) with varying gradient strengths and quantitative R1 mapping via Magnetization Prepared 2 Rapid Acquisition Gradient Echo (MP2RAGE) sequence [23], with detailed sequence parameters listed in Table 4.1.

The MP2RAGE sequence models R1 assuming that water exchange between free water and water bound to macromolecules is negligible, and that each voxel comprises a single spin pool of water molecules, whose signal recovery after excitation can be theoretically described by a mono-exponential behavior. DWI included six non-zero b-shells with increasing diffusion directions at higher b-values and 14 b0 volumes acquired with phase-encoding in an anterior-posterior direction. In addition, an image with no diffusion weighting but an opposite phase-encoding direction was acquired for susceptibility distortion correction. B-value shuffling was adopted to avoid excessive gradient coil heating [81].

Table 4.1. Sequence details. *Overview of parameters for Diffusion - Weighted Imaging (DWI) and R1 protocols.*

Parameter	DWI Protocol	R1 Mapping Protocol
Total DWI Volumes	214	-
Diffusion Directions/Volumes per b-shell	14 / 10 / 30 / 40 / 40 / 40/ 40	-
Diffusion Weightings (b-values)	0 / 500 / 1000 / 2000 / 3000 / 4000 / 6000 s/mm²	-
Acquisition Method	Multi-Band accelerated EPI Pulse Sequences	MP2RAGE
Repetition Time (TR)	3000 ms	5000 ms
Echo Time (TE)	90 ms	3.58 ms
Flip Angle (FA)	50°	FA1 = 4°, FA2 = 5°
Refocusing Flip Angle	180°	-
Diffusion Gradient Separation (Δ)	44.26 ms	-
Diffusion Gradient Duration (δ)	21.78 ms	-
Resolution	1.8-mm isotropic	1-mm isotropic
Number of Slices	80	176
Field of View (FOV)	200 x 200 mm²	256 x 256 mm²
Bandwidth	2066 Hz/pixel	180 Hz/pixel
GRAPPA Acceleration	2	3
Inversion Times (TI)	-	TI1=700 ms, TI2=2500 ms
Echo Spacing	0.59 ms	8.26 ms
Slice orientation	Transversal	Sagittal
Scan duration	11.39 min	4.59 min

GRAPPA=GeneRalized Autocalibrating Partial Parallel Acquisition; EPI=Echo-Planar Imaging; MP2RAGE=Magnetization Prepared 2 Rapid Acquisition Gradient Echoes.

4.2.2. Data processing

Data processing followed the same preprocessing and analysis pipeline adopted in the first study and described in Chapter 2 of this thesis, ensuring methodological consistency across analyses. Briefly, diffusion-weighted images underwent standard denoising and artifact correction procedures, followed by corrections for susceptibility-induced distortions, eddy currents, and subject motion using established software tools, including MRtrix3 and FSL. Quantitative R1 maps and SANDI-derived microstructural metrics - namely the intra-soma signal fraction (fsoma), the estimated soma radius (Rsoma), and the intra-neurite signal fraction (fneurite) were subsequently computed using MATLAB and dedicated toolboxes.

The same quality control procedures described in the first study were applied to all datasets, including signal-to-noise ratio assessment and visual inspection of preprocessing outputs. This unified pipeline enabled direct comparison of metrics across studies while minimizing variability arising from data processing choices.

Surface-based cortical depth analysis

For each subject, 3D T1-weighted anatomical images were processed using FreeSurfer (version 7.3.2) [132] with the standard «*recon-all*» pipeline. This automated procedure included skull stripping, cortical grey matter parcellation and cortical surface reconstruction. All reconstructed surfaces were visually inspected to ensure adequate segmentation quality, and no manual edits were required. The resulting white matter and pial surfaces were used as anatomical references for subsequent surface-based cortical depth analyses.

Quantitative R1 maps and SANDI-derived parametric maps were subsequently resampled into the native FreeSurfer anatomical space to ensure accurate voxel-to-voxel correspondence with the reconstructed cortical surfaces. This step was performed using the ANTs software package (*antsApplyTransforms*), with the FreeSurfer anatomical volume (*brain.mgz*) used as the reference image. No spatial transformations were estimated or applied (i.e., no rigid, affine, or nonlinear registration was performed); instead, the procedure ensured consistent voxel geometry between the quantitative maps and the anatomical data. This operation preserved the anatomical integrity of the quantitative data while guaranteeing proper voxel-to-voxel correspondence, which is required for subsequent surface-based projection and laminar sampling along the cortical ribbon.

Volumetric R1 and SANDI parametric maps were subsequently projected onto the reconstructed cortical surface using FreeSurfer's *mri_vol2surf* tool. Projections were performed separately for the left and right hemispheres. For each subject, data were sampled at multiple normalized cortical depths defined by the *projfrac* parameter, ranging from 0 to 1 in steps of 0.1. These values correspond to fractional positions interpolated between the white matter boundary (*projfrac* = 0) and the pial surface (*projfrac* = 1), allowing the characterization of depth-dependent variations across the cortical ribbon while minimizing biases due to regional differences in cortical thickness. It should be noted that cortical depth in this context represents normalized surface-based coordinates along the cortical thickness and does not correspond directly to histologically or cytoarchitectonically defined cortical layers.

Cortical regions of interest were defined according to the Desikan - Killiany atlas implemented in FreeSurfer and provided in the surface annotation file *aparc.annot* for each hemisphere. This atlas subdivides the cerebral cortex into 34 gyral - based regions per hemisphere based on anatomical landmarks and sulcal - gyral patterns derived from the subject's reconstructed cortical surface. For each cortical region, hemisphere, and sampled cortical depth, depth-dependent profiles of R1 and SANDI-derived microstructural metrics were extracted. For each metric, summary statistics (mean, median, and standard deviation) were computed across all ROIs.

4.3. Results

No subject was excluded due to severe motion or ringing artifacts, resulting in an initial dataset of 40 healthy participants. Following surface reconstruction and parcellation with FreeSurfer, four subjects were excluded after visual inspection: three due to failed cortical labeling/parcellation, and one due to a structural anatomical abnormality (arachnoid cyst) identified on the anatomical MRI.

The final sample therefore consisted of 36. All included subjects showed adequate projection of R1 and SANDI maps onto the reconstructed cortical surfaces after processing with *mri_vol2surf*.

4.3.1. Depth-dependent profiles of R1 and SANDI metrics

Precentral gyrus is shown as a representative ROI; analogous profiles across all cortical ROIs are provided in Supplementary Figures S5 - S6.

Figure 4.1 shows representative layer-wise profiles of intra-neurite signal fraction (fneurite) and R1 across normalized cortical depth in the precentral gyrus, displayed separately for the left and right hemispheres. Mean values across subjects are shown, with error bars representing inter-subject variability.

Across hemispheres and regions, R1 exhibited a robust monotonic decrease from the white matter boundary (*projfrac* = 0) towards the pial surface (*projfrac* = 1), consistent with the expected depth-dependent decrease in R1 across the cortical ribbon.

The intra-neurite signal fraction (fneurite) demonstrated a closely matching depth - dependent pattern, with higher values in deeper cortical layers and a gradual reduction towards superficial layers. This parallel behavior resulted in highly similar profile shapes for R1 and fneurite across cortical depth.

Although the absolute values varied across regions, the overall shape of the laminar profiles was consistent across ROIs and between hemispheres, indicating a robust depth - dependent organization. The parallel decrease of fneurite and R1 across cortical depth suggests a close correspondence between neurite - related microstructural properties and myelin-related cortical tissue properties reflected by R1 across the cortical ribbon.

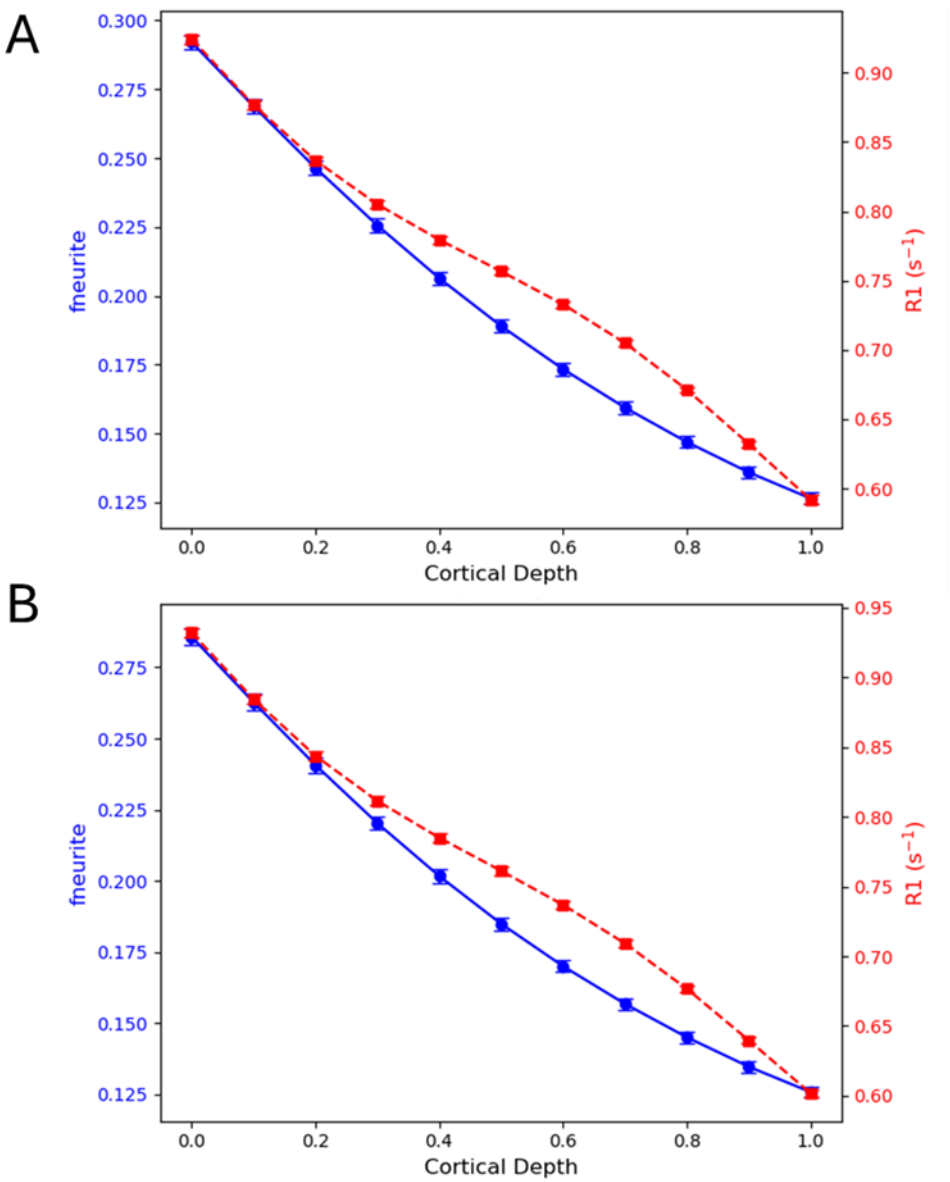


Figure 4.1. Depth - dependent profiles of intra - neurite signal fraction (fneurite, blue, left axis) and R1 (red, right axis) across cortical layers in the precentral gyrus defined by the Desikan - Killiany atlas. *Mean values ± standard deviation across subjects are shown separately for the left (A) and right (B) hemispheres. Cortical depth is expressed as normalized distance from the white matter boundary (0) to the pial surface (1).*

In contrast to the fneurite, the intra-soma signal fraction (fsoma) exhibited a markedly different laminar profile (Figure 4.2). Across regions and hemispheres, fsoma showed a pronounced non-monotonic depth dependence, characterized by lower values near both the white matter boundary and the pial surface, and a clear maximum at intermediate cortical depths (typically around *projfrac* ≈ 0.4 - 0.6).

This pattern was consistently observed across cortical regions and in both hemispheres, although the absolute magnitude of fsoma varied between ROIs (as illustrated in Supplementary Figures S7 – S8). The mid-cortical peak of fsoma indicates a preferential contribution of soma - related signal components in the central portion of the cortical ribbon, consistent with the known laminar distribution of neuronal cell bodies.

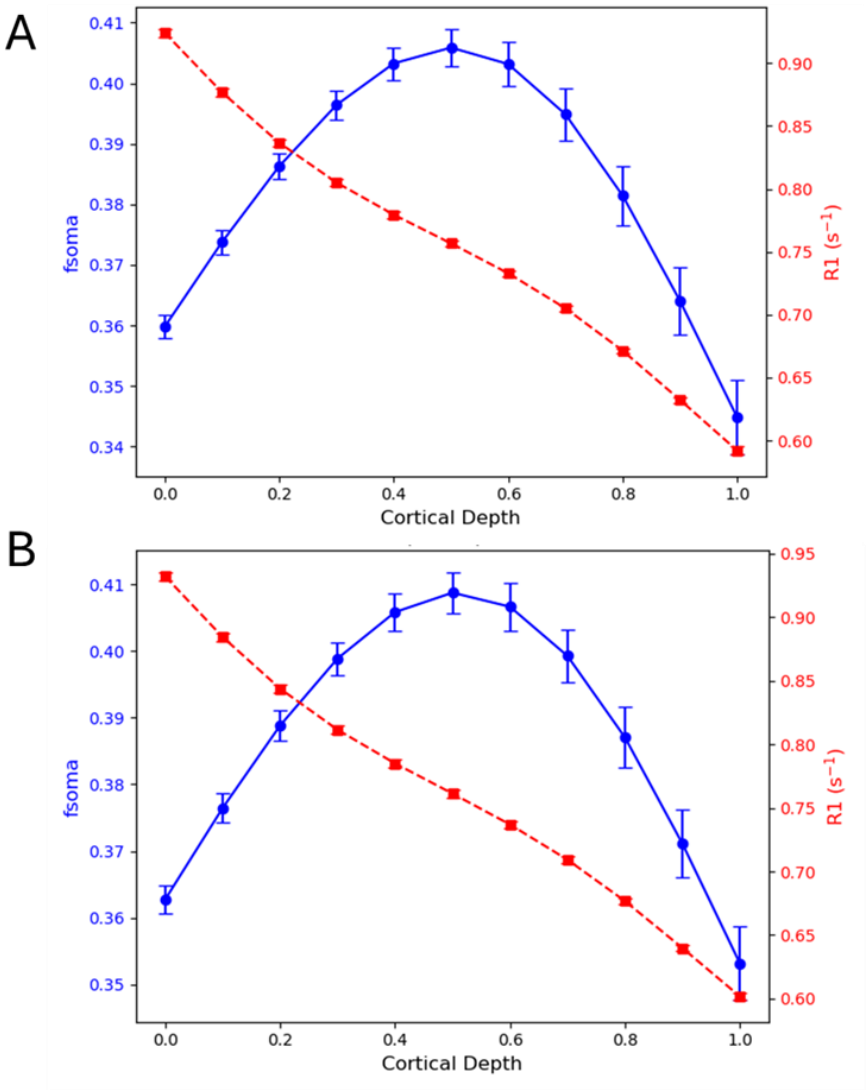


Figure 4.2. Depth - dependent profiles of intra - soma signal fraction (fsoma, blue, left axis) and R1 (red, right axis) across cortical layers in the precentral gyrus defined by the Desikan - Killiany atlas. *Mean values ± standard deviation across subjects are shown separately for the left (A) and right (B) hemispheres. Cortical depth is expressed as normalized distance from the white matter boundary (0) to the pial surface (1).*

The estimated soma radius (Rsoma) exhibited a systematic depth - dependent variation, with values increasing from superficial layers toward mid-cortical depths and reaching a maximum

typically between *projfrac* ≈ 0.6 - 0.8, followed by a moderate decrease toward the white matter boundary (Figure 4.3). Compared to fsoma, changes in Rsoma across cortical depth were less pronounced, yet highly reproducible across hemispheres and cortical regions (as illustrated in Supplementary Figures S9 – S10). Notably, the depth-dependent profiles of fsoma and Rsoma differed qualitatively from those observed for R1 and fneurite. Whereas R1 and fneurite exhibited monotonic decreases toward the cortical surface, soma-related metrics displayed maximal values in intermediate depths. This divergence highlights the distinct layer-specific organization of cellular and myelin-related microstructural components within the cortex.

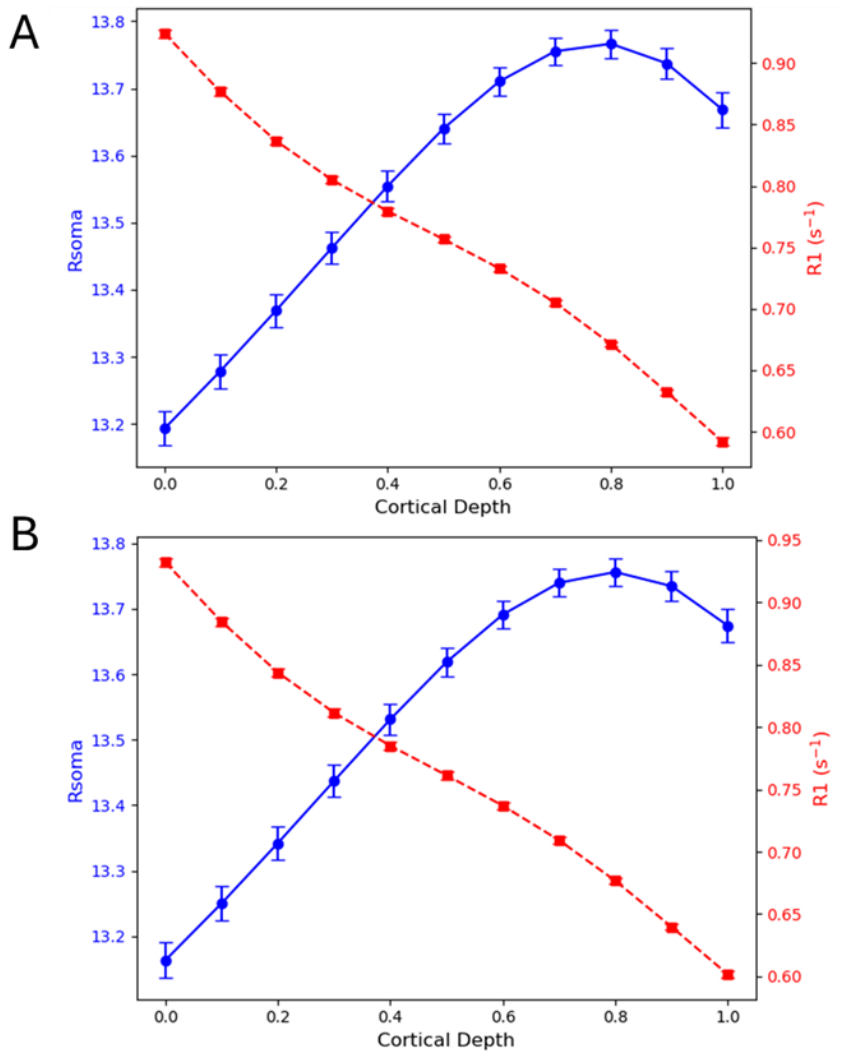


Figure 4.3. Depth - dependent profiles of estimated soma radius (Rsoma, blue, left axis) and R1 (red, right axis) across cortical layers in the precentral gyrus defined by the Desikan - Killiany atlas. *Mean values ± standard deviation across subjects are shown separately for the left (A) and right (B) hemispheres. Cortical depth is expressed as normalized distance from the white matter boundary (0) to the pial surface (1).*

4.3.2. Inter-subject variability of depth profiles

To further characterize inter-subject variability, individual subject depth profiles were examined for all estimated microstructural parameters (Figures 4.4 - 4.6). Each trajectory represents the depth-dependent profile of a single participant across the normalized cortical thickness.

For all parameters, the laminar trends observed at the group level were consistently reproduced at the individual level. In particular, parameters exhibiting monotonic decreases with cortical depth as well as those showing non-monotonic profiles with a mid-cortical maximum displaying highly similar shapes across subjects.

While noticeable variability was present in the absolute values of the parameters, the relative changes across cortical depth and the overall profile morphology remained remarkably stable. This indicates that inter-subject differences primarily affect the scaling of the profiles rather than their qualitative depth-dependent organization.

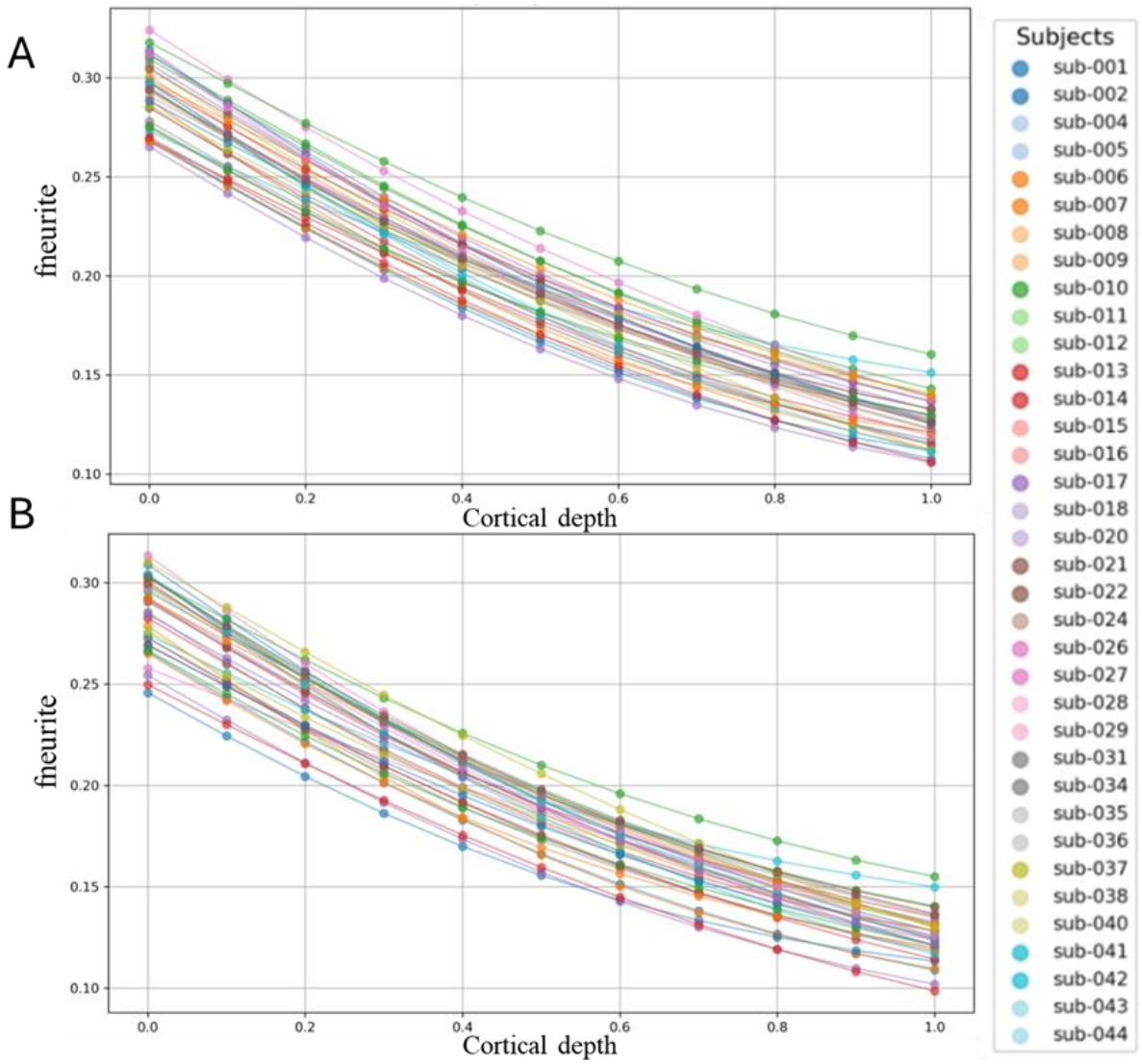


Figure 4.4. Inter - subject variability of depth - dependent profiles of intra - neurite signal fraction (fneurite). *Individual depth profiles are shown for all subjects in the precentral gyrus defined by the Desikan - Killiany atlas. Each colored line represents one participant. Profiles are displayed separately for the left (A) and right (B) hemispheres. Cortical depth is expressed as normalized distance from the white matter boundary (0) to the pial surface (1).*

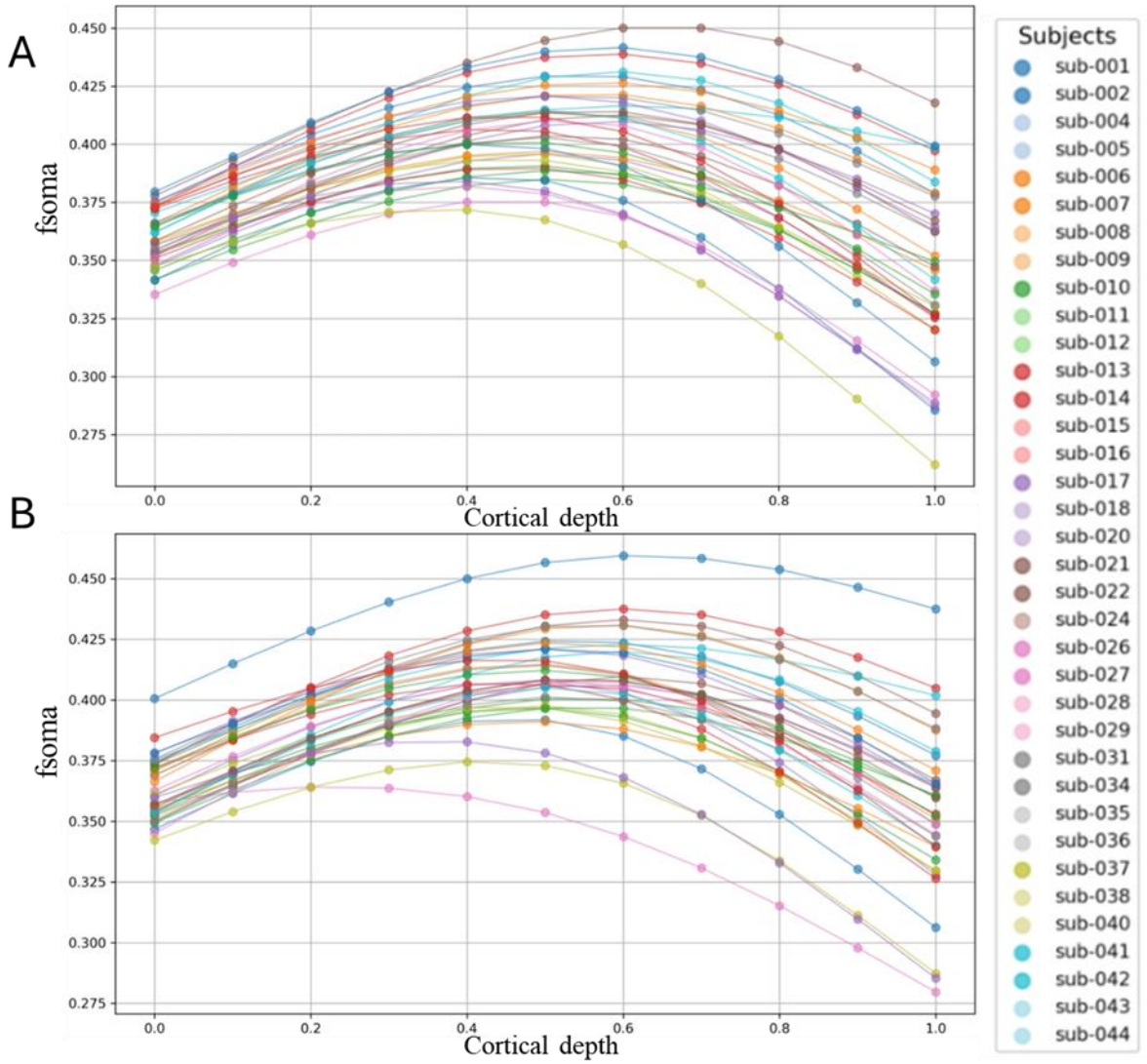


Figure 4.5. Inter - subject variability of depth - dependent profiles of intra - soma signal fraction (fsoma). *Individual depth profiles are shown for all subjects in the precentral gyrus defined by the Desikan - Killiany atlas. Each colored line represents one participant. Profiles are displayed separately for the left (A) and right (B) hemispheres. Cortical depth is expressed as normalized distance from the white matter boundary (0) to the pial surface (1).*

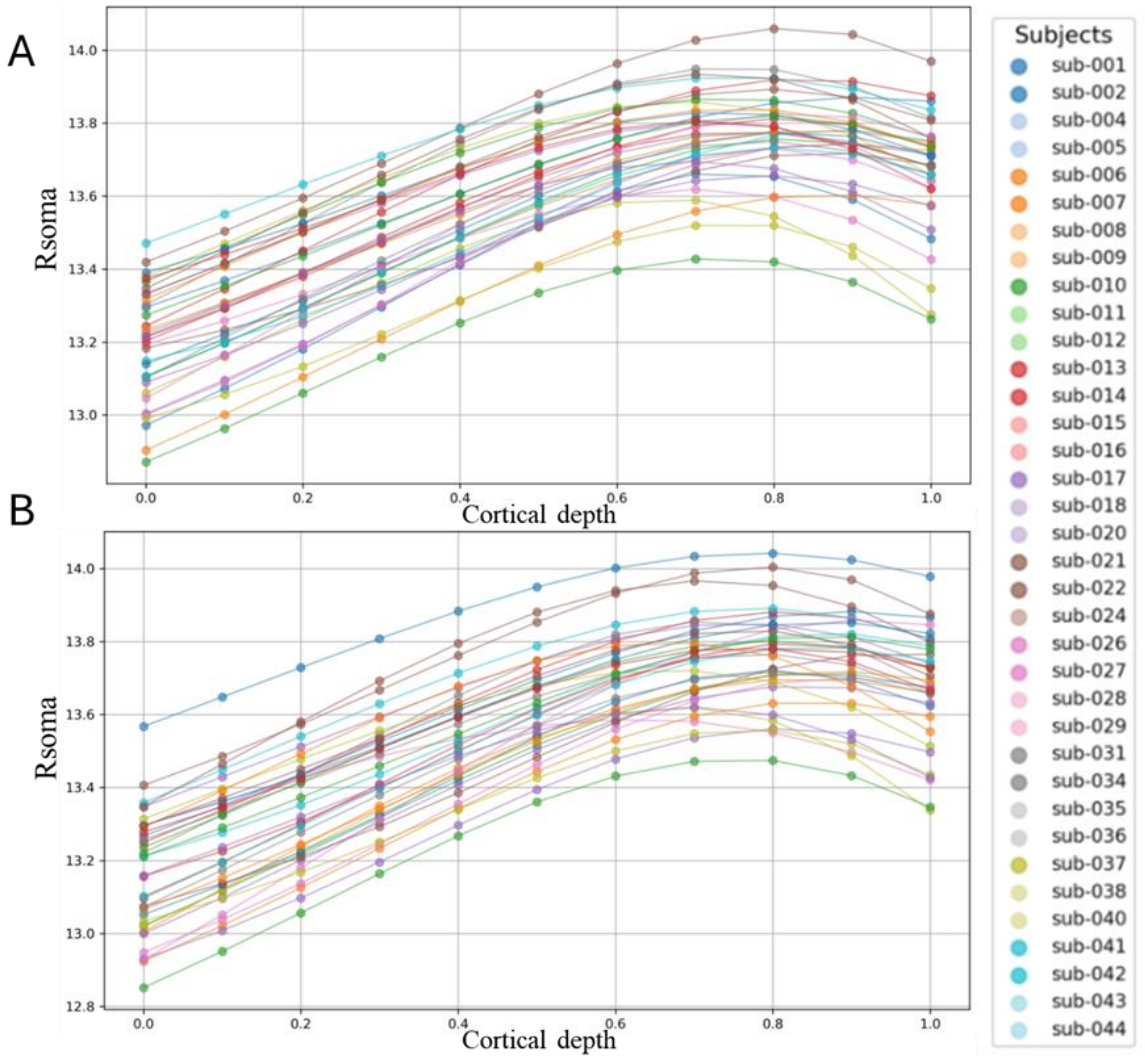


Figure 4.6. Inter - subject variability of depth - dependent profiles of estimated soma radius (Rsoma). *Individual depth profiles are shown for all subjects in the precentral gyrus defined by the Desikan - Killiany atlas. Each colored line represents one participant. Profiles are displayed separately for the left (A) and right (B) hemispheres. Cortical depth is expressed as normalized distance from the white matter boundary (0) to the pial surface (1).*

4.3.3. Depth-dependent correlations between R1 and SANDI metrics

Depth-dependent correlations between R1 and the intra - neurite signal fraction (fneurite) were evaluated across subjects at each cortical depth for all regions of interest, using regional mean values at each depth. In the following, results are illustrated in detail for the precentral gyrus as a representative example (Figures 4.7 - 4.8).

In both hemispheres, fneurite exhibited a positive correlation with R1 across all cortical depths. The strongest associations were observed in superficial layers (depth 0.0 - 0.3), where

correlation coefficients reached moderate to high values (left hemisphere: $r \approx 0.40$ - 0.47, $p < 0.05$; right hemisphere: $r \approx 0.55$ - 0.63, $p < 0.001$).

With increasing cortical depth, the strength of the correlation gradually decreased. In mid-cortical layers (depth 0.4 - 0.6), correlations remained significant but were weaker (left hemisphere: $r \approx 0.28$ - 0.33; right hemisphere: $r \approx 0.40$ - 0.46). In deeper layers (depth ≥ 0.7), the relationship further attenuated and, in some cases, did not reach statistical significance, particularly in the left hemisphere.

Overall, these results indicate a robust positive association between R1 and neurite density that is most pronounced in superficial cortical layers and progressively diminishes toward deeper cortical layers. The consistently higher correlation coefficients observed in the right hemisphere suggest a slightly stronger coupling between R1 and fneurite in this hemisphere.

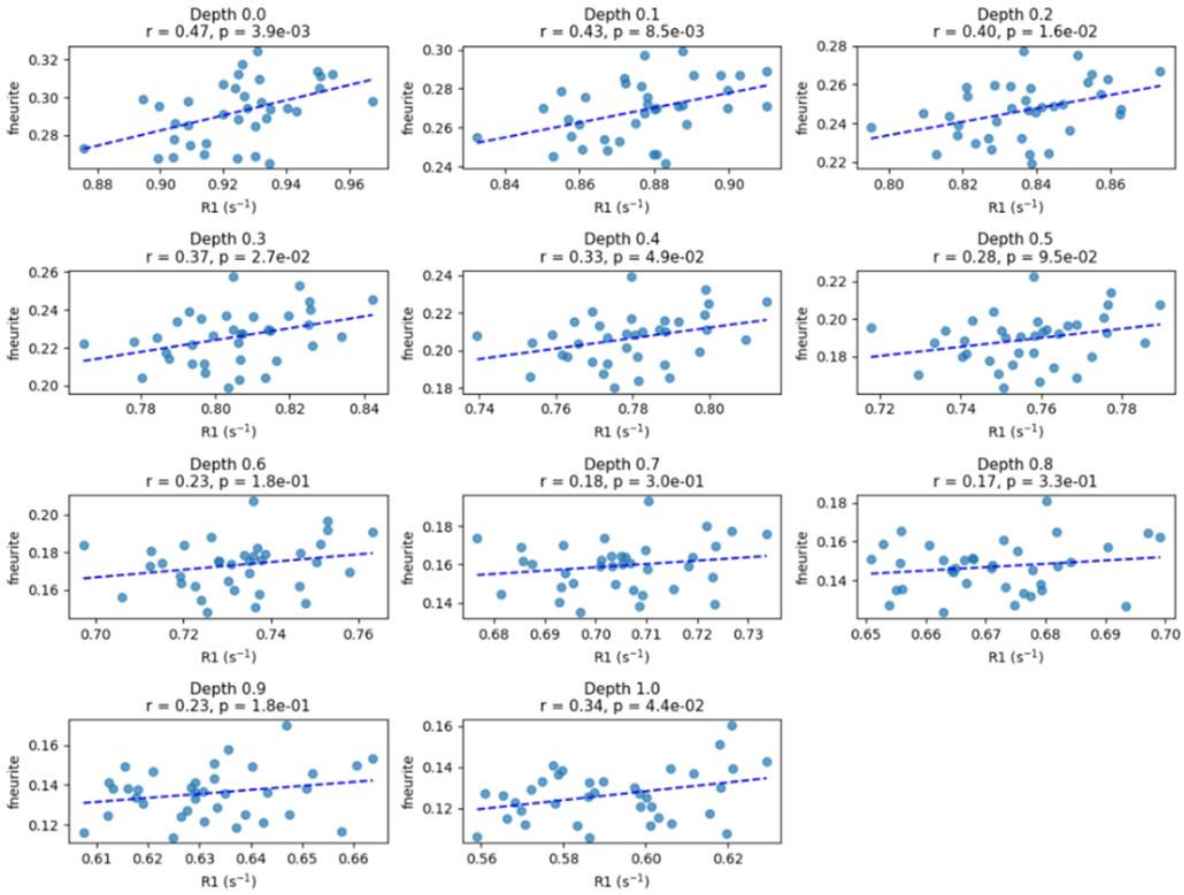


Figure 4.7. Depth-dependent correlations between R1 and intra - neurite signal fraction (fneurite) in the precentral gyrus defined by the Desikan - Killiany atlas (left hemisphere). *Scatter plots show inter-subject correlations between regional mean R1 and fneurite values computed separately at each normalized cortical depth. Each point represents one subject. Pearson correlation coefficients (r) and corresponding p-values are reported in each panel. Cortical depth is expressed as normalized distance from the white matter boundary (0) to the pial surface (1).*

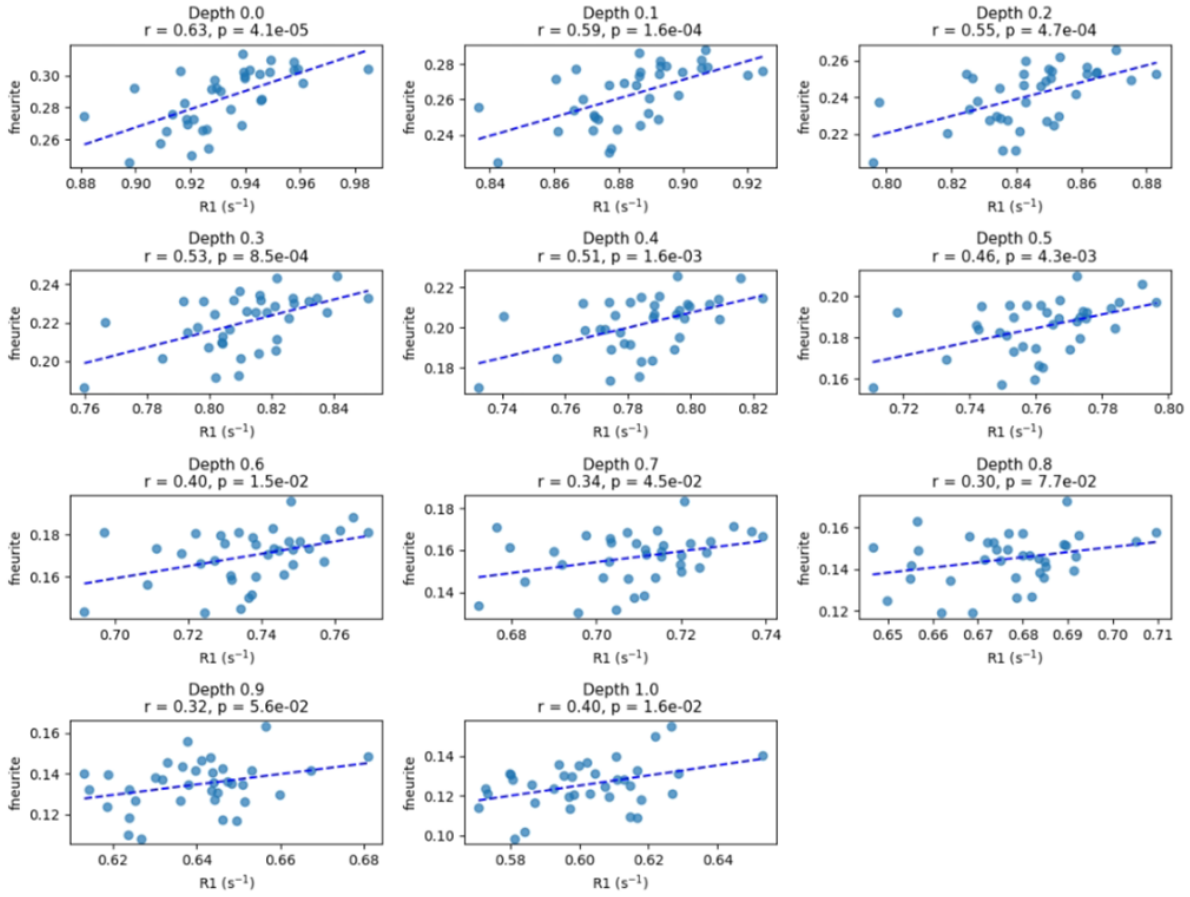


Figure 4.8. Depth-dependent correlations between R1 and intra - neurite signal fraction (fneurite) in the precentral gyrus defined by the Desikan - Killiany atlas (right hemisphere). *Scatter plots show inter-subject correlations between regional mean R1 and fneurite values computed separately at each normalized cortical depth. Each point represents one subject. Pearson correlation coefficients (r) and corresponding p-values are reported in each panel. Cortical depth is expressed as normalized distance from the white matter boundary (0) to the pial surface (1).*

Depth-dependent correlations between R1 and the intra - soma signal fraction (fsoma) were evaluated across subjects at each cortical depth for all regions of interest. In the following, results are illustrated for the precentral gyrus as a representative example (Figures 4.9 - 4.10).

In both hemispheres, fsoma exhibited a significant negative correlation with R1 in superficial and mid-cortical layers. The strongest anti-correlations were observed at depths between 0.0 and 0.4, with correlation coefficients ranging from $r \approx -0.38$ to -0.44 in the left hemisphere ($p < 0.05$) and from $r \approx -0.50$ to -0.57 in the right hemisphere ($p < 0.001$).

With increasing cortical depth, the strength of the negative association progressively decreased. In deeper layers (depth ≥ 0.6), correlations were weak and, in most cases, not statistically

significant. Notably, in the deepest layers (depth 0.9 - 1.0), the relationship changed sign, yielding moderate positive correlations in both hemispheres (left hemisphere: r ≈ 0.34 - 0.57; right hemisphere: r ≈ 0.25 - 0.48), reaching statistical significance at depth 1.0.

Overall, these results indicate a depth-dependent inversion of the relationship between R1 and fsoma: strong negative correlations dominate in superficial cortical layers, gradually weakening with depth and transitioning to positive correlations near the white matter boundary. This pattern was consistently observed in both hemispheres, with systematically stronger effects in the right hemisphere.

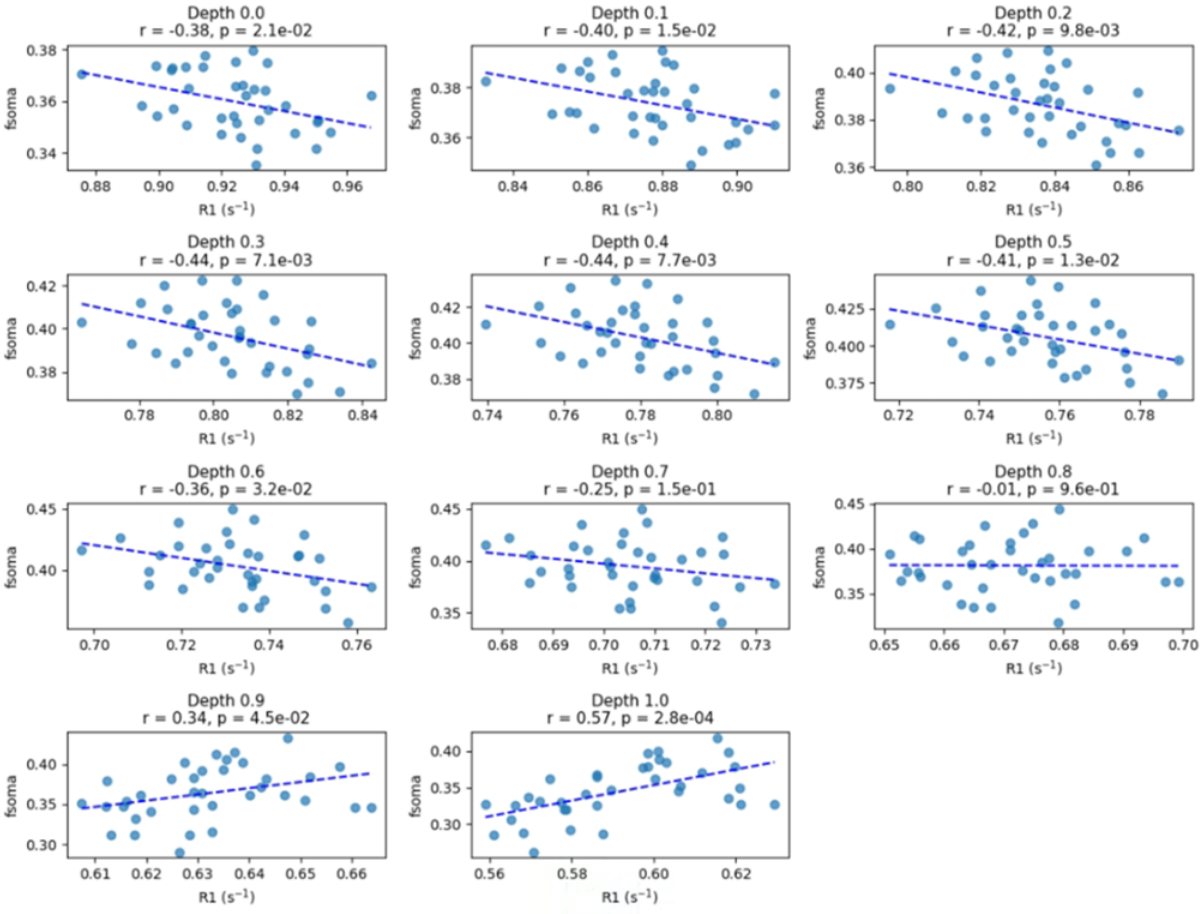


Figure 4.9. Depth-dependent correlations between R1 and intra - soma signal fraction (fsoma) in the precentral gyrus defined by the Desikan - Killiany atlas (left hemisphere). *Scatter plots show inter-subject correlations between regional mean R1 and fsoma values computed separately at each normalized cortical depth. Each point represents one subject. Pearson correlation coefficients (r) and corresponding p-values are reported in each panel. Cortical depth is expressed as normalized distance from the white matter boundary (0) to the pial surface (1).*

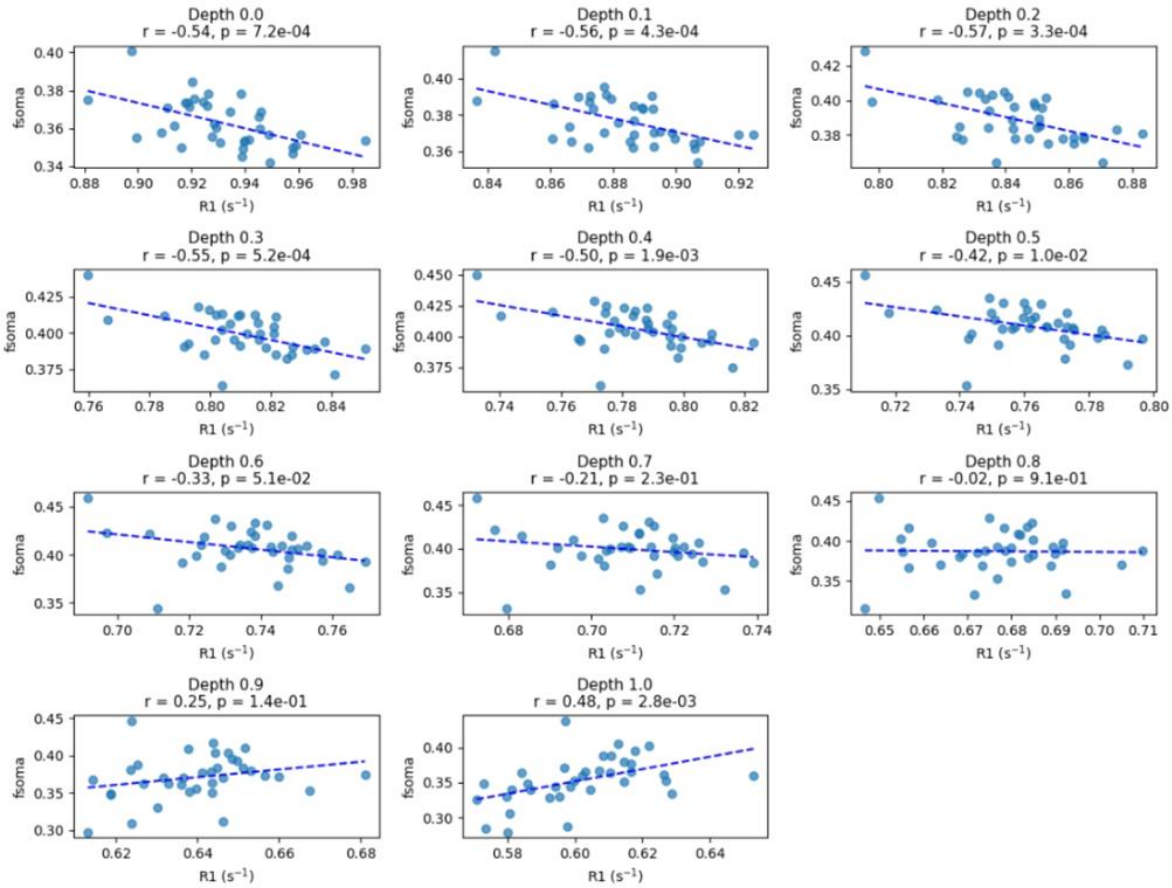


Figure 4.10. Depth-dependent correlations between R1 and intra - soma signal fraction (fsoma) in the precentral gyrus defined by the Desikan - Killiany atlas (right hemisphere). *Scatter plots show inter-subject correlations between regional mean R1 and fsoma values computed separately at each normalized cortical depth. Each point represents one subject. Pearson correlation coefficients (r) and corresponding p-values are reported in each panel. Cortical depth is expressed as normalized distance from the white matter boundary (0) to the pial surface (1).*

Depth-dependent correlations between R1 and the estimated soma radius (Rsoma) were evaluated across subjects at each cortical depth for all regions of interest. In the following, results are illustrated for the precentral gyrus as a representative example **(**Figures 4.11 - 4.12).

In both hemispheres, Rsoma showed a strong and statistically significant negative correlation with R1 in superficial and mid-cortical layers. The strongest anti-correlations were observed between depths 0.0 and 0.5, with correlation coefficients ranging from $r \approx -0.58$ to -0.68 in the left hemisphere ($p < 10^{-4}$) and from $r \approx -0.51$ to -0.64 in the right hemisphere ($p < 10^{-3}$).

With increasing cortical depth, the magnitude of the negative association progressively decreased. In deeper layers (depth ≥ 0.7), correlations became weak and mostly non-significant in both hemispheres. At the deepest depths (0.9 - 1.0), the relationship approached zero or slightly positive values (left hemisphere: r ≈ 0.04 - 0.30; right hemisphere: r ≈ 0.05 - 0.24), none of which reached statistical significance.

Overall, these findings indicate a pronounced depth-dependent relationship between R1 and apparent soma size, characterized by strong negative correlations in superficial and middle cortical layers and a progressive attenuation toward deeper layers. This pattern was consistently observed across hemispheres, suggesting that higher R1 values are associated with smaller apparent soma radii primarily in upper and middle cortical layers.

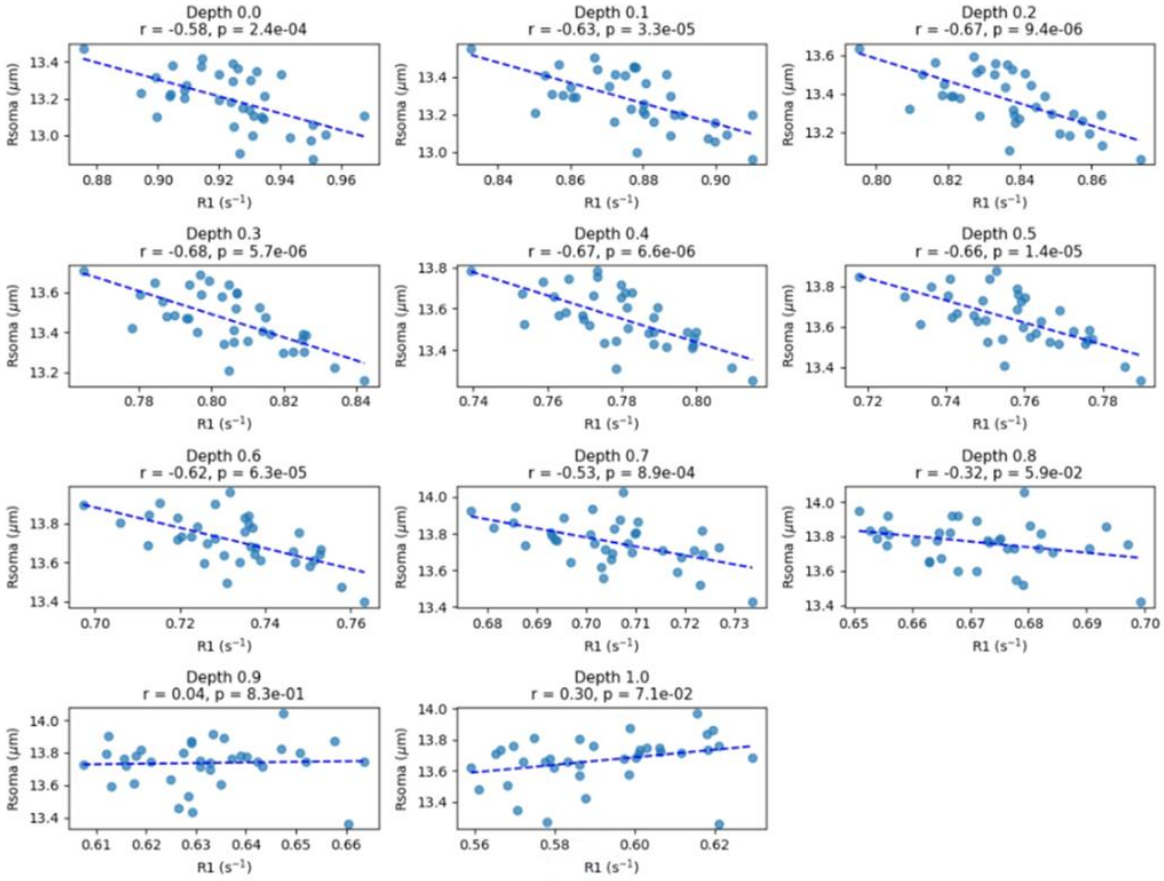


Figure 4.11. Depth-dependent correlations between R1 and estimated soma radius (Rsoma) in the precentral gyrus defined by the Desikan - Killiany atlas (left hemisphere). *Scatter plots show inter-subject correlations between regional mean R1 and Rsoma values computed separately at each normalized cortical depth. Each point represents one subject. Pearson correlation coefficients (r) and corresponding p-values are reported in each panel. Cortical depth is expressed as normalized distance from the white matter boundary (0) to the pial surface (1).*

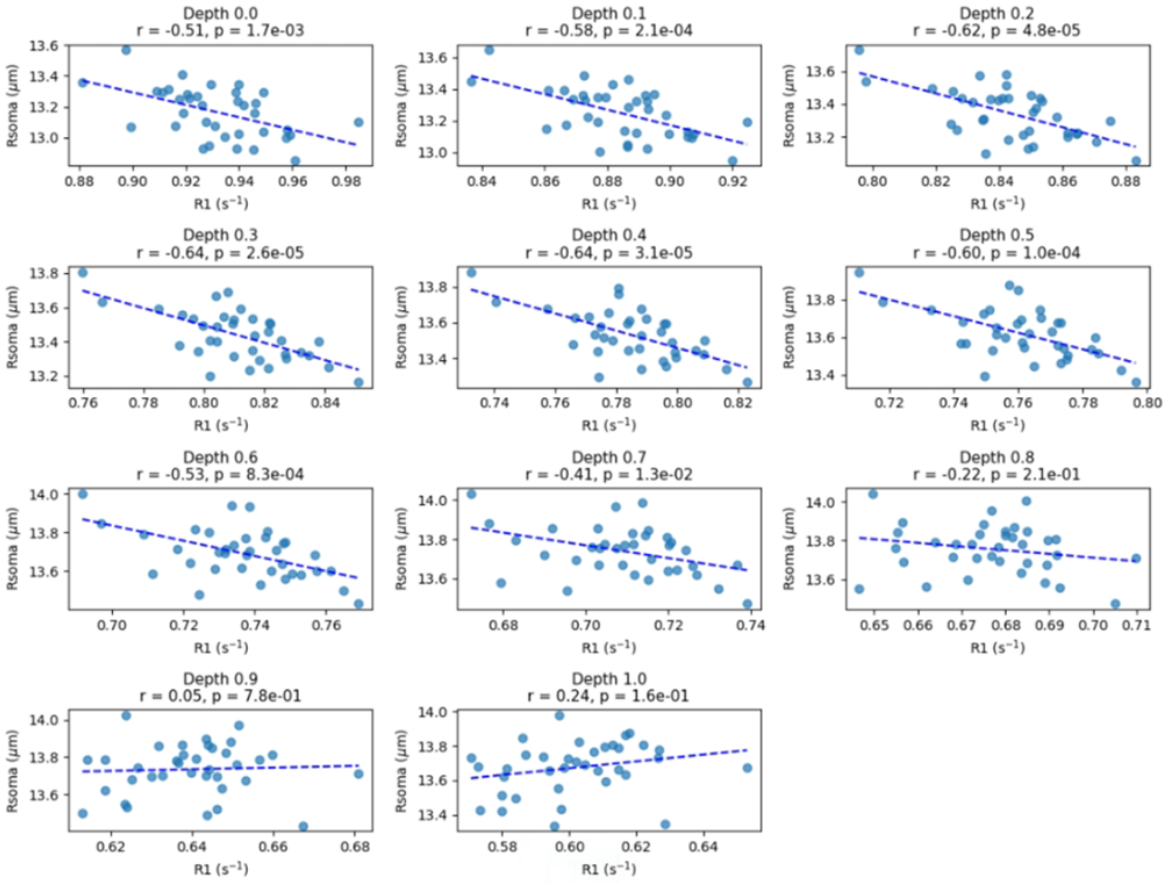


Figure 4.12. Depth-dependent correlations between R1 and estimated soma radius (Rsoma) in the precentral gyrus defined by the Desikan - Killiany atlas (right hemisphere). *Scatter plots show inter-subject correlations between regional mean R1 and Rsoma values computed separately at each normalized cortical depth. Each point represents one subject. Pearson correlation coefficients (r) and corresponding p-values are reported in each panel. Cortical depth is expressed as normalized distance from the white matter boundary (0) to the pial surface (1).*

4.4. Discussion

In this study, we investigated depth-dependent profiles of SANDI-derived microstructural metrics and their relationship with R1, a quantitative marker sensitive to myelin-related cortical tissue properties.

The diffusion acquisition protocol used in this chapter was optimized for SANDI and prioritized high b-values to increase sensitivity to restricted diffusion within a feasible multiparametric MRI session. This choice was appropriate for the aims of the study, which focused on depth-dependent associations between R1 and grey-matter microstructure across the cortical ribbon. In this context, SANDI was particularly suitable because it explicitly

separates soma- and neurite-related signal contributions, whereas models such as NODDI are more strongly oriented toward neurite density and orientation dispersion and do not explicitly model soma-related signal contributions.

Our results demonstrate that the coupling between quantitative MRI contrast and diffusion-derived cellular parameters varies systematically across cortical depth and differs between neurite- and soma-related compartments.

The intra-neurite signal fraction (fneurite) showed a monotonic decrease from deep to superficial cortical depths, closely matching the depth profile of R1. In contrast, the intra-soma signal fraction (fsoma) exhibited a non-monotonic profile with a clear maximum at intermediate depths, while the estimated soma radius (Rsoma) peaked in intermediate-to-deep cortical depths.

These distinct depth-dependent patterns indicate that SANDI metrics capture different aspects of cortical microstructure, reflecting variations in neurite density, soma density, and apparent cell size across the cortical ribbon. The reproducibility of these profiles across regions and hemispheres supports the biological relevance and robustness of SANDI-derived parameters for in vivo characterization of grey matter microstructure.

We observed a consistent positive association between R1 and fneurite across cortical depth, with the strongest correlations in superficial depths and progressively weaker correlations toward deeper regions.

This finding suggests that higher R1 values are associated with increased neurite-related signal, but that this relationship is not uniform across the cortex. The attenuation of the correlation at deeper depths indicates that the coupling between R1-related cortical tissue properties and the neurite-related signal captured by fneurite depends on cortical depth, likely reflecting differences in axonal composition, dendritic contribution, and packing density across the cortical ribbon.

These results provide a depth-resolved explanation for the moderate correlations previously reported between R1 and neurite-related diffusion metrics using cortex-averaged analyses.

Both fsoma and Rsoma showed strong negative correlations with R1 in superficial and mid-cortical depths, which progressively weakened and inverted near the white matter boundary.

This pattern indicates that regions with higher R1 values tend to exhibit lower soma-related signal fraction and smaller apparent soma radii in superficial and intermediate depths, while

this relationship disappears or reverses in deeper cortical regions. The depth-dependent inversion suggests that soma-related microstructural properties and R1-related cortical tissue properties follow partially opposing gradients across the cortex and are governed by different biological factors depending on cortical depth.

Importantly, these findings demonstrate that the relationship between R1 and soma-related microstructure cannot be described by a single global association but is strongly depth-dependent.

Together, our results show that correlations between R1 and diffusion-derived microstructural parameters are highly depth-specific and compartment-dependent. Analyses based on region-averaged cortical values obscure these systematic variations and may lead to incomplete or misleading interpretations of the relationship between cortical microstructure and R1.

Depth-resolved multi-parametric approaches therefore provide a more accurate framework for studying cortical organization in vivo and may be particularly valuable for investigating developmental processes, aging, and neurological disorders, where specific cortical depths and cellular compartments are differentially affected.

Limitations and implications for Future Research

Several limitations of the present study should be acknowledged.

First, an important limitation of the depth-resolved analysis is the potentially strong partial volume effect, given the mismatch between the native acquisition resolution and the thin cortical ribbon. In this study, diffusion-derived microstructural metrics were acquired at 1.8-mm isotropic resolution, while R1 maps were acquired at 1-mm isotropic resolution (MP2RAGE). Depth profiles were sampled along the cortical ribbon using FreeSurfer surface-based coordinates defined by projfrac (from 0 at the white matter boundary to 1 at the pial surface), in steps of 0.1. These depth samples represent fractional positions interpolated between the two surfaces and therefore do not imply millimetre-scale spatial resolution within the cortex. Consequently, estimated depth-dependent profiles may be substantially influenced by signal mixing with tissue compartments outside the cortex, particularly white matter near the WM boundary and CSF near the pial surface, as well as by uncertainties in surface placement and map projection. Nevertheless, recent high-resolution diffusion MRI work using ultra-high-gradient systems has demonstrated that depth-dependent microstructure analyses can reveal biologically plausible laminar profiles in vivo under optimised acquisition and modelling conditions. This supports the qualitative trends reported here, while underscoring

that higher native resolution and explicit partial-volume control will be important in future work [133].

Second, cortical depth was defined using normalized surface-based coordinates (*projfrac*) and does not correspond to histologically defined cortical layers. While this approach enables robust sampling across the cortical ribbon and minimizes biases due to regional thickness differences, direct correspondence with cytoarchitectonic layers cannot be assumed. Future studies combining in vivo depth-resolved MRI with post-mortem histology or ultra-high-resolution imaging may help establish more precise links between SANDI parameters, R1, and cellular architecture.

Third, the SANDI model provides apparent microstructural parameters that depend on model assumptions and acquisition protocol. In particular, estimates of soma radius and compartmental signal fractions may be influenced by partial volume effects, limited gradient strength, and the simplified representation of complex cellular geometries. The use of stronger gradient systems and extended diffusion protocols could further improve parameter specificity and sensitivity.

Finally, correlations were computed across subjects using regional mean values at each cortical depth. This approach captures inter-individual variability but does not address within-subject spatial coupling between R1 and SANDI metrics at the vertex or voxel level. Future work could explore subject-specific depth-dependent correlations and assess their spatial consistency across the cortex. In addition, the present cohort consisted of healthy young and middle-aged adults; the generalizability of the observed depth-dependent relationships to developmental stages, aging populations, or neurological disorders remains to be established. Applying the proposed framework to clinical populations may provide insight into depth-specific microstructural alterations associated with demyelination, neurodegeneration, or abnormal cellular organization.

4.5. Conclusions

This study demonstrates that the relationship between cortical myelination, quantified by R1, and diffusion-derived microstructural properties from the SANDI model is strongly dependent on cortical depth and on the specific cellular compartment being probed.

Neurite-related microstructure exhibits a positive association with R1 that is strongest at superficial cortical depths and progressively weakens toward deeper regions. In contrast, soma-related metrics show pronounced negative correlations with R1 in superficial and intermediate depths, followed by attenuation and inversion near the white matter boundary.

These findings indicate that cortex-averaged analyses obscure systematic depth-dependent variations in microstructural–myelin coupling and that multi-parametric, depth-resolved approaches provide a more accurate characterization of cortical organization in vivo.

By integrating quantitative R1 mapping with SANDI-based microstructural modeling, this work establishes a framework for disentangling distinct cellular contributions to MRI contrast across the cortical ribbon and highlights the potential of depth-resolved MRI to study normal cortical architecture and its alteration in disease.

Importantly, the observed depth-dependent profiles are reproducible across subjects and regions and are consistent with established histological knowledge of cellular and myelin distributions, particularly with respect to the relative concentration of neuronal cell bodies and myelinated fibers at different cortical depths. Overall, these results show that detailed depth-dependent characterization of cortical microstructure is feasible using clinically available MRI hardware and acquisition protocols, thereby contributing to narrowing the gap between post-mortem histology and in vivo neuroimaging and providing a foundation for the development of non-invasive biomarkers sensitive to subtle, depth-specific microstructural alterations relevant to neurodevelopment, aging, and a wide range of neurological and psychiatric disorders.

5. General conclusions

This PhD thesis focuses on the non-invasive investigation of grey matter (GM) microstructure using magnetic resonance imaging (MRI) and examines how microstructural parameters derived from multi-compartment diffusion modelling relate to the longitudinal relaxation rate R1 (1/T1), a widely used quantitative marker sensitive to myelin-related cortical tissue properties, as well as to functional brain activity measured with BOLD-fMRI in healthy volunteers. Across the three experimental chapters, the thesis delivers a coherent message: R1 contrast in GM is shaped by multiple microstructural determinants, and the relationship between diffusion-derived metrics and R1 is both compartment-dependent and depth-dependent. In addition, the fraction of restricted water diffusion in GM, expressed by FR in the Composite Hindered and Restricted Model of Diffusion MRI (CHARMED) shows a consistent relationship with R1 across many regions, but its relationship with task-evoked BOLD responses is region-specific, suggesting that microstructure-function coupling is not uniform across the motor network.

The work was designed around a progressive set of questions. First, can diffusion metrics that explicitly model GM cytoarchitecture (soma- and neurite-related compartments) account for meaningful variance in R1, beyond the traditional qualitative interpretation of "T1w contrast"? Second, does the fraction of restricted water diffusion (FR) relate to functional activation during a visuomotor learning paradigm, and can this help bridge microstructure with function? Third, are the relationships between R1 and GM microstructure uniform across cortical thickness, or do they systematically vary with cortical depth in ways that are hidden when measures are averaged across the cortical ribbon?

These questions were addressed by combining quantitative R1 mapping (MP2RAGE at 3T) with advanced diffusion modelling (SANDI and CHARMED), complemented by task fMRI in a subset of participants. The overall framework treats cortical tissue as a multi-compartment entity (soma, neurites, extra-neurite space) and considers R1 not as a "myelin index", but as a quantitative signal influenced by myelin and other microstructural contributors (e.g., water content, iron), whose interpretation can be sharpened through multimodal imaging and advanced modelling.

Chapter 2 tested whether diffusion metrics with high sensitivity to cortical GM microstructure, derived from high b-value diffusion-weighted data using the three-compartment Soma and Neurite Density Imaging (SANDI) model, are significantly associated with R1 (1/T1). Twenty healthy volunteers underwent diffusion-weighted MRI and quantitative R1 mapping using MP2RAGE at 3T. Voxel-wise and regional correlations between SANDI metrics and R1 were examined within cortical GM; for completeness and comparison, associations in WM were also evaluated.

In GM, the main finding was a moderate negative association between R1 and soma-related metrics, specifically fsoma and Rsoma (spatial correlations: $r \approx -0.47$ and -0.35), with similar effects across subjects (fsoma and Rsoma: $r \approx -0.56$ and -0.48). These results indicate that GM microstructure, and in particular the soma-related compartment estimated by SANDI, contributes to shaping R1 contrast. In WM, the pattern differed, with moderate-to-strong positive correlations between R1 and intra-neurite metrics, especially Din and fneurite ($r \approx 0.53$ and 0.30), consistent with the contribution of myelinated axons to the intra-neurite water pool.

Taken together, Chapter 2 shows that the associations between diffusion-derived microstructural metrics and R1 differ across tissue types and compartments: in cortical GM, R1 is primarily linked to soma-related SANDI parameters (negative associations with fsoma and Rsoma, alongside positive associations with extra-neurite metrics), whereas in WM R1 relates mainly to intra-neurite properties most robustly to Din after accounting for ROI volume-consistent with a stronger contribution of myelinated axons to the WM R1 contrast.

Chapter 3 aimed to clarify the biophysical meaning of the fraction of restricted water diffusion in GM, expressed by FR, estimated with the CHARMED model. Specifically, we tested whether FR is associated with R1 (1/T1), an MP2RAGE-derived quantitative marker sensitive to myelin-related cortical tissue properties and whether it relates to functional activation measured as task-evoked BOLD responses during repeated execution of a visuomotor learning task. Data from 20 healthy volunteers included BOLD-fMRI, quantitative R1 mapping, and diffusion MRI for FR quantification.

Across subjects, FR correlated positively with R1 in most GM ROIs, supporting a robust link between restricted diffusion properties and tissue characteristics reflected by R1. However, the relationship between FR and task-evoked BOLD was not widespread across the motor network: a strong negative correlation emerged only in the left supplementary motor cortex ($r \approx -0.79$, $p < 0.0001$), a region implicated in the control of internally generated movements.

This dissociation is important conceptually. It suggests that although FR often covaries with R1 across cortex, its functional relevance can be localized and circuit-dependent.

Chapter 4 tested the hypothesis that the relationship between R1, a quantitative marker sensitive to myelin-related cortical tissue properties, and diffusion-derived microstructural metrics from SANDI is systematically dependent on cortical depth and differs across cellular compartments. Using a surface-based, depth-resolved approach, quantitative R1 and SANDI parametric maps (fneurite, fsoma, Rsoma) were projected onto the reconstructed cortical surfaces and sampled across normalized cortical depth (0.1). Data were acquired in 40 healthy adults on a standard clinical 3T MRI system.

Depth profiling revealed distinct trajectories for neurite- and soma-related metrics. fneurite decreased monotonically from deep to superficial depths, closely matching the R1 profile. In contrast, fsoma showed a non-monotonic pattern with a maximum at intermediate depths (≈ 0.4-0.6), while Rsoma peaked in intermediate-to-deep depths (≈ 0.6-0.8). Critically, depth-resolved correlations demonstrated strong compartment-specific coupling: R1 correlated positively with fneurite, with the strongest associations in superficial depths and progressively weaker coupling toward deeper regions, whereas fsoma and Rsoma showed pronounced negative correlations with R1 in superficial and mid-cortical depths, followed by attenuation and partial inversion near the WM boundary.

These results indicate that cortex-averaged analyses can miss structured biological effects and may blur meaningful relationships between microstructural metrics and R1. Depth-resolved multimodal MRI therefore provides a more accurate in vivo description of cortical organization by exposing systematic coupling patterns that are otherwise hidden.

Future Perspectives

The work presented in this thesis demonstrates that combining quantitative R1 mapping with biophysically motivated diffusion models (SANDI and CHARMED), and, where available, BOLD-fMRI, provides a coherent framework for probing grey-matter microstructure, R1-related cortical tissue properties, and their functional relevance in vivo. Several lines of development naturally follow from these results, spanning clinical translation, methodological refinement, and applications to cognition and lifespan neuroscience.

The first direction concerns translation to clinical populations. The compartment- and depth-specific relationships between R1 and diffusion-derived metrics observed in healthy cortex provide a principled baseline against which pathological deviations can be interpreted.

Conditions such as Multiple Sclerosis, other demyelinating diseases, and neurodegenerative disorders affecting GM are particularly relevant, as they combine demyelination, inflammation, changes in water content, and neuro-axonal loss. Applying the same multi-parametric protocol and analysis framework in these cohorts could help disentangle whether disease-related reductions in R1 predominantly reflect loss of myelin, alterations in soma- and neurite-related compartments, or changes in extra-neurite space. In this context, depth-resolved analyses may be especially informative for identifying layer- or depth-selective vulnerability that is not captured by cortex-averaged measures.

A second key avenue is methodological refinement of quantitative MRI and diffusion modelling. The present work relied on MP2RAGE-derived "apparent" R1 and on SANDI/CHARMED models under specific acquisition regimes and modelling assumptions. Future studies should aim to integrate R1 with advanced multi-parameter mapping protocols, in order to better separate myelin-related effects from contributions of water content, iron, and other macromolecular pools. On the diffusion side, extending the modelling to explicitly account for exchange, non-Gaussian effects, and more realistic geometries, as well as optimizing b-values, diffusion times, and gradient strengths, would improve the specificity and robustness of compartment estimates, particularly in cortical GM where microstructure is highly heterogeneous and partial-volume effects are prominent.

Third, the results from Chapters 3 and 4 motivate richer investigations of structure–function coupling. In this thesis, functional relevance was assessed using task-evoked BOLD responses during a visuomotor learning paradigm and by examining depth-dependent relationships between R1 and SANDI metrics. Future work could extend this by combining depth-resolved microstructural measures with high-resolution laminar fMRI or alternative functional readouts such as ASL-derived perfusion or calibrated fMRI, to separate neuronal and vascular contributions more clearly. Beyond simple correlations, model-based approaches that explicitly link microstructural parameters to expected haemodynamic responses and network dynamics could help clarify when and where microstructural differences translate into differences in functional recruitment or efficiency.

A further important direction is longitudinal and lifespan applications. The present work focused on healthy young and middle-aged adults. Applying the same framework across developmental stages, healthy aging, and longitudinally in individuals would help characterize how compartment-specific R1-microstructure relationships evolve over time, and whether depth-resolved profiles exhibit characteristic trajectories or turning points. In clinical cohorts,

repeated measures could be used to test whether changes in R1 and diffusion-derived metrics provide complementary markers of disease progression or treatment response, potentially supporting personalized prognosis and therapy monitoring.

Finally, there is scope for integration with behavioural and cognitive phenotyping. The microstructural heterogeneity revealed here across regions, compartments, and cortical depth-likely underpins individual differences in learning, cognition, and resilience. Future studies could therefore combine the proposed MRI framework with detailed behavioural assessments and cognitive tasks, probing whether specific microstructural signatures (for example, particular combinations of neurite fraction, soma properties, and R1 in selected depths) are associated with performance, adaptability, or vulnerability to cognitive decline.

In summary, this thesis establishes a methodological and conceptual basis for interpreting cortical R1 contrast in the context of multi-compartment diffusion modelling and, where available, functional imaging. Building on this foundation through clinical, methodological, longitudinal, and cognitive extensions will be essential for turning depth-resolved, multi-parametric MRI into a practical tool for studying normal cortical organization and for detecting subtle, spatially specific microstructural alterations in neurological and psychiatric disease.

References

[1] J. H. S. E. R. Kandel, THOMAS M. JESSELL, STEVEN A. SIEGELBAUM, and A. J. HUDSPETH, *Principles of Neural Science*. 2013.

[2] Purves D., Augustine G. J., Fitzpatrick D., Hall W. C., LaMantia A.-S., White L. E., *NEUROSCIENCE, Sixth Edition*. Oxford University Press, 2018.

[3] F. Naz and Y. H. Siddique, 'Human Brain Disorders: A Review', *Open Biol. J.*, vol. 8, no. 1, pp. 6–21, Sep. 2020, doi: 10.2174/1874196702008010006.

[4] J. G. Betts *et al.*, '12.2 Nervous Tissue - Anatomy and Physiology 2e | OpenStax'. Accessed: Nov. 12, 2025. [Online]. Available: https://openstax.org/books/anatomy-and-physiology-2e/pages/12-2-nervous-tissue

[5] E. M. Marcus, S. Jacobson, and T. D. Sabin, 'Cerebral Cortex: Cytoarchitecture, Physiology, and Overview of Functional Localization.', *Oxford University Press*, 2014.

[6] K. Brodmann, *Vergleichende Lokalisationslehre der Grosshirnrinde.* Verlag von Johann Ambrosius Barth, 1909.

[7] B. Fischl and A. M. Dale, 'Measuring the thickness of the human cerebral cortex from magnetic resonance images', *Proc. Natl. Acad. Sci.*, vol. 97, no. 20, pp. 11050–11055, Sep. 2000, doi: 10.1073/pnas.200033797.

[8] J. L. Goldberg, 'How does an axon grow?', *Genes Dev.*, vol. 17, no. 8, pp. 941–958, Apr. 2003, doi: 10.1101/gad.1062303.

[9] C. Filley, *White Matter Structure and Function.* Oxford University Press, 2013.

[10] S. G. Waxman, J. D. Kocsis, and P. K. Stys., *The axon. Structure, Function and Pathophysiology.* Oxford University Press, New York, 1995.

[11] F. Aboitiz, A. B. Scheibel, R. S. Fisher, and E. Zaidel, 'Brain Research', *Fiber Compos. Hum. Corpus Callosum*, vol. Volume 598, Issues 1–2, pp. 143–153, doi: https://doi.org/10.1016/0006-8993(92)90178-C.

[12] J. Guy, A. E. Ellis, K. Kelley, and M. G. Hope, 'The Journal of Comparative Neurology', *Spectra G Ratio Myelin Sheath Thick. Axon Fiber Diameter Guin. Pig Opt. Nerve*, pp. 446–454, 1992.

[13] N. Stikov *et al.*, 'Quantitative analysis of the myelin g -ratio from electron microscopy images of the macaque corpus callosum', *Data Brief*, vol. 4, pp. 368–373, Sep. 2015, doi: 10.1016/j.dib.2015.05.019.

[14] S. Tomasi, R. Caminiti, and Innocenti G. M., 'Cerebral Cortex', *Areal Differ. Diameter Length Corticofugal Proj.*, vol. Volume 22, pp. 1463–1472, 2012, doi: https://doi.org/10.1093/cercor/bhs011.

[15] C. Filley, *Neurobiology of White Matter Disorders.* Oxford University Press, 2013.

[16] N. A. Bock *et al.*, 'Optimizing T1-weighted imaging of cortical myelin content at 3.0 T', *NeuroImage*, vol. 65, pp. 1–12, Jan. 2013, doi: 10.1016/j.neuroimage.2012.09.051.

[17] M. F. Glasser and D. C. Van Essen, 'Mapping human cortical areas in vivo based on myelin content as revealed by T1- and T2-weighted MRI', *J. Neurosci. Off. J. Soc. Neurosci.*, vol. 31, no. 32, pp. 11597–11616, Aug. 2011, doi: 10.1523/JNEUROSCI.2180-11.2011.

[18] A. Lutti, F. Dick, M. I. Sereno, and N. Weiskopf, 'Using high-resolution quantitative mapping of R1 as an index of cortical myelination', *NeuroImage*, vol. 93 Pt 2, pp. 176–188, Jun. 2014, doi: 10.1016/j.neuroimage.2013.06.005.

[19] J. P. Mottershead *et al.*, 'High field MRI correlates of myelin content and axonal density in multiple sclerosis--a post-mortem study of the spinal cord', *J. Neurol.*, vol. 250, no. 11, pp. 1293–1301, Nov. 2003, doi: 10.1007/s00415-003-0192-3.

[20] K. Schmierer, F. Scaravilli, D. R. Altmann, G. J. Barker, and D. H. Miller, 'Magnetization transfer ratio and myelin in postmortem multiple sclerosis brain', *Ann. Neurol.*, vol. 56, no. 3, pp. 407–415, Sep. 2004, doi: 10.1002/ana.20202.

[21] S. B. Eickhoff *et al.*, 'A new SPM toolbox for combining probabilistic cytoarchitectonic maps and functional imaging data', *NeuroImage*, vol. 25, no. 4, pp. 1325–1335, May 2005, doi: 10.1016/j.neuroimage.2004.12.034.

[22] N. B. Walters *et al.*, '*In vivo* identification of human cortical areas using high-resolution MRI: An approach to cerebral structure–function correlation', *Proc. Natl. Acad. Sci.*, vol. 100, no. 5, pp. 2981–2986, Mar. 2003, doi: 10.1073/pnas.0437896100.

[23] J. P. Marques, T. Kober, G. Krueger, W. Van Der Zwaag, P.-F. Van De Moortele, and R. Gruetter, 'MP2RAGE, a self bias-field corrected sequence for improved segmentation and T1-mapping at high field', *NeuroImage*, vol. 49, no. 2, pp. 1271–1281, Jan. 2010, doi: 10.1016/j.neuroimage.2009.10.002.

[24] J. P. Mugler and J. R. Brookeman, 'Three-dimensional magnetization-prepared rapid gradient-echo imaging (3D MP RAGE)', *Magn. Reson. Med.*, vol. 15, no. 1, pp. 152–157, Jul. 1990, doi: 10.1002/mrm.1910150117.

[25] J. P. Marques and R. Gruetter, 'New Developments and Applications of the MP2RAGE Sequence - Focusing the Contrast and High Spatial Resolution R1 Mapping', *PLoS ONE*, vol. 8, no. 7, p. e69294, Jul. 2013, doi: 10.1371/journal.pone.0069294.

[26] M. D. Waehnert *et al.*, 'Anatomically motivated modeling of cortical laminae', *NeuroImage*, vol. 93, pp. 210–220, Jun. 2014, doi: 10.1016/j.neuroimage.2013.03.078.

[27] I. O. Jelescu and M. D. Budde, 'Design and validation of diffusion MRI models of white matter', *Front. Phys.*, vol. 28, p. 61, Nov. 2017, doi: 10.3389/fphy.2017.00061.

[28] H. Zhang, T. Schneider, C. A. Wheeler-Kingshott, and D. C. Alexander, 'NODDI: Practical *in vivo* neurite orientation dispersion and density imaging of the human brain', *NeuroImage*, vol. 61, no. 4, pp. 1000–1016, Jul. 2012, doi: 10.1016/j.neuroimage.2012.03.072.

[29] Y. Assaf and P. J. Basser, 'Composite hindered and restricted model of diffusion (CHARMED) MR imaging of the human brain', *NeuroImage*, vol. 27, no. 1, pp. 48–58, Aug. 2005, doi: 10.1016/j.neuroimage.2005.03.042.

[30] M. Palombo *et al.*, 'SANDI: A compartment-based model for non-invasive apparent soma and neurite imaging by diffusion MRI', *NeuroImage*, vol. 215, p. 116835, Jul. 2020, doi: 10.1016/j.neuroimage.2020.116835.

[31] S. Ogawa *et al.*, 'Intrinsic signal changes accompanying sensory stimulation: functional brain mapping with magnetic resonance imaging', *Proc. Natl. Acad. Sci. U. S. A.*, vol. 89, no. 13, pp. 5951–5955, Jul. 1992, doi: 10.1073/pnas.89.13.5951.

[32] S. Ogawa and T. M. Lee, 'Magnetic resonance imaging of blood vessels at high fields: in vivo and in vitro measurements and image simulation', *Magn. Reson. Med.*, vol. 16, no. 1, pp. 9–18, Oct. 1990, doi: 10.1002/mrm.1910160103.

[33] N. K. Logothetis, J. Pauls, M. Augath, T. Trinath, and A. Oeltermann, 'Neurophysiological investigation of the basis of the fMRI signal', *Nature*, vol. 412, no. 6843, pp. 150–157, Jul. 2001, doi: 10.1038/35084005.

[34] B. Biswal, F. Z. Yetkin, V. M. Haughton, and J. S. Hyde, 'Functional connectivity in the motor cortex of resting human brain using echo-planar MRI', *Magn. Reson. Med.*, vol. 34, no. 4, pp. 537–541, Oct. 1995, doi: 10.1002/mrm.1910340409.

[35] M. D. Fox and M. E. Raichle, 'Spontaneous fluctuations in brain activity observed with functional magnetic resonance imaging', *Nat. Rev. Neurosci.*, vol. 8, no. 9, pp. 700–711, Sep. 2007, doi: 10.1038/nrn2201.

[36] R. Brown, 'XXVII. A brief account of microscopical observations made in the months of June, July and August 1827, on the particles contained in the pollen of plants; and on the general existence of active molecules in organic and inorganic bodies', *Philos. Mag.*, vol. 4, no. 21, pp. 161–173, Sep. 1828, doi: 10.1080/14786442808674769.

[37] R. Turner, D. Le Bihan, J. Maier, R. Vavrek, L. K. Hedges, and J. Pekar, 'Echo-planar imaging of intravoxel incoherent motion', *Radiology*, vol. 177, no. 2, pp. 407–414, Nov. 1990, doi: 10.1148/radiology.177.2.2217777.

[38] D. Le Bihan, 'Molecular diffusion, tissue microdynamics and microstructure', *NMR Biomed.*, vol. 8, no. 7–8, pp. 375–386, 1995, doi: 10.1002/nbm.1940080711.

[39] M. E. Moseley *et al.*, 'Diffusion-weighted MR imaging of anisotropic water diffusion in cat central nervous system', *Radiology*, vol. 176, no. 2, pp. 439–445, Aug. 1990, doi: 10.1148/radiology.176.2.2367658.

[40] Y. Assaf, R. Z. Freidlin, G. K. Rohde, and P. J. Basser, 'New modeling and experimental framework to characterize hindered and restricted water diffusion in brain white matter', *Magn. Reson. Med.*, vol. 52, no. 5, pp. 965–978, Nov. 2004, doi: 10.1002/mrm.20274.

[41] C. Beaulieu, 'The basis of anisotropic water diffusion in the nervous system - a technical review', *NMR Biomed.*, vol. 15, no. 7–8, pp. 435–455, 2002, doi: 10.1002/nbm.782.

[42] D. S. Novikov, E. Fieremans, S. N. Jespersen, and V. G. Kiselev, 'Quantifying brain microstructure with diffusion MRI: Theory and parameter estimation', *NMR Biomed.*, vol. 32, no. 4, p. e3998, Apr. 2019, doi: 10.1002/nbm.3998.

[43] P. van Gelderen, D. DesPres, P. C. van Zijl, and C. T. Moonen, 'Evaluation of restricted diffusion in cylinders. Phosphocreatine in rabbit leg muscle', *J. Magn. Reson. B*, vol. 103, no. 3, pp. 255–260, Mar. 1994, doi: 10.1006/jmrb.1994.1038.

[44] E. T. McKinnon, J. H. Jensen, G. R. Glenn, and J. A. Helpern, 'Dependence on b-value of the direction-averaged diffusion-weighted imaging signal in brain', *Magn. Reson. Imaging*, vol. 36, pp. 121–127, Feb. 2017, doi: 10.1016/j.mri.2016.10.026.

[45] M. Palombo, N. Shemesh, A. Ianus, D. Alexander, and H. Zhang, 'Abundance of cell bodies can explain the stick model's failure in grey matter at high bvalue', presented at the Joint Annual Meeting ISMRM-ESMRMB 2018, Jun. 2018. Accessed: Nov. 22, 2024. [Online]. Available: https://orca.cardiff.ac.uk/id/eprint/147883/

[46] D. M. Yang, J. E. Huettner, G. L. Bretthorst, J. J. Neil, J. R. Garbow, and J. J. H. Ackerman, 'Intracellular water preexchange lifetime in neurons and astrocytes', *Magn. Reson. Med.*, vol. 79, no. 3, pp. 1616–1627, Mar. 2018, doi: 10.1002/mrm.26781.

[47] L. Pauling and C. D. Coryell, 'The Magnetic Properties and Structure of Hemoglobin, Oxyhemoglobin and Carbonmonoxyhemoglobin', *Proc. Natl. Acad. Sci. U. S. A.*, vol. 22, no. 4, pp. 210–216, Apr. 1936, doi: 10.1073/pnas.22.4.210.

[48] S. Ogawa, T. M. Lee, A. S. Nayak, and P. Glynn, 'Oxygenation-sensitive contrast in magnetic resonance image of rodent brain at high magnetic fields', *Magn. Reson. Med.*, vol. 14, no. 1, pp. 68–78, Apr. 1990, doi: 10.1002/mrm.1910140108.

[49] S. Ogawa, T. M. Lee, A. R. Kay, and D. W. Tank, 'Brain magnetic resonance imaging with contrast dependent on blood oxygenation', *Proc. Natl. Acad. Sci. U. S. A.*, vol. 87, no. 24, pp. 9868–9872, Dec. 1990, doi: 10.1073/pnas.87.24.9868.

[50] K. R. Thulborn, J. C. Waterton, P. M. Matthews, and G. K. Radda, 'Oxygenation dependence of the transverse relaxation time of water protons in whole blood at high field', *Biochim. Biophys. Acta*, vol. 714, no. 2, pp. 265–270, Feb. 1982, doi: 10.1016/0304-4165(82)90333-6.

[51] P. Jezzard *et al.*, 'Comparison of EPI gradient-echo contrast changes in cat brain caused by respiratory challenges with direct simultaneous evaluation of cerebral oxygenation via a cranial window', *NMR Biomed.*, vol. 7, no. 1–2, pp. 35–44, Mar. 1994, doi: 10.1002/nbm.1940070107.

[52] R. L. Grubb, M. E. Raichle, J. O. Eichling, and M. M. Ter-Pogossian, 'The Effects of Changes in Pa CO_2 Cerebral Blood Volume, Blood Flow, and Vascular Mean Transit Time', *Stroke*, vol. 5, no. 5, pp. 630–639, Sep. 1974, doi: 10.1161/01.STR.5.5.630.

[53] R. P. Kennan, B. E. Scanley, R. B. Innis, and J. C. Gore, 'Physiological basis for BOLD MR signal changes due to neuronal stimulation: Separation of blood volume and magnetic susceptibility effects', *Magn. Reson. Med.*, vol. 40, no. 6, pp. 840–846, 1998, doi: 10.1002/mrm.1910400609.

[54] G. M. Hathout *et al.*, 'A quantitative physiologic model of blood oxygenation for functional magnetic resonance imaging', *Invest. Radiol.*, vol. 30, no. 11, pp. 669–682, Nov. 1995, doi: 10.1097/00004424-199511000-00007.

[55] T. Ernst and J. Hennig, 'Observation of a fast response in functional MR', *Magn. Reson. Med.*, vol. 32, no. 1, pp. 146–149, Jul. 1994, doi: 10.1002/mrm.1910320122.

[56] E. Bliakharskaia *et al.*, 'Exploring the contribution of gray matter microstructure to R1 contrast via multi-compartment diffusion modelling in the healthy brain', *NeuroImage*, vol. 320, p. 121466, Oct. 2025, doi: 10.1016/j.neuroimage.2025.121466.

[57] M. F. Glasser, M. S. Goyal, T. M. Preuss, M. E. Raichle, and D. C. Van Essen, 'Trends and properties of human cerebral cortex: correlations with cortical myelin content', *NeuroImage*, vol. 93 Pt 2, pp. 165–175, Jun. 2014, doi: 10.1016/j.neuroimage.2013.03.060.

[58] A. Kutzelnigg *et al.*, 'Cortical demyelination and diffuse white matter injury in multiple sclerosis', *Brain*, vol. 128, no. 11, pp. 2705–2712, Nov. 2005, doi: 10.1093/brain/awh641.

[59] G. R. Davies *et al.*, 'Evidence for grey matter MTR abnormality in minimally disabled patients with early relapsing-remitting multiple sclerosis', *J. Neurol. Neurosurg. Psychiatry*, vol. 75, no. 7, pp. 998–1002, Jul. 2004, doi: 10.1136/jnnp.2003.021915.

[60] M. F. Callaghan, G. Helms, A. Lutti, S. Mohammadi, and N. Weiskopf, 'A General Linear Relaxometry Model of R1 Using Imaging Data', *Magn. Reson. Med.*, vol. 73, no. 3, pp. 1309–1314, Mar. 2015, doi: 10.1002/mrm.25210.

[61] N. Gelman, J. R. Ewing, J. M. Gorell, E. M. Spickler, and E. G. Solomon, 'Interregional variation of longitudinal relaxation rates in human brain at 3.0 T: relation to estimated iron and water contents', *Magn. Reson. Med.*, vol. 45, no. 1, pp. 71–79, Jan. 2001, doi: 10.1002/1522-2594(200101)45:1<71::aid-mrm1011>3.0.co;2-2.

[62] K. D. Harkins *et al.*, 'The microstructural correlates of T1 in white matter', *Magn. Reson. Med.*, vol. 75, no. 3, pp. 1341–1345, Mar. 2016, doi: 10.1002/mrm.25709.

[63] K. Schmierer *et al.*, 'Quantitative magnetic resonance of postmortem multiple sclerosis brain before and after fixation', *Magn. Reson. Med.*, vol. 59, no. 2, pp. 268–277, Feb. 2008, doi: 10.1002/mrm.21487.

[64] K. Schmierer, F. Scaravilli, D. R. Altmann, G. J. Barker, and D. H. Miller, 'Magnetization transfer ratio and myelin in postmortem multiple sclerosis brain', *Ann. Neurol.*, vol. 56, no. 3, pp. 407–415, Sep. 2004, doi: 10.1002/ana.20202.

[65] S. Eickhoff *et al.*, 'High-resolution MRI reflects myeloarchitecture and cytoarchitecture of human cerebral cortex', *Hum. Brain Mapp.*, vol. 24, no. 3, pp. 206–215, Mar. 2005, doi: 10.1002/hbm.20082.

[66] A. Lutti, F. Dick, M. I. Sereno, and N. Weiskopf, 'Using high-resolution quantitative mapping of R1 as an index of cortical myelination', *NeuroImage*, vol. 93, pp. 176–188, Jun. 2014, doi: 10.1016/j.neuroimage.2013.06.005.

[67] K. L. Desmond *et al.*, 'Differences in iron and manganese concentration may confound the measurement of myelin from R1 and R2 relaxation rates in studies of dysmyelination', *NMR Biomed.*, vol. 29, no. 7, pp. 985–998, 2016, doi: 10.1002/nbm.3549.

[68] G. D. Fullerton, J. L. Potter, and N. C. Dornbluth, 'NMR relaxation of protons in tissues and other macromolecular water solutions', *Magn. Reson. Imaging*, vol. 1, no. 4, pp. 209–226, Jan. 1982, doi: 10.1016/0730-725X(82)90172-2.

[69] R. M. Henkelman, G. J. Stanisz, and S. J. Graham, 'Magnetization transfer in MRI: a review', *NMR Biomed.*, vol. 14, no. 2, pp. 57–64, Apr. 2001, doi: 10.1002/nbm.683.

[70] D. K. Jones, *Diffusion MRI*. Oxford University Press, 2010.

[71] P. Mukherjee *et al.*, 'Diffusion-Tensor MR Imaging of Gray and White Matter Development during Normal Human Brain Maturation', *Am. J. Neuroradiol.*, vol. 23, no. 9, pp. 1445–1456, Oct. 2002.

[72] A. Caporale, M. Palombo, E. Macaluso, M. Guerreri, M. Bozzali, and S. Capuani, 'The γ-parameter of anomalous diffusion quantified in human brain by MRI depends on local magnetic susceptibility differences', *NeuroImage*, vol. 147, pp. 619–631, Feb. 2017, doi: 10.1016/j.neuroimage.2016.12.051.

[73] M. Guerreri *et al.*, 'Age-related microstructural and physiological changes in normal brain measured by MRI *γ*-metrics derived from anomalous diffusion signal representation', *NeuroImage*, vol. 188, pp. 654–667, Mar. 2019, doi: 10.1016/j.neuroimage.2018.12.044.

[74] D. H. Salat *et al.*, 'Age-related alterations in white matter microstructure measured by diffusion tensor imaging', *Neurobiol. Aging*, vol. 26, no. 8, pp. 1215–1227, 2005, doi: 10.1016/j.neurobiolaging.2004.09.017.

[75] E. V. Sullivan and A. Pfefferbaum, 'Diffusion Tensor Imaging in Aging and Age-Related Neurodegenerative Disorders', in *Diffusion MRI: Theory, Methods, and Applications*, P. Jones Derek K., Ed., Oxford University Press, 2010, p. 0. doi: 10.1093/med/9780195369779.003.0038.

[76] D. C. Alexander, T. B. Dyrby, M. Nilsson, and H. Zhang, 'Imaging brain microstructure with diffusion MRI: practicality and applications', *NMR Biomed.*, vol. 32, no. 4, p. e3841, Apr. 2019, doi: 10.1002/nbm.3841.

[77] I. O. Jelescu, A. de Skowronski, F. Geffroy, M. Palombo, and D. S. Novikov, 'Neurite Exchange Imaging (NEXI): A minimal model of diffusion in gray matter with inter-compartment water exchange', *NeuroImage*, vol. 256, p. 119277, Aug. 2022, doi: 10.1016/j.neuroimage.2022.119277.

[78] J. L. Olesen, L. Østergaard, N. Shemesh, and S. N. Jespersen, 'Diffusion time dependence, power-law scaling, and exchange in gray matter', *NeuroImage*, vol. 251, p. 118976, May 2022, doi: 10.1016/j.neuroimage.2022.118976.

[79] D. S. Novikov, J. H. Jensen, J. A. Helpern, and E. Fieremans, 'Revealing mesoscopic structural universality with diffusion', *Proc. Natl. Acad. Sci.*, vol. 111, no. 14, pp. 5088–5093, Apr. 2014, doi: 10.1073/pnas.1316944111.

[80] D. S. Novikov, E. Fieremans, J. H. Jensen, and J. A. Helpern, 'Random walks with barriers', *Nat. Phys.*, vol. 7, no. 6, pp. 508–514, Jun. 2011, doi: 10.1038/nphys1936.

[81] J. Hutter *et al.*, 'Time-efficient and flexible design of optimized multishell HARDI diffusion', *Magn. Reson. Med.*, vol. 79, no. 3, pp. 1276–1292, 2018, doi: 10.1002/mrm.26765.

[82] J. Veraart, D. S. Novikov, D. Christiaens, B. Ades-aron, J. Sijbers, and E. Fieremans, 'Denoising of diffusion MRI using random matrix theory', *NeuroImage*, vol. 142, pp. 394–406, Nov. 2016, doi: 10.1016/j.neuroimage.2016.08.016.

[83] J.-D. Tournier *et al.*, 'MRtrix3: A fast, flexible and open software framework for medical image processing and visualisation', *NeuroImage*, vol. 202, p. 116137, Nov. 2019, doi: 10.1016/j.neuroimage.2019.116137.

[84] M. Jenkinson, C. F. Beckmann, T. E. J. Behrens, M. W. Woolrich, and S. M. Smith, 'FSL', *NeuroImage*, vol. 62, no. 2, pp. 782–790, Aug. 2012, doi: 10.1016/j.neuroimage.2011.09.015.

[85] D. K. Jones and P. J. Basser, '"Squashing peanuts and smashing pumpkins": How noise distorts diffusion-weighted MR data', *Magn. Reson. Med.*, vol. 52, no. 5, pp. 979–993, 2004, doi: 10.1002/mrm.20283.

[86] O. Dietrich, J. G. Raya, S. B. Reeder, M. F. Reiser, and S. O. Schoenberg, 'Measurement of signal-to-noise ratios in MR images: influence of multichannel coils, parallel imaging, and reconstruction filters', *J. Magn. Reson. Imaging JMRI*, vol. 26, no. 2, pp. 375–385, Aug. 2007, doi: 10.1002/jmri.20969.

[87] M. F. Glasser *et al.*, 'A multi-modal parcellation of human cerebral cortex', *Nature*, vol. 536, no. 7615, pp. 171–178, Aug. 2016, doi: 10.1038/nature18933.

[88] S. Mori *et al.*, 'Stereotaxic white matter atlas based on diffusion tensor imaging in an ICBM template', *NeuroImage*, vol. 40, no. 2, pp. 570–582, Apr. 2008, doi: 10.1016/j.neuroimage.2007.12.035.

[89] M. Afzali, M. Nilsson, M. Palombo, and D. K. Jones, 'SPHERIOUSLY? The challenges of estimating sphere radius non-invasively in the human brain from diffusion MRI', *NeuroImage*, vol. 237, p. 118183, Aug. 2021, doi: 10.1016/j.neuroimage.2021.118183.

[90] B. Fischl, 'FreeSurfer', *NeuroImage*, vol. 62, no. 2, pp. 774–781, Aug. 2012, doi: 10.1016/j.neuroimage.2012.01.021.

[91] S. Schiavi *et al.*, 'Mapping tissue microstructure across the human brain on a clinical scanner with soma and neurite density image metrics', *Hum. Brain Mapp.*, vol. 44, no. 13, pp. 4792–4811, Sep. 2023, doi: 10.1002/hbm.26416.

[92] D. K. Jones, T. R. Knösche, and R. Turner, 'White matter integrity, fiber count, and other fallacies: The do's and don'ts of diffusion MRI', *NeuroImage*, vol. 73, pp. 239–254, Jun. 2013, doi: 10.1016/j.neuroimage.2012.06.081.

[93] R. C. Berg, T. Leutritz, N. Weiskopf, and C. Preibisch, 'Multi-parameter quantitative mapping of R1, R2*, PD, and MTsat is reproducible when accelerated with Compressed SENSE', *NeuroImage*, vol. 253, p. 119092, Jun. 2022, doi: 10.1016/j.neuroimage.2022.119092.

[94] N. Weiskopf *et al.*, 'Quantitative multi-parameter mapping of R1, PD*, MT, and R2* at 3T: a multi-center validation', *Front. Neurosci.*, vol. 7, 2013, doi: 10.3389/fnins.2013.00095.

[95] E. A. Krijnen *et al.*, 'Detection of grey matter microstructural substrates of neurodegeneration in multiple sclerosis', *Brain Commun.*, vol. 5, no. 3, p. fcad153, May 2023, doi: 10.1093/braincomms/fcad153.

[96] R. Turner, 'Myelin and Modeling: Bootstrapping Cortical Microcircuits', *Front. Neural Circuits*, vol. 13, p. 34, 2019, doi: 10.3389/fncir.2019.00034.

[97] C. L. Call and D. E. Bergles, 'Cortical neurons exhibit diverse myelination patterns that scale between mouse brain regions and regenerate after demyelination', *Nat. Commun.*, vol. 12, no. 1, p. 4767, Aug. 2021, doi: 10.1038/s41467-021-25035-2.

[98] U. Dicke and G. Roth, 'Neuronal factors determining high intelligence', *Philos. Trans. R. Soc. B Biol. Sci.*, vol. 371, no. 1685, p. 20150180, Jan. 2016, doi: 10.1098/rstb.2015.0180.

[99] S.-K. Song, S.-W. Sun, M. J. Ramsbottom, C. Chang, J. Russell, and A. H. Cross, 'Dysmyelination revealed through MRI as increased radial (but unchanged axial) diffusion of water', *NeuroImage*, vol. 17, no. 3, pp. 1429–1436, Nov. 2002, doi: 10.1006/nimg.2002.1267.

[100] P. van Gelderen, X. Jiang, and J. H. Duyn, ‘Effects of Magnetization Transfer on T1 Contrast in Human Brain White Matter’, *NeuroImage*, vol. 128, pp. 85–95, Mar. 2016, doi: 10.1016/j.neuroimage.2015.12.032.

[101] J. Jamarik, L. Vojtišek, and D. Schwarz, ‘Uncovering cortical layers with multi-exponential analysis: a region of interest study’, in *2022 30th European Signal Processing Conference (EUSIPCO)*, Aug. 2022, pp. 1353–1356. doi: 10.23919/EUSIPCO55093.2022.9909806.

[102] J. A. Rioux, I. R. Levesque, and B. K. Rutt, ‘Biexponential longitudinal relaxation in white matter: Characterization and impact on T1 mapping with IR-FSE and MP2RAGE’, *Magn. Reson. Med.*, vol. 75, no. 6, pp. 2265–2277, Jun. 2016, doi: 10.1002/mrm.25729.

[103] A. M. Saunders *et al.*, ‘Comparison and calibration of MP2RAGE quantitative T1 values to multi-TI inversion recovery T1 values’, *Magn. Reson. Imaging*, vol. 117, p. 110322, Apr. 2025, doi: 10.1016/j.mri.2025.110322.

[104] R. Shafee, R. L. Buckner, and B. Fischl, ‘Gray matter myelination of 1555 human brains using partial volume corrected MRI images’, *NeuroImage*, vol. 105, pp. 473–485, Jan. 2015, doi: 10.1016/j.neuroimage.2014.10.054.

[105] Y. Assaf and P. J. Basser, ‘Composite hindered and restricted model of diffusion (CHARMED) MR imaging of the human brain’, *NeuroImage*, vol. 27, no. 1, pp. 48–58, Aug. 2005, doi: 10.1016/j.neuroimage.2005.03.042.

[106] P. J. Basser, ‘Invention and Development of Diffusion Tensor MRI (DT-MRI or DTI) at the NIH’, in *Diffusion MRI: Theory, Methods, and Applications*, P. Jones Derek K., Ed., Oxford University Press, 2010, p. 0. doi: 10.1093/med/9780195369779.003.0047.

[107] D. Le Bihan, ‘Magnetic Resonance Diffusion Imaging: Introduction and Concepts’, in *Diffusion MRI: Theory, Methods, and Applications*, P. Jones Derek K., Ed., Oxford University Press, 2010, p. 0. doi: 10.1093/med/9780195369779.003.0005.

[108] Y. Assaf and P. J. Basser, ‘Composite hindered and restricted model of diffusion (CHARMED) MR imaging of the human brain’, *NeuroImage*, vol. 27, no. 1, pp. 48–58, Aug. 2005, doi: 10.1016/j.neuroimage.2005.03.042.

[109] I. Tavor, S. Hofstetter, and Y. Assaf, ‘Micro-structural assessment of short term plasticity dynamics’, *NeuroImage*, vol. 81, pp. 1–7, Nov. 2013, doi: 10.1016/j.neuroimage.2013.05.050.

[110] J. P. Marques, T. Kober, G. Krueger, W. van der Zwaag, P.-F. Van de Moortele, and R. Gruetter, ‘MP2RAGE, a self bias-field corrected sequence for improved segmentation and T1-mapping at high field’, *NeuroImage*, vol. 49, no. 2, pp. 1271–1281, Jan. 2010, doi: 10.1016/j.neuroimage.2009.10.002.

[111] T. W. Okell, M. A. Chappell, M. E. Kelly, and P. Jezzard, ‘Cerebral Blood Flow Quantification Using Vessel-Encoded Arterial Spin Labeling’, *J. Cereb. Blood Flow Metab.*, vol. 33, no. 11, pp. 1716–1724, Nov. 2013, doi: 10.1038/jcbfm.2013.129.

[112] V. J. Schmithorst, L. Hernandez-Garcia, J. Vannest, A. Rajagopal, G. Lee, and S. K. Holland, ‘Optimized simultaneous ASL and BOLD functional imaging of the whole brain: Whole-Brain ASL/BOLD Functional Imaging’, *J. Magn. Reson. Imaging*, vol. 39, no. 5, pp. 1104–1117, May 2014, doi: 10.1002/jmri.24273.

[113] J. W. Peirce, ‘PsychoPy—Psychophysics software in Python’, *J. Neurosci. Methods*, vol. 162, no. 1–2, pp. 8–13, May 2007, doi: 10.1016/j.jneumeth.2006.11.017.

[114] M. Jenkinson, P. Bannister, M. Brady, and S. Smith, ‘Improved Optimization for the Robust and Accurate Linear Registration and Motion Correction of Brain Images’, *NeuroImage*, vol. 17, no. 2, pp. 825–841, Oct. 2002, doi: 10.1006/nimg.2002.1132.

[115] S. M. Smith, ‘Fast robust automated brain extraction’, *Hum. Brain Mapp.*, vol. 17, no. 3, pp. 143–155, Nov. 2002, doi: 10.1002/hbm.10062.

[116] S. M. Smith and J. M. Brady, ‘SUSAN—A New Approach to Low Level Image Processing’, 1997.

[117] M. Jenkinson and S. Smith, ‘A global optimisation method for robust affine registration of brain images’, *Med. Image Anal.*, vol. 5, no. 2, pp. 143–156, Jun. 2001, doi: 10.1016/S1361-8415(01)00036-6.

[118] C. Paquola and S.-J. Hong, ‘The Potential of Myelin-Sensitive Imaging: Redefining Spatiotemporal Patterns of Myeloarchitecture’, *Biol. Psychiatry*, vol. 93, no. 5, pp. 442–454, Mar. 2023, doi: 10.1016/j.biopsych.2022.08.031.

[119] M. M. Menz, J. Neumann, K. Müller, and S. Zysset, ‘Variability of the BOLD response over time: an examination of within-session differences’, *NeuroImage*, vol. 32, no. 3, pp. 1185–1194, Sep. 2006, doi: 10.1016/j.neuroimage.2006.06.003.

[120] F. X. Graydon, K. J. Friston, C. G. Thomas, V. B. Brooks, and R. S. Menon, ‘Learning-related fMRI activation associated with a rotational visuo-motor transformation’, *Brain Res. Cogn. Brain Res.*, vol. 22, no. 3, pp. 373–383, Mar. 2005, doi: 10.1016/j.cogbrainres.2004.09.007.

[121] A. E. Aloufi, F. J. Rowe, and G. F. Meyer, ‘Behavioural performance improvement in visuomotor learning correlates with functional and microstructural brain changes’, *NeuroImage*, vol. 227, p. 117673, Feb. 2021, doi: 10.1016/j.neuroimage.2020.117673.

[122] E. Berlot, N. J. Popp, and J. Diedrichsen, ‘A critical re-evaluation of fMRI signatures of motor sequence learning’, *eLife*, vol. 9, p. e55241, May 2020, doi: 10.7554/eLife.55241.

[123] M. A. Perez, S. Tanaka, S. P. Wise, D. T. Willingham, and L. G. Cohen, ‘Time-Specific Contribution of the Supplementary Motor Area to Intermanual Transfer of Procedural Knowledge’, *J. Neurosci.*, vol. 28, no. 39, pp. 9664–9669, Sep. 2008, doi: 10.1523/JNEUROSCI.3416-08.2008.

[124] C. Saiote, R. Polanía, K. Rosenberger, W. Paulus, and A. Antal, ‘High-Frequency TRNS Reduces BOLD Activity during Visuomotor Learning’, *PLOS ONE*, vol. 8, no. 3, p. e59669, Mar. 2013, doi: 10.1371/journal.pone.0059669.

[125] S. O. Dumoulin, ‘Layers of Neuroscience’, *Neuron*, vol. 96, no. 6, pp. 1205–1206, Dec. 2017, doi: 10.1016/j.neuron.2017.12.004.

[126] I. Shamir and Y. Assaf, ‘Expanding connectomics to the laminar level: A perspective’, *Netw. Neurosci.*, vol. 7, no. 2, pp. 377–388, Jun. 2023, doi: 10.1162/netn_a_00304.

[127] R. Nieuwenhuys, ‘The myeloarchitectonic studies on the human cerebral cortex of the Vogt–Vogt school, and their significance for the interpretation of functional neuroimaging data’, *Brain Struct. Funct.*, vol. 218, no. 2, pp. 303–352, Mar. 2013, doi: 10.1007/s00429-012-0460-z.

[128] M. F. Glasser and D. C. Van Essen, ‘Mapping human cortical areas in vivo based on myelin content as revealed by T1- and T2-weighted MRI’, *J. Neurosci. Off. J. Soc. Neurosci.*, vol. 31, no. 32, pp. 11597–11616, Aug. 2011, doi: 10.1523/JNEUROSCI.2180-11.2011.

[129] R. Nieuwenhuys, J. Voogd, and C. Van Huijzen, *The Human Central Nervous System*. Berlin, Heidelberg: Springer, 2008. doi: 10.1007/978-3-540-34686-9.

[130] A. Lutti, F. Dick, M. I. Sereno, and N. Weiskopf, ‘Using high-resolution quantitative mapping of R1 as an index of cortical myelination’, *NeuroImage*, vol. 93, pp. 176–188, Jun. 2014, doi: 10.1016/j.neuroimage.2013.06.005.

[131] C. Stüber *et al.*, ‘Myelin and iron concentration in the human brain: a quantitative study of MRI contrast’, *NeuroImage*, vol. 93 Pt 1, pp. 95–106, Jun. 2014, doi: 10.1016/j.neuroimage.2014.02.026.

[132] B. Fischl, ‘FreeSurfer’, *NeuroImage*, vol. 62, no. 2, pp. 774–781, Aug. 2012, doi: 10.1016/j.neuroimage.2012.01.021.

[133] S. Huang *et al.*, ‘Visualizing cortical laminar architecture in the living human brain using next-generation ultra-high-gradient diffusion MRI’, *Res. Sq.*, p. rs.3.rs-6724971, Jun. 2025, doi: 10.21203/rs.3.rs-6724971/v1.

Appendix A – Supplementary Materials

The first four figures included in this Appendix (Figures S1-S4) were previously published in [56].

Inclusion of subcortical structures in the correlation analysis

By employing the AAL2 atlas (10.1016/j.neuroimage.2015.07.075) the following subcortical GM ROIs were included: right and left putamen, caudate, pallidum, thalamus, hippocampus and amygdala. The GM partial volume estimate maps derived from the FSL FAST were used, resulting in a partial mask of the thalamus region (which also comprises WM structures and therefore is not correctly represented in this case). ROIs with a number of voxels exceeding the 20th percentile were retained, as in the original analysis, ending up by discarding the globus pallidus. Outliers were evaluated considering the distributions of cortical and subcortical GM ROIs separately, excluding the experimental points with values above/below 3 median absolute deviations from the median of the distribution, as done in the original paper. The scatter plots of the SANDI parameters and R1 across ROIs including the subcortical structures are shown in Figure S1. Pearson's correlation coefficients and p-values are shown (Bonferroni corrected p-value=0.05/6=0.0083). Figure S2 shows the same plots but considering a combination of GM and WM partial volume estimate mask, allowing to better represent some subcortical GM ROIs, such as the thalamus. The subcortical structures clustered in the regions of lower extra-neurite diffusivities (De) and larger R1 (Fig. S1E,1F), vanishing the correlation between De and R1. Including subcortical structures did not affect significantly the results of the correlations between SANDI metrics and R1 across subjects, as shown in Figure S3.

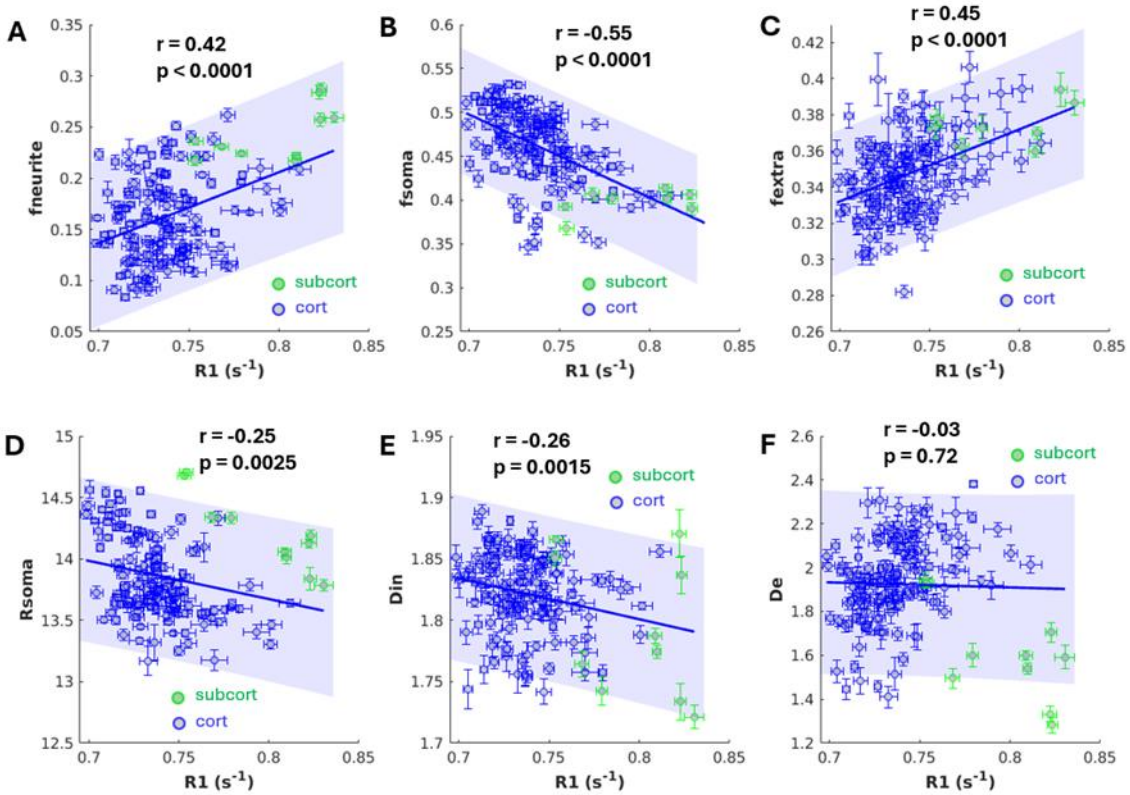


Figure S1. Scatter plots of SANDI metrics vs R1 in cortical and subcortical Gray Matter regions (GM ROIs). *The experimental points represent cortical GM ROIs (cort, blue circles) and subcortical GM ROIs (subcort, green circles). The Pearson's correlation coefficients are indicated (with the original p-value; please consider that Bonferroni corrected p-value is 0.0083). Each marker represents, for a different brain region, the median across subjects of the regional median of the parameter. Error bars are standard errors (median absolute deviations/squared root of number of subjects). The regression line is shown in blue. Shaded areas represent 95% confidence intervals.*

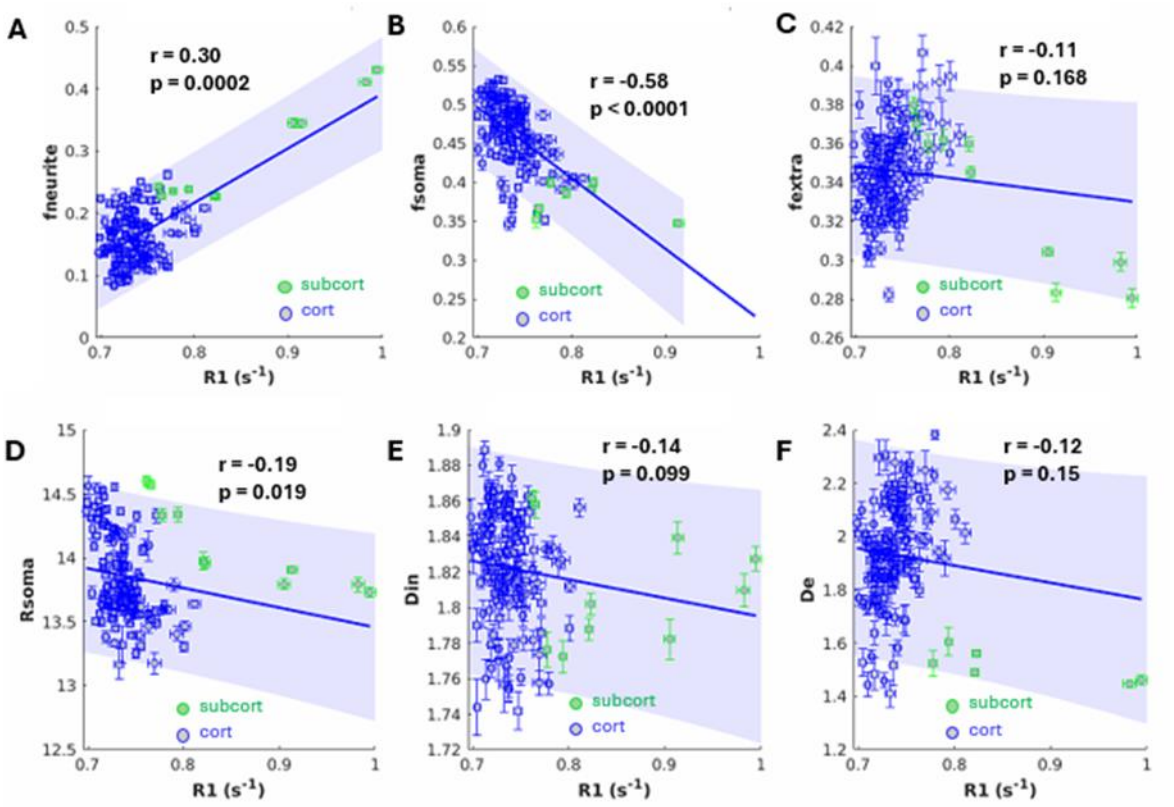


Figure S2. Scatter plots of SANDI metrics vs R1 in cortical and subcortical Gray Matter regions (GM ROIs) using GM and WM partial volume estimate masking. *The experimental points represent cortical GM ROIs (cort, blue circles) and subcortical GM ROIs (subcort, green circles). The Pearson's correlation coefficients are indicated (with the original p-value; please consider that Bonferroni corrected p-value is 0.0083). Each marker represents, for a different brain region, the median across subjects of the regional median of the parameter. Error bars are standard errors (median absolute deviations/squared root of number of subjects). The regression line is shown in blue. Shaded areas represent 95% confidence intervals.*

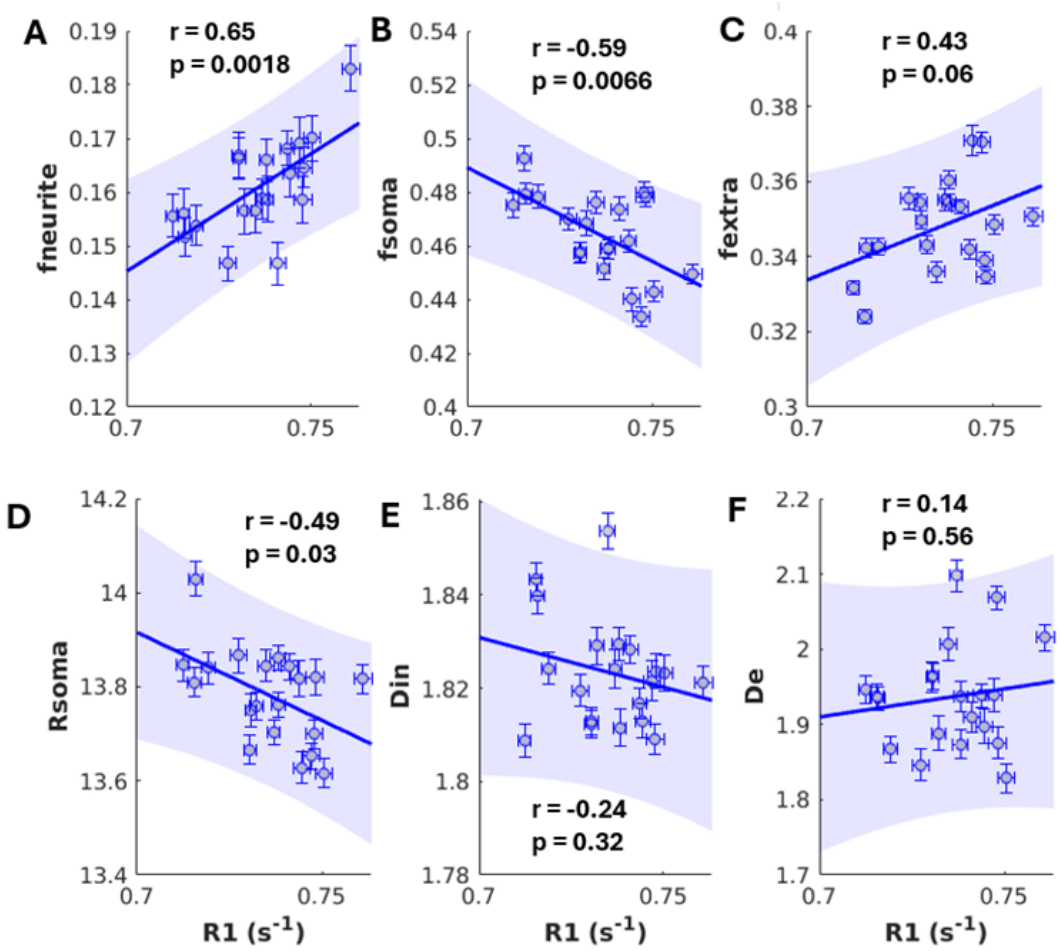


Figure S3. Scatter plots of SANDI metrics vs R1 in Grey Matter (including cortical and subcortical structures) across subjects. *The Pearson's correlation coefficient between SANDI metrics quantified in GM regions is indicated (with the original p-values shown). Each marker represents, for a different subject, the median across regions of the specific parameter. Error bars are standard errors (median absolute deviations/squared root of number of subjects). Markers and regression lines are shown in blue. Shaded areas represent 95% confidence intervals.*

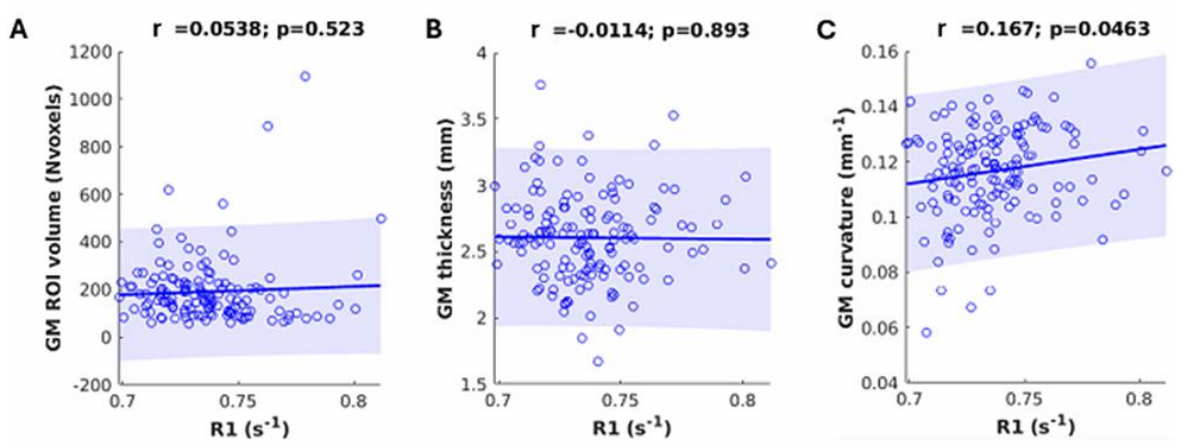


Figure S4. Scatter plot of Gray Matter (GM) region volume, cortical thickness and curvature against R1. *The Pearson's correlation coefficient is reported with the significance level, p. The thick line represents the regression line. Each marker represents the median across subjects in a given GM region.*

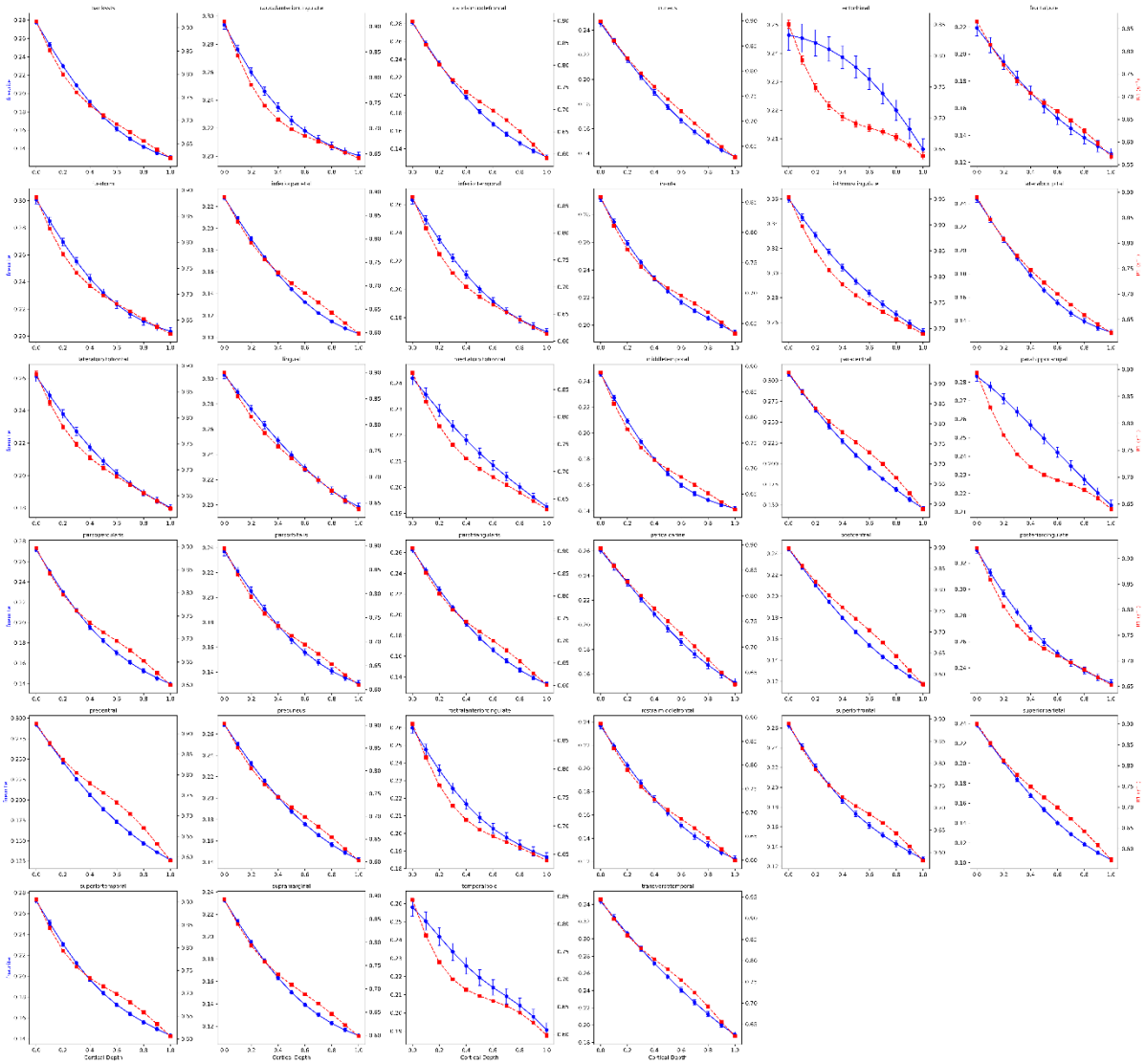


Figure S5. Depth - dependent profiles of intra - neurite signal fraction (fneurite, blue, left axis) and R1 (red, right axis) across cortical layers in all ROIs defined by the Desikan - Killiany atlas. *Mean values ± standard deviation across subjects are shown for the left hemisphere. Cortical depth is expressed as normalized distance from the white matter boundary (0) to the pial surface (1).*

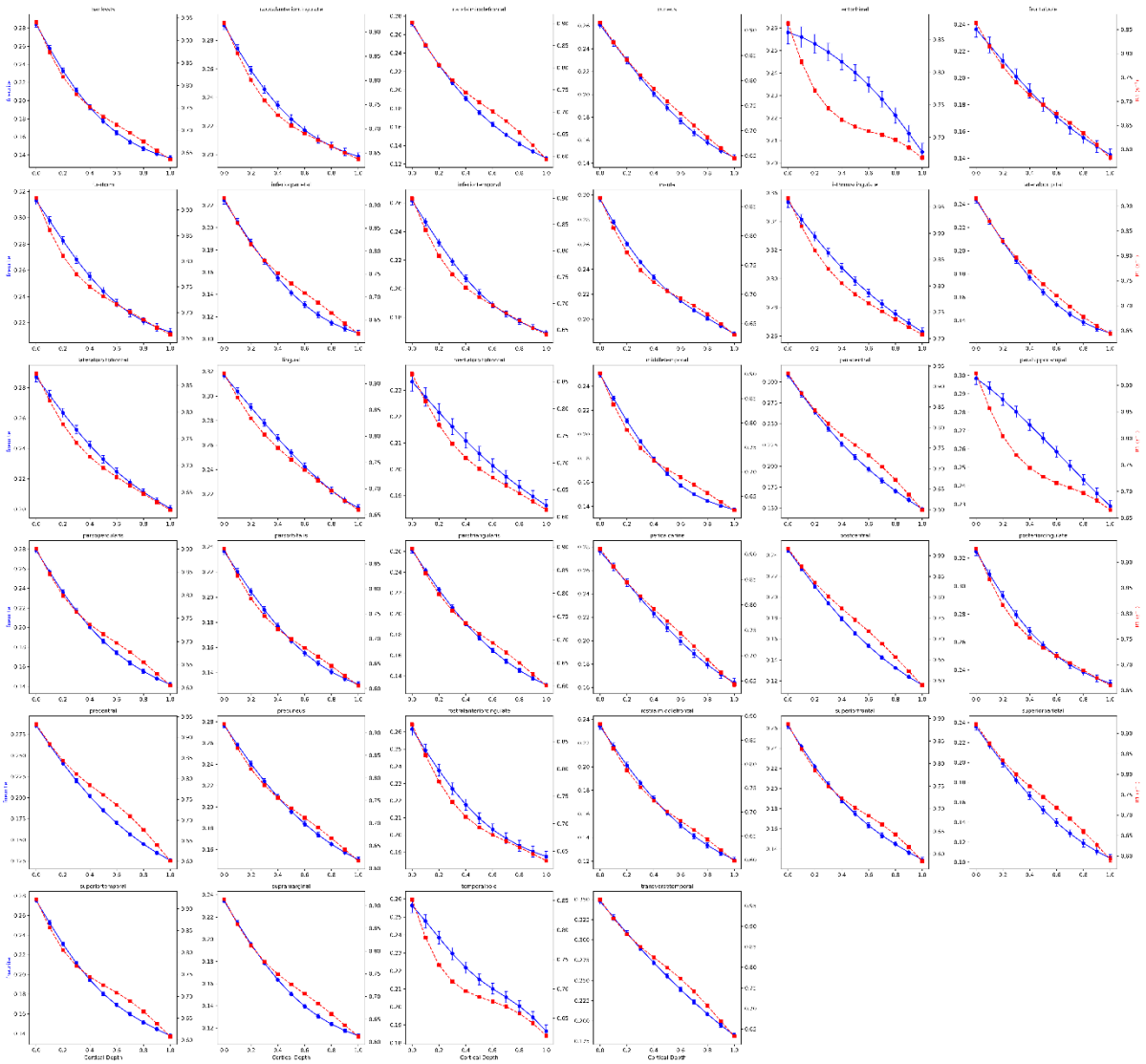


Figure S6. Depth - dependent profiles of intra - neurite signal fraction (fneurite, blue, left axis) and R1 (red, right axis) across cortical layers in all ROIs defined by the Desikan - Killiany atlas. *Mean values ± standard deviation across subjects are shown for the right hemisphere. Cortical depth is expressed as normalized distance from the white matter boundary (0) to the pial surface (1).*

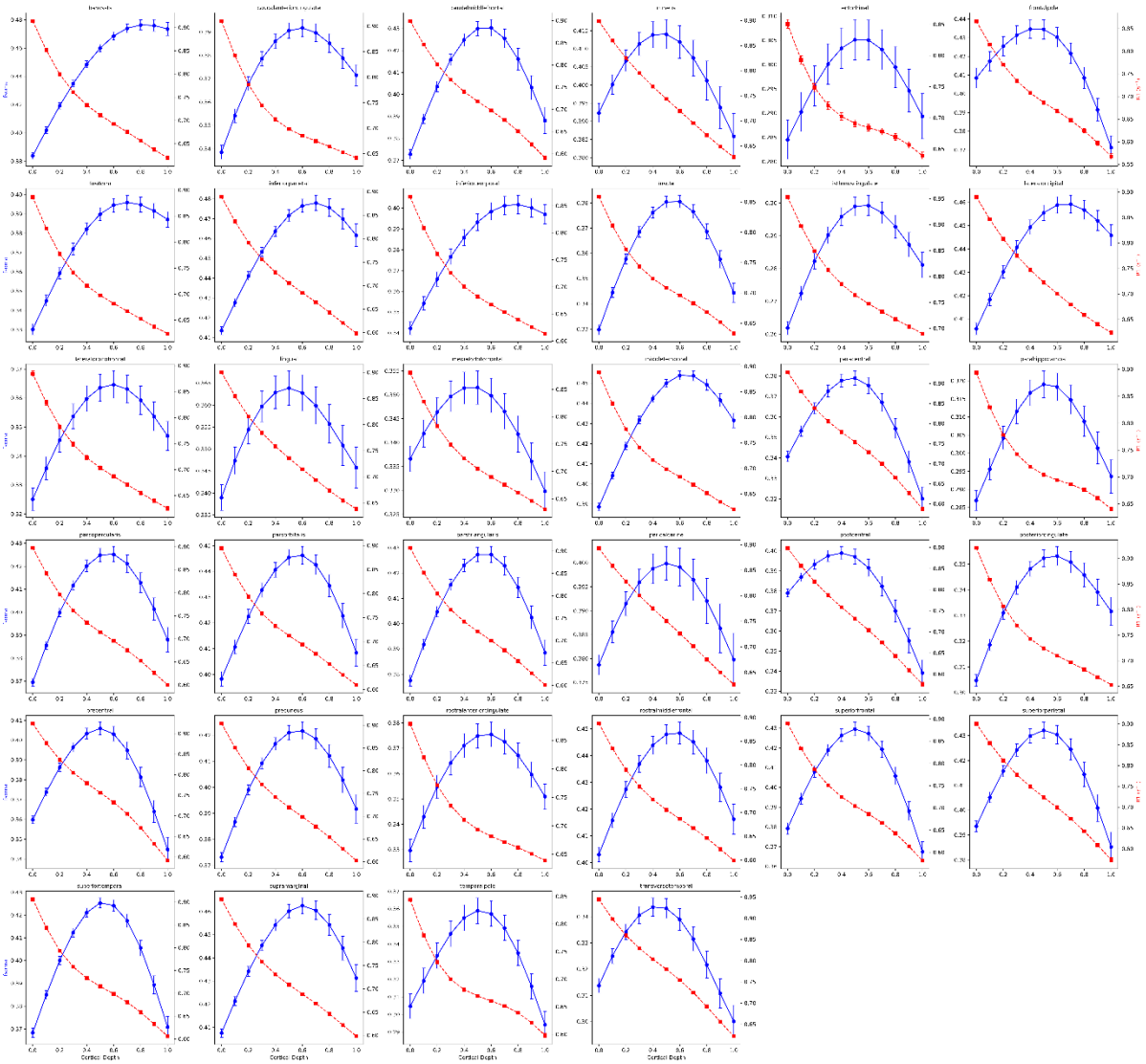


Figure S7. Depth - dependent profiles of intra - soma signal fraction (fsoma, blue, left axis) and R1 (red, right axis) across cortical layers in all ROIs defined by the Desikan - Killiany atlas. *Mean values ± standard deviation across subjects are shown for the left hemisphere. Cortical depth is expressed as normalized distance from the white matter boundary (0) to the pial surface (1).*

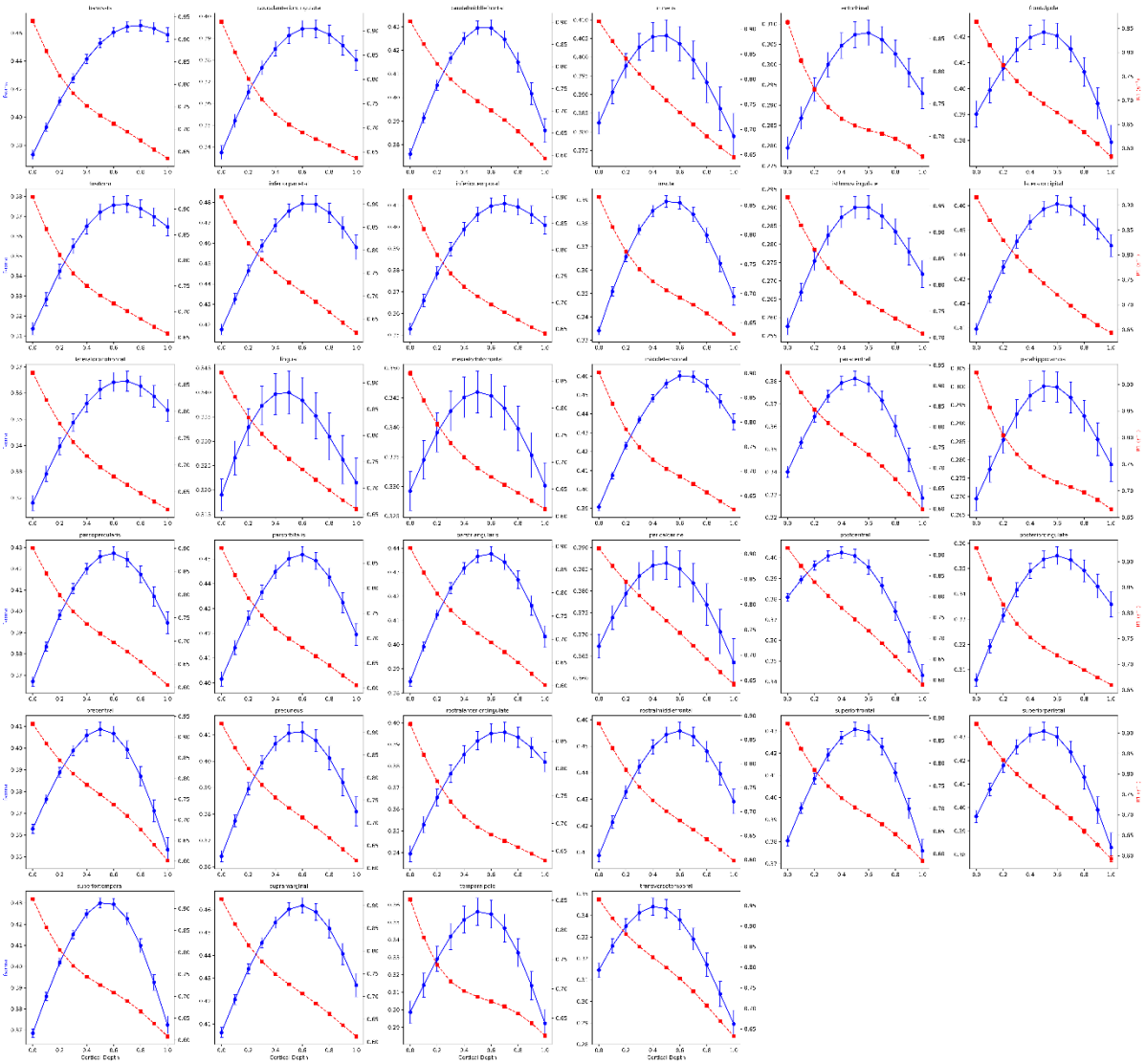


Figure S8. Depth - dependent profiles of intra - soma signal fraction (fsoma, blue, left axis) and R1 (red, right axis) across cortical layers in all ROIs defined by the Desikan - Killiany atlas. *Mean values ± standard deviation across subjects are shown for the right hemisphere. Cortical depth is expressed as normalized distance from the white matter boundary (0) to the pial surface (1).*

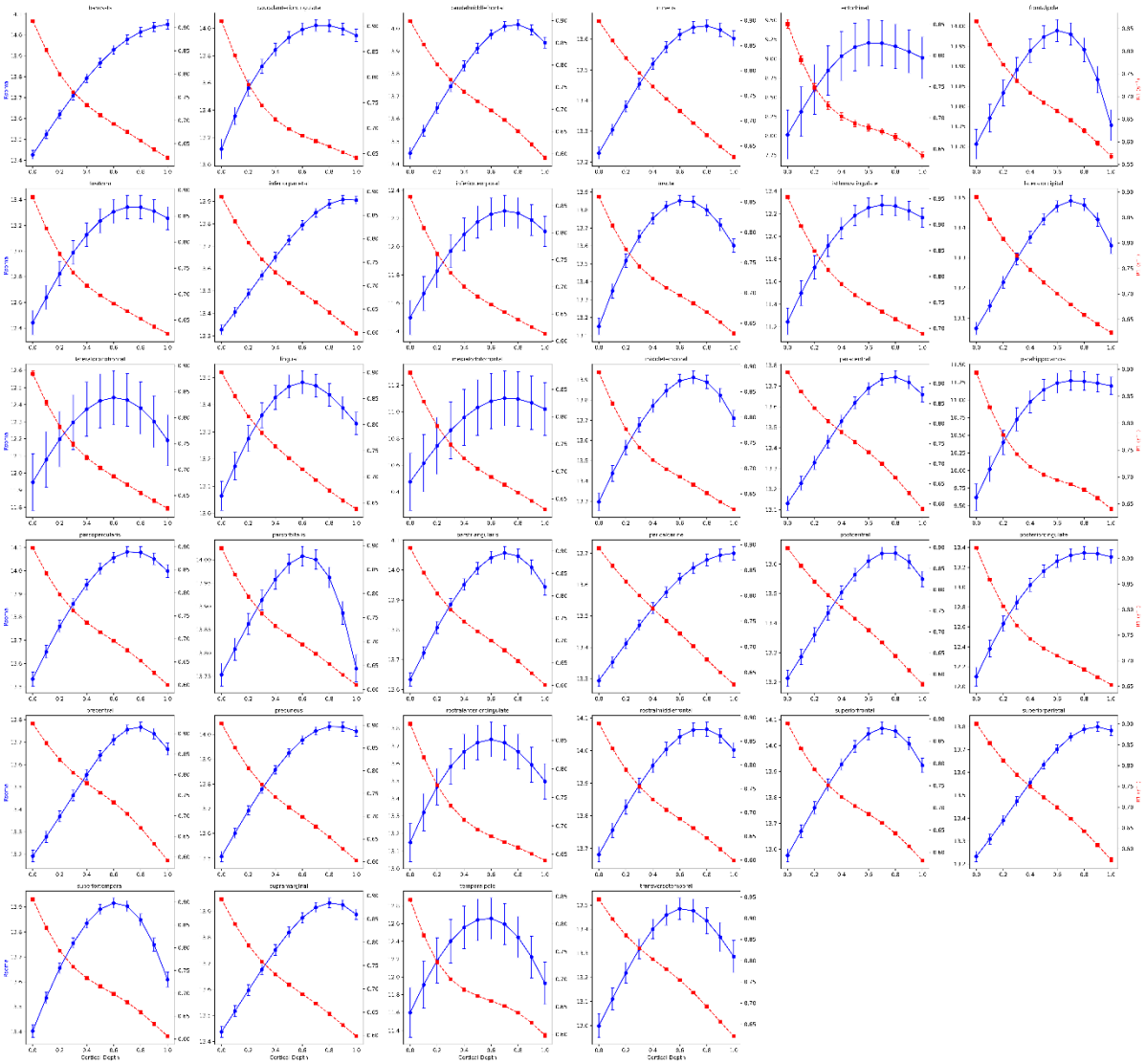


Figure S9. Depth - dependent profiles of estimated soma radius (Rsoma, blue, left axis) and R1 (red, right axis) across cortical layers in all ROIs defined by the Desikan - Killiany atlas. *Mean values ± standard deviation across subjects are shown for the left hemisphere. Cortical depth is expressed as normalized distance from the white matter boundary (0) to the pial surface (1).*

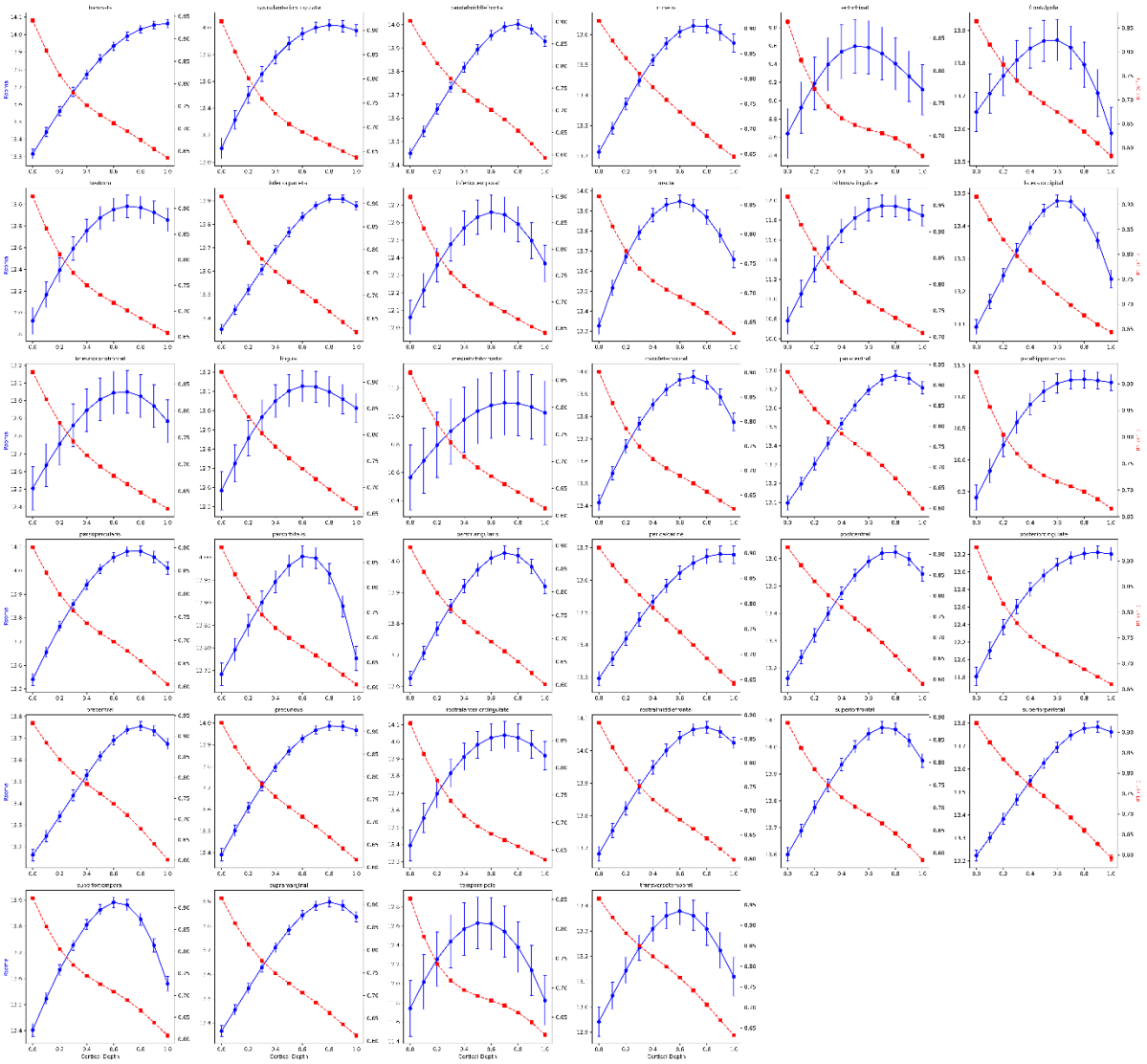


Figure S10. Depth - dependent profiles of estimated soma radius (Rsoma, blue, left axis) and R1 (red, right axis) across cortical layers in all ROIs defined by the Desikan - Killiany atlas. *Mean values ± standard deviation across subjects are shown for the right hemisphere. Cortical depth is expressed as normalized distance from the white matter boundary (0) to the pial surface (1).*